L. Tauscher

Institut de Physique
Université de Fribourg (Suisse)

Measurement of the K^0_{e3} Form Factor in the CPLEAR Experiment

THESE

présentée à la faculté des Sciences de l'Université de Fribourg (Suisse)
pour l'obtention du grade de *Doctor rerum naturalium* par

Frédéric Blanc
de
Montreux (VD)

Thèse N° 1198
Mécanographie Université, Fribourg
1998

Institut de Physique
Université de Fribourg (Suisse)

Measurement of the K^0_{e3} Form Factor in the CPLEAR Experiment

THESE

présentée à la faculté des Sciences de l'Université de Fribourg (Suisse) pour l'obtention du grade de *Doctor rerum naturalium* par

Frédéric Blanc
de
Montreux (VD)

Thèse N° 1198
Mécanographie Université, Fribourg
1998

Acceptée par la Faculté des Sciences de l'Université de Fribourg (Suisse) sur la proposition de:
Prof. Dr. L. Schaller, de l'Université de Fribourg,
Prof. Dr. L. Tauscher, de l'Université de Bâle, et
PD Dr. T. Nakada, du Paul Scherrer Institute (PSI), Villigen.

Fribourg, le 13 mars 1998

Le Directeur de Thèse

Prof. Dr. L. Schaller

Le Doyen:

Prof. Dr. B. Hirsbrunner

Résumé

L'expérience CPLEAR a eu pour but d'étudier les symétries discrètes CP, T et CPT au LEAR ("Low Energy Antiproton Ring") du CERN. De 1989 à 1996, une grande quantité de désintégrations du kaon neutre (K^0) et de son antiparticule ($\overline{K}^0$) dans différents canaux a été observée. En effet, le système du kaon neutre est encore actuellement le système le plus adapté à l'étude des symétries discrètes. Bien que les mesons K^0 et $\overline{K}^0$ soient des états propres des interactions forte et electromagnetique, ils ne le sont pas pour l'interaction faible, qui, elle, ne conserve pas l'étrangeté. Ainsi, le K^0 et le $\overline{K}^0$ peuvent osciller l'un en l'autre par interactions faibles. Deux états propres de masse sont créés, K_S et K_L, correspondant aux deux modes d'oscillation possibles. Ces deux particules peuvent se désintégrer dans les modes semileptoniques $\pi e \nu$ et $\pi \mu \nu$. De plus, le K_S se désintègre aussi en deux pions ($\pi^+\pi^-$ ou $\pi^0\pi^0$) avec un temps de vie court, alors que le K_L se désintègre en trois pions ($\pi^+\pi^-\pi^0$ ou $\pi^0\pi^0\pi^0$), avec un temps de vie long. Donc, puisque les états à deux et trois pions sont des états propres de la symétrie CP, avec des valeurs propres CP$= +1$ et CP$= -1$, on pouvait penser que le K_S et le K_L étaient des états propres de la symétrie CP. Mais en 1964, des désintégrations du K_L en deux pions ont été observées [1]. Ainsi, la symétrie CP n'était pas respectée par l'interaction faible. A ce jour, le système du kaon neutre est le seul système où cette non-conservation de CP (violation de CP) a été observée.

Depuis cette découverte, de nombreux efforts ont été faits pour comprendre la violation de CP. L'introduction d'éléments complexes dans la matrice CKM permet d'inclure la violation de CP dans le modèle standard [2], sans toutefois en expliquer l'origine. Du point de vue expérimental, cette symétrie a été étudiée principalement au moyen de faisceaux de K_L. Les paramètres décrivant la violation de CP dans le système du kaon neutre ont pu être mesurés, en particulier le rapport des amplitudes de désintégration du K_L et du K_S dans les désintégrations en deux pions, $\eta_{+-} = A(K_L \to \pi^+\pi^-)/A(K_S \to \pi^+\pi^-)$. De son coté, l'expérience CPLEAR a utilisé des kaons d'étrangeté déterminée à leur production. Les kaons neutres étaient produits dans des annihilations $p\overline{p}$ au repos, par les processus:

$$\begin{aligned} p\overline{p} &\to K^-\pi^+K^0 \quad \text{et} \\ p\overline{p} &\to K^+\pi^-\overline{K}^0. \end{aligned}$$

De ce fait, l'étrangeté du K^0 ($\overline{K}^0$) produit était déterminée par la charge du kaon associé.

Dans chaque voie de désintégration, les paramètres de la violation de CP étaient obtenus au moyen d'asymétries construites avec les taux de désintégration mesurés pour chacun des deux états d'étrangeté initiaux. Alors, puisque dans les asymétries, les acceptances absolues s'annulent, seules les acceptances relatives étaient à considérer. Ainsi, le détecteur et les procédures d'analyse ont été optimisés pour minimiser ces effets relatifs non désirés.

Pour l'expérience CPLEAR, un détecteur à géométrie cylindrique a été utilisé. Les réactions $p\overline{p}$ étaient produites par un faisceau d'antiprotons du LEAR dirigé sur une cible d'hydrogène, au centre du détecteur. Les trajectoires des particules étaient détectées par 3 chambres proportionnelles, 6 chambres à dérive (drift chambers), et 2 rangées de tubes à décharges (streamer tubes). Les kaons chargés étaient identifiés par un compteur Čerenkov à seuil, situé entre deux scintillateurs. Enfin, les particules neutres

étaient détectées par un calorimètre électromagnétique. L'ensemble du détecteur se trouvait dans un champ magnétique de 0.44 T.

Dans cette thèse, une étude des performances de deux des chambres proportionnelles est présentée. Plus précisément, la dépendance de leurs efficacités en fonction des paramètres géométriques et de la quantité de mouvement des particules a été étudiée. Les efficacités moyennes mesurées pour ces deux chambres proportionnelles, étaient de $(95.97 \pm 0.21)\%$ et de $(96.73 \pm 0.21)\%$. Les pertes d'efficacité dues aux canaux défectueux, ainsi qu'aux supports des fils dans les chambres, ont également été estimées. De plus, cette étude a permis de vérifier précisément la position des chambres dans le détecteur CPLEAR. Finalement, la même analyse a été effectuée sur des données de simulation. Les résultats obtenus sont compatibles avec les résultats des données réelles.

En plus des tests de symétries, la quantité de données accumulée par CPLEAR devait permettre la mesure du facteur de forme électrofaible dans les désintégrations semileptoniques du kaon neutre (désintégrations K^0_{e3}). L'effet du facteur de forme se manifeste dans l'amplitude de désintégration, et dépend de variables cinématiques. Contrairement aux paramètres de la violation de CP, le facteur de forme ne peut pas être mesuré au moyen d'asymétries. Cela implique donc une excellente compréhension de l'acceptance absolue du détecteur. Il faut noter que seule une différence entre les facteurs de forme dans les désintégrations K^0_{e3} et $\overline{K}^0_{e3}$ pourrait être mesurée au moyen d'asymétries. Un tel résultat serait un signe de violation de CP dans les amplitudes de désintégration. Toutefois, ceci n'est pas prédit par le modèle standard.

Dans cette thèse, une analyse détaillée des performances du programme de simulation de CPLEAR est présentée. Afin d'améliorer la qualité de cette simulation, des corrections basées sur des données de calibration sont proposées. Ensuite, le facteur de forme dans les désintégrations K^0_{e3} est mesuré en comparant la cinématique des données de simulation et réelles. A cette fin, les critères de sélection des évenements ont été optimisés pour rejeter les modes de désintégration $\pi\mu\nu$, $\pi^+\pi^-$ et $\pi^+\pi^-\pi^0$, qui constituent la contamination principale du mode $\pi e\nu$. Comme pour les mesures des expériences précédentes, une dépendance linéaire du facteur de forme f_+ avec le carré du transfert de quantité de mouvement (q^2) à la paire leptonique a été observée:

$$f_+(q^2) = f_+(0) \cdot (1 + \lambda_+ \frac{q^2}{m_\pi^2}).$$

Le résultat obtenu pour le paramètre λ_+ est:

$$\lambda_+ = 0.0245 \pm 0.0012_{\mathrm{stat}} \pm 0.0029_{\mathrm{syst}}.$$

L'incertitude est du même ordre de grandeur que celle des mesures publiées les plus précises. En tenant compte de ce résultat, la moyenne de toutes les mesures devient

$$\lambda_+ = 0.0291 \pm 0.0014.$$

Summary

The CPLEAR experiment studied the discrete CP, T and CPT symmetries at the Low Energy Antiproton Ring (LEAR) of CERN. From 1989 to 1996, a large amount of data of K^0 and $\overline{K}^0$ decaying into different final states were collected. The neutral kaon system is indeed the most sensitive system in which these discrete symmetries can be tested. Although the K^0 and $\overline{K}^0$ mesons are eigenstates of the strong and the electromagnetic interactions, they are not eigenstates of the weak interaction, which does not conserve the strangeness. Thus, through weak interactions, the K^0 and $\overline{K}^0$ may oscillate into each other. Two mass eigenstates are then created, K^0_S and K^0_L, corresponding to the two possible oscillation modes. Both these particles can decay into the semileptonic $\pi e \nu$ and $\pi \mu \nu$ channels. Moreover, the short living K^0_S and the long living K^0_L were thought to be eigenstates of the CP symmetry. Indeed, K^0_S decays into the $\pi^+\pi^-$ and $\pi^0\pi^0$ final states, eigenstates of CP, with eigenvalue $+1$, while K^0_L decays into $\pi^+\pi^-\pi^0$ and $\pi^0\pi^0\pi^0$ final states, also eigenstates of CP, with eigenvalue -1 if no relative angular momentum in the final state are involved. However, it was discovered in 1964, that K^0_L could also decay into two pions [1]. Hence, the CP symmetry was found to be violated by the weak interaction. At present, the neutral kaon system is still the only system where CP-violation has ever been observed.

Since this discovery, many efforts have been made to understand CP-violation. The CP-violation could be incorporated into the standard model, by introducing complex elements in the quark mass mixing matrix (CKM matrix) [2], although without explaining the origin of the CP-violation. On the experimental side, most of the experiments used K^0_L beams to observe CP-violation. They measured parameters describing the CP-violation in the neutral kaon system, in particular the ratio of the CP-violating to the CP-conserving decay amplitudes in the two pion decays, $\eta_{+-} = A(K_L \to \pi^+\pi^-)/A(K_S \to \pi^+\pi^-)$. The CPLEAR experiment chose to use kaons of known strangeness at the production. The neutral kaons were produced in $p\overline{p}$-annihilations at rest in the processes:

$$\begin{aligned} p\overline{p} &\to K^-\pi^+K^0 \quad \text{and} \\ p\overline{p} &\to K^+\pi^-\overline{K}^0. \end{aligned}$$

The strangeness of the produced K^0 ($\overline{K}^0$) was determined by the charge of the accompanying kaon.

For the different decay channels, the CP-violation parameters were measured by decay rate asymmetries between the two initial strangeness states. In these asymmetries, the absolute acceptances cancel. Only relative acceptances had to be considered. Hence, the detector and the analysis procedures were optimised to minimise unwanted relative effects.

The experiment was performed using a cylindrical detector. The $p\overline{p}$-annihilations were produced in a hydrogen target at the centre of the detector with the $\overline{p}$-beam delivered by LEAR. The particles were detected by tracking devices: 3 proportional chambers, 6 drift chambers, and 2 layers of streamer tubes. The charged kaons were identified by a threshold Čerenkov counter, sandwiched between two scintillators. Finally, the neutral particles were detected in an electromagnetic calorimeter. The whole apparatus was embeded in a magnetic field of 0.44 T.

In this work, a study of the performance of two of the proportional chambers is presented. In particular, the dependence of their efficiencies on geometrical parameters and on the particle momentum were investigated. The mean efficiency of each chamber under data taking conditions was measured to be $(95.97 \pm 0.21)\%$ and $(96.73 \pm 0.21)\%$, respectively. The losses of efficiency due to the dead channels and to the wire supports inside the chambers were also determined. In addition, this study allowed a precise check of the geometrical position of the chambers in the CPLEAR detector. Finally, the results of the same analysis, performed on the simulated data, were found to be in agreement with the real data results.

Apart from the symmetry tests, the large amount of semileptonic data accumulated by CPLEAR also suggested the possibility to measure the $\mathrm{K}^0_{\mathrm{e}3}$ electroweak form factor with small statistical uncertainties. The effect of the form factor shows itself in the kinematical dependence of the K^0 and $\overline{\mathrm{K}}^0$ decay amplitudes. In contrast to the CP-violation parameters, the form factor is not measured in asymmetries. Therefore, the absolute acceptance of the detector had to be fully understood. Only a difference between the $\mathrm{K}^0_{\mathrm{e}3}$ and the $\overline{\mathrm{K}}^0_{\mathrm{e}3}$ form factors could be measured by asymmetries, which would indicate CP-violation in the semileptonic decay amplitudes. However, this is not expected in the standard model of electroweak interactions.

In this thesis, a detailed analysis of the CPLEAR simulation programme performances is presented. Corrections based on calibration data are proposed, in order to improve the quality of the simulation data. Then, the $\mathrm{K}^0_{\mathrm{e}3}$ form factor is determined by comparing the kinematics of the semileptonic $\pi e \nu$ events in real and simulated data. For this purpose, the data selection was optimised to reject unwanted $\pi\mu\nu$, $\pi^+\pi^-$ and $\pi^+\pi^-\pi^0$ backgrounds. The $\mathrm{K}^0_{\mathrm{e}3}$ form factor f_+ was found to depend linearly on the square of the momentum transfer q^2 to the lepton pair, like in previous experiments:

$$f_+(q^2) = f_+(0) \cdot (1 + \lambda_+ \frac{q^2}{m_\pi^2}).$$

The result for the form factor's linear energy dependence parameter λ_+ turned out to be

$$\lambda_+ = 0.0245 \pm 0.0012_{\mathrm{stat}} \pm 0.0029_{\mathrm{syst}}.$$

The uncertainty of this value is similar to those of the most precise published measurements. Taking into account this result, the world average becomes

$$\lambda_+ = 0.0291 \pm 0.0014.$$

Contents

Chapter 1

Introduction

The "strange" particles were discovered in 1947 [3]. In order to include these particles in the zoo of the already known particles, a new quantum number had to be defined, "strangeness" S. The new particles, called kaons in modern terminology, have strangeness values $S = \pm 1$, and for each state of strangeness, the kaon has a charged and neutral component. For $S = +1$, the particles are the positively charged kaon K^+ and the neutral kaon K^0, while for $S = -1$, there is a negatively charged kaon K^- and the anti-neutral kaon $\overline{K}^0$. These particles are created by strong interactions. They may also decay, through the weak interaction, which does not conserve the strangeness S. Here, the attractive feature of the neutral kaons K^0 ($S = +1$) and $\overline{K}^0$ ($S = -1$) appear : they are antiparticles of each other, and they decay weakly into common final states. This suggested that $K^0 \leftrightarrow \overline{K}^0$ transitions might occur, due to the weak interaction. These transitions, or oscillations, are the most sensitive probe for testing discrete symmetries. The CP-violation was indeed discovered in the $K^0 - \overline{K}^0$ system in 1964 [1].

The kaons are mesons, hence, in the quark model, the neutral kaon K^0 ($\overline{K}^0$) is composed of two quarks, an $\bar{s}$- (s) and a d- ($\bar{d}$) quark. This quark structure is governed by the strong interaction. Then, in the weak decays of K^0 ($\overline{K}^0$), the decay amplitude also depends on the strong interaction between the quarks. This effect can be observed in the Dalitz distribution of the neutral kaon decays, and the experimental parameters characterising the structure, the form factors, can be determined.

The purpose of this thesis is to present the measurement of the form factor of the K^0 ($\overline{K}^0$) $\rightarrow \pi e \nu$ decays. Firstly, the phenomenology of the neutral kaon system is presented in Chapter 2. The form factors are also introduced, and the present status on their experimental values is also presented.

The measurement presented in this work was part of the CPLEAR experiment, the main purpose of which was the observation and description of CP-violation. A description of the detector is given in Chapter 3, and an analysis of the CPLEAR proportional chambers performance is presented in Chapter 4.

Following which, the CPLEAR simulation programme, and its performances are discussed (Chapter 5). Corrections are proposed to improve the quality of the simulated events.

From the data selection (Chapter 6), one obtains the final sample of K^0 ($\overline{K}^0$) $\rightarrow \pi e \nu$ events. This sample is then used to determine the electroweak form factor (Chapter 7).

Finally, Chapter 8 presents a summary of the results obtained and draws the conclusion to this work.

Chapter 2

The Neutral Kaon System

2.1 Introduction

The K^0-$\overline{K}^0$ system has very attractive features to test discrete symmetries. Most interesting is the ability of the K^0 and the $\overline{K^0}$ to oscillate into each other through weak interactions. The phenomenology of these oscillations is described in Section 2.2. It is explained how the violation of CP, T and CPT symmetries is included in the phenomenological formalism. Then, the CP-violation in the 2π, 3π and semileptonic decay channels is described in Sections 2.3 to 2.5. Finally, the semileptonic decays are treated in more detail, and the decay amplitude is expressed in terms of form factors (Section 2.6). Note that to simplify the equations, the units $\hbar = c = 1$ are used.

2.2 $K^0 - \overline{K^0}$ Oscillations: Phenomenology

The K^0 and its antiparticle the $\overline{K^0}$ are produced by strong interactions, and they carry strangeness quantum numbers $S = +1$ and $S = -1$, respectively. The associated states $|K^0\rangle$ and $|\overline{K^0}\rangle$ at rest are eigenstates of the strong and electromagnetic interactions:

$$\begin{aligned} H_0 \left|K^0\right\rangle &= m_0 \left|K^0\right\rangle \\ H_0 \left|\overline{K^0}\right\rangle &= \overline{m_0} \left|\overline{K^0}\right\rangle , \end{aligned} \tag{2.1}$$

where $H_0 = H_{\text{strong}} + H_{\text{em}}$ is the Hamiltonian of the strong and the electromagnetic interactions, and m_o ($\overline{m_0}$) is the rest mass of the K^0 ($\overline{K^0}$). CPT invariance of H_0 is assumed, hence, the masses of the two strangeness eigenstates are equal: $m_o = \overline{m_0}$. Due to the strangeness non-conservation of the weak interaction the two states $|K^0\rangle$ and $|\overline{K^0}\rangle$ couple. These states are then not eigenstates of the full Hamiltonian $H = H_0 + H_{\text{weak}}$. In order to determine the eigenstates, one writes the most general state $|\Psi\rangle$ describing the neutral kaon as

$$|\Psi(t)\rangle = a(t)\left|K^0\right\rangle + b(t)\left|\overline{K^0}\right\rangle + \sum_f c_f(t)\left|f\right\rangle , \tag{2.2}$$

where $a(t)$, $b(t)$ and $c(t)$ are time dependent functions. In the neutral kaon rest frame, the relativistic effects can be neglected. Hence, the time evolution of the $|\Psi(t)\rangle$ state is a solution of the Schrödinger equation

$$i\frac{\partial}{\partial t}\left|\Psi(t)\right\rangle = (H_0 + H_{\text{weak}})\left|\Psi(t)\right\rangle . \tag{2.3}$$

Because of the very small coupling constant of the weak interaction with respect to the strong interaction, H_{weak} can be considered as a perturbation of H_0. From perturbation theory, and applying the Wigner-Weisskopf method [4], i.e. neglecting weak interactions between distinct final states, one can write the effective Schrödinger equation independent of the final states $|f\rangle$ [5]:

$$i\frac{\partial}{\partial t}\begin{pmatrix} a(t) \\ b(t) \end{pmatrix} = \Lambda \begin{pmatrix} a(t) \\ b(t) \end{pmatrix}, \tag{2.4}$$

where Λ is represented by a two-by-two complex matrix. This matrix is used to describe the neutral kaon time evolution, including the decay. There is therefore a loss of probability and Λ is not hermitian. However, like for any complex two-by-two matrix, it can be written as the sum of two hermitian matrices M and Γ:

$$\Lambda = M - \frac{i}{2}\Gamma, \tag{2.5}$$

with

$$\text{with} \quad M = \begin{pmatrix} M_{11} & M_{12} \\ M_{12}^* & M_{22} \end{pmatrix} \quad \text{and} \quad \Gamma = \begin{pmatrix} \Gamma_{11} & \Gamma_{12} \\ \Gamma_{12}^* & \Gamma_{22} \end{pmatrix}.$$

M and Γ are called the mass and the decay matrices, respectively. The elements of the mass matrix are given by [5]

$$M_{ij} = m_0\delta_{ij} + \langle i|H_{\text{weak}}|j\rangle + \sum_f \mathcal{P}\left(\frac{\langle i|H_{\text{weak}}|f\rangle\,\langle f|H_{\text{weak}}|j\rangle}{m_0 - E_f}\right), \tag{2.6}$$

where i and $j = 1$ for $\mathrm{K^0}$ and $= 2$ for $\overline{\mathrm{K}}^0$. $\mathcal{P}$ is the principal part, and E_f is the energy of the final state $|f\rangle$. The first order term in H_{weak} corresponds to the direct $\mathrm{K^0} \leftrightarrow \overline{\mathrm{K}}^0$ transitions, while the second order term corresponds to the same transitions through virtual intermediate states.

For the decay matrix Γ, the matrix elements are given by

$$\Gamma_{ij} = 2\pi \sum_f \langle i|H_{\text{weak}}|f\rangle\,\langle f|H_{\text{weak}}|j\rangle \cdot \delta(m_0 - E_f), \tag{2.7}$$

where the delta function expresses the energy conservation in the decay to the real state $|f\rangle$.

It can be shown that the following conditions on the mass and decay matrix elements hold if H_{weak} is invariant under the T, CPT and/or CP transformations [6]:

$$\left|M_{12} - \frac{i}{2}\Gamma_{12}\right| = \left|M_{12}^* - \frac{i}{2}\Gamma_{12}^*\right| \qquad \text{if T is conserved,} \tag{2.8}$$

$$M_{11} = M_{22} \text{ and } \Gamma_{11} = \Gamma_{22} \qquad \text{if CPT is conserved, and} \tag{2.9}$$

$$\left.\begin{array}{c} \left|M_{12} - \frac{i}{2}\Gamma_{12}\right| = \left|M_{12}^* - \frac{i}{2}\Gamma_{12}^*\right| \\ M_{11} = M_{22} \text{ and } \Gamma_{11} = \Gamma_{22} \end{array}\right\} \qquad \text{if CP is conserved.} \tag{2.10}$$

Thus, in the neutral kaon system, CP-violation is always associated with T- or CPT-violation.

From the diagonalisation of Λ, the mass eigenstates of the neutral kaon system can be determined. One obtains two eigenstates, $|\mathrm{K_S}\rangle$ and $|\mathrm{K_L}\rangle$, with eigenvalues λ_S and λ_L, respectively:

$$\begin{aligned}\lambda_S &= m_S - \frac{i}{2}\gamma_S \\ \lambda_L &= m_L - \frac{i}{2}\gamma_L.\end{aligned} \tag{2.11}$$

Using eq. (2.4) one finds that $|\mathrm{K_S}\rangle$ ($|\mathrm{K_L}\rangle$) is a state of mass m_S (m_L) and of decay width γ_S (γ_L). The actual experimental values for these parameters are (from [7] and [8]):

$$\begin{aligned}\Delta m = m_L - m_S = 2\,|M_{12}| &= (0.5274 \pm 0.0029) \times 10^{10}\,\hbar\mathrm{s}^{-1} \\ 1/\gamma_S = \tau_S &= (0.8927 \pm 0.0009) \times 10^{-10}\,\mathrm{s} \\ 1/\gamma_L = \tau_L &= (5.17 \pm 0.04) \times 10^{-8}\,\mathrm{s}.\end{aligned}$$

The eigenstates $|\mathrm{K_S}\rangle$ and $|\mathrm{K_L}\rangle$ can also be expressed as a linear combination of $|\mathrm{K}^0\rangle$ and $|\overline{\mathrm{K}}^0\rangle$ [6] :

$$\begin{aligned}|\mathrm{K_S}\rangle &= \frac{1}{\sqrt{2}}\left[(1-2\varepsilon_{\mathrm{CPT}})\,|\mathrm{K}^0\rangle + (1-2\varepsilon_{\mathrm{T}})e^{-i\varphi_\Gamma}\,|\overline{\mathrm{K}}^0\rangle\right] \\ |\mathrm{K_L}\rangle &= \frac{1}{\sqrt{2}}\left[(1+2\varepsilon_{\mathrm{CPT}})\,|\mathrm{K}^0\rangle - (1-2\varepsilon_{\mathrm{T}})e^{-i\varphi_\Gamma}\,|\overline{\mathrm{K}}^0\rangle\right],\end{aligned} \tag{2.12}$$

with $\varphi_\Gamma = \arg(\Gamma_{12})$. The states $|\mathrm{K_S}\rangle$ and $|\mathrm{K_L}\rangle$ are normalised for $\varepsilon_{\mathrm{CPT}} = \varepsilon_{\mathrm{T}} = 0$, and $\varepsilon_{\mathrm{CPT}}$ and ε_{T} are given by:

$$\begin{aligned}\varepsilon_{\mathrm{CPT}} &= \frac{2i\Delta\Gamma}{4\Delta m^2 + \Delta\Gamma^2}\left(1 + i\frac{2\Delta m}{\Delta\Gamma}\right)(\Lambda_{22} - \Lambda_{11}) \\ \varepsilon_{\mathrm{T}} &= \frac{\Delta m \Delta\Gamma}{4\Delta m^2 + \Delta\Gamma^2}\left(1 + i\frac{2\Delta m}{\Delta\Gamma}\right)\delta_\varphi\end{aligned} \tag{2.13}$$

where $\Delta\Gamma = \gamma_S - \gamma_L$, and δ_φ is defined by the relation:

$$\delta_\varphi = \pi - (\arg(\Gamma_{12}) - \arg(M_{12}))\,. \tag{2.14}$$

Hence, according to eqs (2.8), (2.9) and (2.10), the parameters $\varepsilon_{\mathrm{CPT}}$ and ε_{T} are the CP-violation parameters:

$$\begin{aligned}\varepsilon_{\mathrm{CPT}} \neq 0 \quad &\Leftrightarrow \quad \text{CPT- and CP-violation} \\ \varepsilon_{\mathrm{T}} \neq 0 \quad &\Leftrightarrow \quad \text{T- and CP-violation}\end{aligned}$$

Then, from eq. (2.13), one sees that the CP-violation associated with the T-violation is directly related to the phase difference δ_φ between the mass and the decay matrices. It can also be concluded that the $|\mathrm{K_S}\rangle$ and $|\mathrm{K_L}\rangle$ states are CP-eigenstates if $\varepsilon_{\mathrm{CPT}} = \varepsilon_{\mathrm{T}} = 0$. In this case, the eigenvalues of $|\mathrm{K_S}\rangle$ and $|\mathrm{K_L}\rangle$ are CP$= +1$ and CP$= -1$, respectively, with the convention CP$|\mathrm{K}^0\rangle = |\overline{\mathrm{K}}^0\rangle$, and CP$|\overline{\mathrm{K}}^0\rangle = |\mathrm{K}^0\rangle$.

Eqs (2.12) can also be inverted to express $|\mathrm{K}^0\rangle$ and $|\overline{\mathrm{K}}^0\rangle$ as functions of $|\mathrm{K_S}\rangle$ and $|\mathrm{K_L}\rangle$. Then, with the help of eq. (2.4), one can write the time evolution of an initially pure strangeness state $|\mathrm{K}^0\rangle$:

$$|\mathrm{K}^0(t)\rangle = \frac{1}{\sqrt{2}}\left(|\mathrm{K_S}\rangle\, e^{-i\lambda_S t} + |\mathrm{K_L}\rangle\, e^{-i\lambda_L t}\right), \tag{2.15}$$

and for an initially pure strangeness state $|\overline{\mathrm{K}}^0\rangle$:

$$|\overline{\mathrm{K}}^0(t)\rangle = \frac{1}{\sqrt{2}(1-2\varepsilon_{\mathrm{T}})}e^{i\varphi_\Gamma}\left((1+2\varepsilon_{\mathrm{CPT}})\,|\mathrm{K_S}\rangle\, e^{-i\lambda_S t} - (1-2\varepsilon_{\mathrm{CPT}})\,|\mathrm{K_L}\rangle\, e^{-i\lambda_L t}\right). \tag{2.16}$$

These expressions for $|K_S\rangle$ and $|K_L\rangle$ can then be used to calculate the decay rate $R_f(t)$ ($\overline{R}_f(t)$) of an initially pure $|K^0\rangle$ ($|\overline{K}^0\rangle$) state, decaying into a final state $|f\rangle$:

$$\begin{aligned} R_f(t) &= \left|\langle f\, |H_{\text{weak}}|\, K^0(t)\rangle\right|^2 \\ \overline{R}_f(t) &= \left|\langle f\, |H_{\text{weak}}|\, \overline{K}^0(t)\rangle\right|^2 . \end{aligned} \tag{2.17}$$

These decay rates are the observables which are measured in the CPLEAR experiment.

2.3 Two Pion Decays

The two pion final states $\pi^+\pi^-$ and $\pi^0\pi^0$ are CP-eigenstates, with eigenvalue CP$= +1$[1]. Since K_L has a CP-eigenvalue CP$= -1$, if $\varepsilon_{\text{CPT}} = \varepsilon_{\text{T}} = 0$, the observation of $K_L \to \pi^+\pi^-$ is a sign of CP-violation. Therefore, one defines, in $\pi^+\pi^-$ decays of the neutral kaon, the CP-violation observable parameters η_{+-} as

$$\eta_{+-} = |\eta_{+-}|\, e^{i\phi_{+-}} = \frac{\langle \pi^+\pi^-|\, H_{\text{weak}}\, |K_L\rangle}{\langle \pi^+\pi^-|\, H_{\text{weak}}\, |K_S\rangle}, \tag{2.18}$$

and, in the $\pi^0\pi^0$decays, the corresponding parameter η_{00} as

$$\eta_{00} = |\eta_{00}|\, e^{i\phi_{00}} = \frac{\langle \pi^0\pi^0|\, H_{\text{weak}}\, |K_L\rangle}{\langle \pi^0\pi^0|\, H_{\text{weak}}\, |K_S\rangle}. \tag{2.19}$$

Then, from eqs (2.15), (2.16) and (2.17), one obtains the decay rates for initially pure states $|K^0\rangle$ and $|\overline{K}^0\rangle$:

$$R_{\pi\pi}(t) = \frac{|A_S|}{2}\left[e^{-\gamma_S t} + |\eta_{\pi\pi}|^2 e^{-\gamma_L t} + 2\,|\eta_{\pi\pi}|\, e^{-\frac{\gamma_S+\gamma_L}{2}t}\cos(\Delta m t - \phi_{\pi\pi})\right] \tag{2.20}$$

$$\overline{R}_{\pi\pi}(t) = (1 + 4\text{Re}(\varepsilon_{\text{T}} + \varepsilon_{\text{CPT}}))\,\frac{|A_S|}{2}\cdot\left[e^{-\gamma_S t} + |\eta_{\pi\pi}|^2 e^{-\gamma_L t} - 2\,|\eta_{\pi\pi}|\, e^{-\frac{\gamma_S+\gamma_L}{2}t}\cos(\Delta m t - \phi_{\pi\pi})\right] \tag{2.21}$$

where $A_S = \langle \pi\pi|\, H_{\text{weak}}\, |K_S\rangle$. From these two observable rates $R_{\pi\pi}(t)$ and $\overline{R}_{\pi\pi}(t)$, the asymmetry $A_{\pi\pi}(t)$ is

$$\begin{aligned} A_{\pi\pi}(t) &= \frac{\overline{R}_{\pi\pi}(t) - R_{\pi\pi}(t)}{\overline{R}_{\pi\pi}(t) + R_{\pi\pi}(t)} \\ &= 2\text{Re}(\varepsilon_{\text{T}} + \varepsilon_{\text{CPT}}) - \frac{2\,|\eta_{\pi\pi}|\, e^{-\frac{\gamma_S-\gamma_L}{2}t}\cos(\Delta m t - \phi_{\pi\pi})}{1 + |\eta_{\pi\pi}|^2 e^{-\frac{\gamma_S-\gamma_L}{2}t}}, \end{aligned} \tag{2.22}$$

which is used in the CPLEAR experiment to determine η_{+-} [9] and η_{00} [10]. The results are:

$$\begin{aligned} |\eta_{+-}| &= (2.316 \pm 0.037) \times 10^{-3} \\ \phi_{+-} &= \arg(\eta_{+-}) = 42.5^o \pm 0.7^o \\ |\eta_{00}| &= (2.47 \pm 0.39) \times 10^{-3} \\ \phi_{00} &= 42.0^o \pm 5.9^o \end{aligned}$$

[1] CP($\pi^+\pi^-$)=C($\pi^+\pi^-$)$\cdot$P($\pi^+\pi^-$)= $(-1)^{l_{+-}}\cdot$P(π^+)$\cdot$P(π^-) $\cdot\, (-1)^{l_{+-}} = +1$, for all angular momenta l_{+-} between π^+ and π^-. For that result, the parity of the pion P($\pi^\pm$) $= -1$ was used, and the charge of a state formed by two bosons without spin C($\pi^+\pi^-$) $= (-1)^{l_{+-}}$.

2.4 Three Pion Decays

Two three pion final states exist: $\pi^+\pi^-\pi^0$ and $\pi^0\pi^0\pi^0$. Both states are CP-eigenstates. The CP-eigenvalue of the three charged pion final state ($\pi^+\pi^-\pi^0$) depends on the angular momentum between the pions. If one defines l_{+-} as the angular momentum between π^+ and π^-, and l_0 the angular momentum between the $\pi^+\pi^-$-pair and π^0, the total angular momentum J is therefore restricted to the values

$$|l_{+-} - l_0| \leq J \leq l_{+-} + l_0. \tag{2.23}$$

Because $J = 0$, due to the conservation of angular momentum (K^0 has no spin), eq. (2.23) imposes that $l_{+-} = l_0$. Then, the parity of the final state is not uniquely determined. This parity depends on the angular momentum l_{+-} and on the intrinsic parity of the pions (-1). Hence, the $\pi^+\pi^-\pi^0$ state has a CP-eigenvalue:

$$\begin{aligned} \mathrm{CP}(\pi^+\pi^-\pi^0) &= \mathrm{CP}(\pi^+\pi^-) \cdot \mathrm{CP}(\pi^0) \cdot (-1)^{l_0} \\ &= (+1) \cdot (-1) \cdot (-1)^{l_0} \\ &= -(-1)^{l_{+-}}, \end{aligned} \tag{2.24}$$

where one used the CP-eigenvalue of the $\pi^+\pi^-$ state CP=+1, and the C- and P-eigenvalues of the π^0, C= +1 and P= -1. The CP-eigenvalue of the $\pi^+\pi^-\pi^0$ state thus depends on l_{+-}. It should be noted that the $\pi^0\pi^0\pi^0$ final state is totally symmetric under the exchange of two pions, hence the angular momentum between any two pions is always even. Therefore, the CP-eigenvalue of the $\pi^0\pi^0\pi^0$ state is CP= -1.

Since the masses of the neutral kaon (497 MeV/c^2) and that of the $\pi^+\pi^-\pi^0$ state ($\approx$ 414 MeV/c^2) are close, the high angular momentum states are suppressed due to centrifugal barrier. Therefore, the $l_{+-} = 0$ state is dominant. Similarly to the two pion decays, the CP-violation observable parameter η_{+-0} is defined as

$$\eta_{+-0} = \frac{\langle \pi^+\pi^-\pi^0(\mathrm{CP}=-1)\,|H_{\mathrm{weak}}|\,\mathrm{K_S}\rangle}{\langle \pi^+\pi^-\pi^0\,|H_{\mathrm{weak}}|\,\mathrm{K_L}\rangle}. \tag{2.25}$$

For the $\pi^0\pi^0\pi^0$ final state, the CP-violation parameter η_{000} is

$$\eta_{000} = \frac{\langle \pi^0\pi^0\pi^0\,|H_{\mathrm{weak}}|\,\mathrm{K_S}\rangle}{\langle \pi^0\pi^0\pi^0\,|H_{\mathrm{weak}}|\,\mathrm{K_L}\rangle}. \tag{2.26}$$

From asymmetries, defined analogously to the two pion decays, the values measured at CPLEAR for the CP-violation parameters are [11] [12]:

$$\begin{aligned} \mathrm{Re}(\eta_{+-0}) &= (-2 \pm 8) \times 10^{-3} \\ \mathrm{Im}(\eta_{+-0}) &= (-2 \pm 9) \times 10^{-3} \\ \mathrm{Re}(\eta_{000}) &= 0.18 \pm 0.14 \\ \mathrm{Im}(\eta_{000}) &= 0.15 \pm 0.20 \end{aligned}$$

showing no CP-violation in $\mathrm{K_S} \rightarrow \pi\pi\pi$ decays at the present experimental precision.

2.5 Semileptonic Decays

In contrast to two pion and three pion decays, the semileptonic $\pi\ell\nu$ ($\ell = \mathrm{e}, \mu$) final states are not CP-eigenstates. Furthermore, the states $\pi^+\ell^-\overline{\nu}$ and $\pi^-\ell^+\nu$ can be distinguished by the charge of the lepton ℓ. Then, four decay rates of an initially pure K^0 or $\overline{\mathrm{K}}^0$ can be defined:

$$R_+(t) \equiv R_{\mathrm{K}^0 \to \pi^-\ell^+\nu}(t), \tag{2.27}$$

$$\overline{R}_-(t) \equiv R_{\overline{\mathrm{K}}^0 \to \pi^+\ell^-\overline{\nu}}(t), \tag{2.28}$$

which are allowed by the $\Delta S = \Delta Q$ rule, and

$$R_-(t) \equiv R_{\mathrm{K}^0 \to \pi^+\ell^-\overline{\nu}}(t), \tag{2.29}$$

$$\overline{R}_+(t) \equiv R_{\overline{\mathrm{K}}^0 \to \pi^-\ell^+\nu}(t), \tag{2.30}$$

which are forbidden by the $\Delta S = \Delta Q$ rule, at the time $t = 0$. From these rates, one again define different asymmetries, and determine the parameters ε_T, ε_CPT and the $\mathrm{K_L} - \mathrm{K_S}$ mass difference Δm.

2.6 The K^0_{e3} Form Factor

2.6.1 The K^0_{e3} Matrix element

In this section, the semileptonic decay of the neutral kaon ($\mathrm{K}^0_{\mathrm{e}3}$) are described in more details:

$$\mathrm{K}^0 \to \pi \mathrm{e} \nu, \tag{2.31}$$

where K^0 stands for both K^0 and $\overline{\mathrm{K}}^0$[2]. One defines the particle energies E_K, E_π, E_e, E_ν, the masses m_K, m_π, m_e, m_ν, and the momenta $\boldsymbol{p_K}$, $\boldsymbol{p_\pi}$, $\boldsymbol{p_e}$ and $\boldsymbol{p_\nu}$ of K^0, π, e and ν, respectively. The neutrino mass is assumed to be zero, $m_\nu \equiv 0$, hence, $E_\nu \equiv |\boldsymbol{p_\pi}|$. The four-momenta are denoted by p:

$$p = (E, \boldsymbol{p}) \tag{2.32}$$

The $\mathrm{K}^0_{\mathrm{e}3}$ decay (eq. (2.31)) is characterised by its amplitude $\mathcal{M}$:

$$\mathcal{M} = \left\langle \pi \mathrm{e} \nu \left| H_{\text{weak}} \right| \mathrm{K}^0 \right\rangle. \tag{2.33}$$

This amplitude depends on a lepton current and on a hadron current (cf. fig. 2.1). Due to the left-handed neutrino, the lepton current j_μ has the form

$$j_\mu = \overline{U}_e O_j (1 + \gamma_5) U_\nu, \tag{2.34}$$

where U_e and U_ν are the lepton spinors and $O_j = 1, \gamma_\mu, \sigma_{\mu\lambda}, \gamma_\mu\gamma_5, \gamma_5$ stands for scalar, vector, tensor, axial vector or pseudoscalar coupling. On the other hand, the hadron current depends on the strong interaction between the decaying strange quark and the spectator $\overline{\mathrm{d}}$ (or d) quark. This interaction gives a structure to the kaon. Since this structure is not well known, one parametrizes the hadron current with

[2] All the results in this section apply the same way to K^0 and $\overline{\mathrm{K}}^0$. Moreover, if one assumes the $\Delta I = 1/2$ rule, the form of the expressions are also adapted for the $\mathrm{K}^\pm$ decays [13].

Figure 2.1: Feynman diagram for $\overline{\mathrm{K}}^0 \to \pi^+ \mathrm{e}^- \overline{\nu}$ decay.

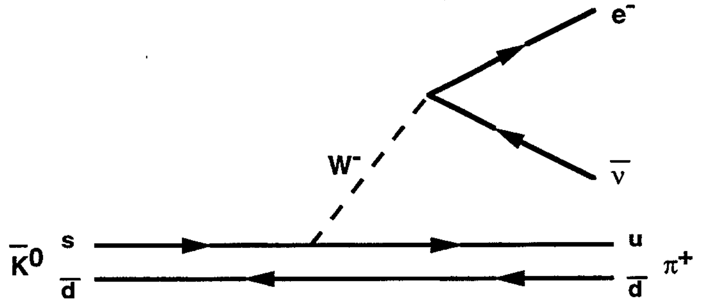

form factors f. Then, the most general matrix element for the K^0_{e3} decay is a mixture of scalar, vector and tensor terms [13]:

$$\begin{aligned}\mathcal{M} = \frac{G}{\sqrt{2}} V_{us} \Bigg[& m_K f_S \overline{U}_e (1+\gamma_5) U_\nu \\ & + \frac{1}{\sqrt{2}} \left[f_+ \cdot (p_K + p_\pi)^\mu + f_- \cdot (p_K - p_\pi)^\mu \right] \cdot \overline{U}_e \gamma_\mu (1+\gamma_5) U_\nu \\ & + \frac{f_T}{2m_K} \left[{p_K}^\lambda {p_\pi}^\mu - {p_K}^\mu {p_\pi}^\lambda \right] \cdot \overline{U}_e \sigma_{\lambda\mu} (1+\gamma_5) U_\nu \Bigg],\end{aligned} \tag{2.35}$$

where G is the Fermi constant, V_{us} is the CKM matrix element coupling the two quarks u and s, f_+ and f_- are the vector form factors, and f_S and f_T are the scalar and tensor form factors. Since the kaon and the pion have no spin, the form factors are functions of only p_K and p_π. It should be noted that no axial-vector term contributes to $\mathcal{M}$, because the two particles K^0 and π have the same intrinsic parity ($P = -1$). If one assumes V-A coupling, then one can omit the scalar and tensor terms. This hypothesis is corroborated by the current experimental limits of the ratios [8] [14]:

$$|f_S/f_+| < 0.04 \quad \text{(CL=68\%)},$$

and:

$$|f_T/f_+| < 0.23 \quad \text{(CL=68\%)}.$$

Hence, one can consider the vector term alone in the expression of $\mathcal{M}$ (eq. (2.35)):

$$\mathcal{M} \propto \left[f_+(q^2)(p_K + p_\pi)^\mu + f_-(q^2)(p_K - p_\pi)^\mu \right] \cdot \overline{U}_e \gamma_\mu (1+\gamma_5) U_\nu, \tag{2.36}$$

where $q = p_k - p_\pi$ is the four-momentum transfer to the eν-lepton pair.

The following discussion explains how this form of the matrix element is obtained: The hadronic amplitude $\langle \pi | H_{\text{weak}} | \mathrm{K}^0 \rangle$ must be formed from the available four-vectors. In the K^0_{e3} decay, the available four-momentum vectors are p_K and p_π. From the two variables p_K and p_π, one cannot construct an axial vector, confirming thus the previously discussed statement that no axial term contributes to the matrix element $\mathcal{M}$. Hence, the hadronic matrix element has the form

$$\langle \pi | H_{\text{weak}} | \mathrm{K}^0 \rangle \propto f_K p_K + f_\pi p_\pi, \tag{2.37}$$

where f_K and f_π are scalar functions of the available Lorentz invariants. In the present case, the only invariant is the four-momentum transfer squared q^2:

$$q^2 = (p_K - p_\pi)^2 = (p_e + p_\nu)^2, \tag{2.38}$$

which can vary in

$$m_e^2 \leq q^2 \leq (m_{K^0} - m_{\pi^\pm})^2 \tag{2.39}$$

Therefore, the form factors f_K and f_π are functions of q^2:

$$\begin{aligned} f_K &= f_K(q^2), \\ f_\pi &= f_\pi(q^2). \end{aligned} \tag{2.40}$$

For reasons which will become clear later, one can transform eq. (2.37) as follows:

$$\left\langle \pi \left| H_{\text{weak}} \right| \mathrm{K}^0 \right\rangle \propto f_+(q^2) \cdot (p_K + p_\pi) + f_-(q^2) \cdot (p_K - p_\pi), \tag{2.41}$$

where $f_+(q^2)$ and $f_-(q^2)$ are linear combinations of $f_K(q^2)$ and $f_\pi(q^2)$:

$$\begin{aligned} f_+(q^2) &= \frac{f_K(q^2) + f_\pi(q^2)}{2} \\ f_-(q^2) &= \frac{f_K(q^2) - f_\pi(q^2)}{2} \end{aligned} \tag{2.42}$$

The term given in eq. (2.41) is the hadronic part of the complete matrix element $\mathcal{M}$ (eq. (2.36)), explaining thus how it was obtained.

2.6.2 Relation to the Experimental Data

In the K^0_{e3} decay, the Dalitz plot distribution can be measured experimentally. The form of the population density ρ over the Dalitz plot can be determined from eq. (2.36), relating thus the experimental to the theoretical distributions [13]:

$$\rho \propto A \cdot f_+^2(q^2) + B \cdot f_+^2(q^2) f_-^2(q^2) + C \cdot f_-^2(q^2). \tag{2.43}$$

Here,

$$\begin{aligned} A &= m_K \left(2E_e E_\nu - m_K E'_\pi\right) + m_e^2 \left(\frac{1}{4}E'_\pi - E_\nu\right), \\ B &= m_e^2 \left(E_\nu - \frac{1}{2}E'_\pi\right), \\ C &= \frac{1}{4} m_e^2 E'_\pi, \end{aligned} \tag{2.44}$$

with

$$E'_\pi = E_\pi^{max} - E_\pi = \frac{m_K^2 + m_\pi^2 - m_e^2}{2m_K} - E_\pi. \tag{2.45}$$

In eqs (2.44), the terms B and C are proportional to m_e^2. Since $m_e^2 \ll m_\pi^2$, B and C are negligible compared to A. Then, eq. (2.43) can be well approximated by

$$\rho \propto A f_+^2(q^2). \tag{2.46}$$

In the case of $\mathrm{K}^0_{\mu 3}$ decays, this approximation would not apply, because $m_\mu \approx m_\pi$. The obtained expression for the Dalitz plot distribution (eq. (2.46)) can be directly compared to the experimental distribution, and the form factor can be extracted.

2.6.3 The dependence of f_+ on q^2

Before measuring the K^0_{e3} form factor, one discusses in this section what the expected dependence of $f_+(q^2)$ on q^2 is. Most experiments assume a linear dependence of f_+ on q^2:

$$f_+(q^2) = f_+(0) \cdot (1 + \lambda_+ \frac{q^2}{m_\pi^2}). \tag{2.47}$$

Because the typical transferred momentum is of the order of the pion mass, the term q^2/m_π^2 is of order of unity. Furthermore, the term $1/m_\pi^2$ makes the linear energy dependence parameter λ_+ dimensionless. It should be noted that a quadratic (or other) dependence is not necessary at the present experimental precision.

From the theoretical side, several independent predictions have been proposed for the parameter λ_+:

1. Gasser and Leutwyler [15], using chiral perturbation theory, obtained $\lambda_+ = 0.030$.
2. Shabalin [16], using the effective Lagrangian method, obtained $\lambda_+ = 0.0328$.
3. Afanasev and Buck [17], using the IBG [18] covariant model for the pion and the kaon, with a given quark-antiquark interaction form, predict $\lambda_+ = 0.028$, without parameter adjustment.
4. Finally, Kalinovsky et al. [19] also obtained $\lambda_+ = 0.028$, on the basis of a phenomenological application of the Dyson-Schwinger equations.

In addition, the theoretically calculated form factor $f_+(q^2)$ appears to be a linear function of q^2 [17]. Hence, the linear parametrisation (eq. (2.47)) is not contradicted by theory.

From the experimental side, 19 independent measurements are listed in ref. [8] (cf. table 2.1), most of them based on a Dalitz plot analysis. The calculated average for λ_+ becomes [8]:

$$\lambda_+ = 0.0300 \pm 0.0016. \tag{2.48}$$

The addition of a quadratic term to $f_+(q^2)$ has also been investigated experimentally. However, it is at the present experimental accuracy compatible with zero.

From table 2.1, one can see that the values scatter considerably, and that the most recent measurement was published in 1981. There is thus a real interest to use new data samples, such as that the ones from the CPLEAR experiment, in order to obtain a new, and if possible more accurate measurement for the form factor $f_+(q^2)$.

Table 2.1: List of the available measurements of the $f_+(q^2)$ linear energy dependence parameter λ_+. The number of events used for each experiment, the year of the publication, and the respective reference are also mentioned.

λ_+	Nb of events	Year	Ref.
0.0306 ± 0.0034	74k	1981	[20]
0.025 ± 0.005	12k	1978	[21]
0.0348 ± 0.0044	18k	1978	[22]
0.0312 ± 0.0025	500k	1976	[23]
0.0270 ± 0.0028	25k	1975	[14]
0.044 ± 0.006	24k	1975	[24]
0.040 ± 0.012	2171	1974	[25]
0.045 ± 0.014	5600	1973	[26]
0.019 ± 0.013	1871	1973	[27]
0.022 ± 0.014	1910	1972	[28]
0.023 ± 0.005	42k	1971	[29]
0.05 ± 0.01	16k	1971	[30]
0.02 ± 0.013	1000	1968	[31]
0.023 ± 0.012	4800	1968	[32]
-0.01 ± 0.02	762	1967	[33]
0.01 ± 0.015	531	1967	[34]
$0.08 + 0.10/-0.08$	240	1967	[35]
0.015 ± 0.08	577	1965	[36]
0.07 ± 0.06	153	1964	[37]
0.0300 ± 0.0016			Average [8]

Chapter 3

The CPLEAR Detector

3.1 Introduction

In this chapter, the CPLEAR detector [38] will be presented. The experimental constraints to measure CP-violation and the solutions adopted are explained in Section 3.2. The details of the detector and its subdetectors are described in the Sections 3.3 to 3.10. In Chapter 4, a detailed analysis of the performance of the two CPLEAR proportional chambers PC1 and PC2 is presented.

3.2 Experimental Requirements and Choices

The aim of the CPLEAR experiment is a precision study of the CP, T and CPT symmetries with neutral kaons of tagged strangeness at the production. The K^0 and $\overline{\mathrm{K}}^0$ may oscillate into each other and eventually decay. The decay channels that are studied by CPLEAR are $\pi^+\pi^-$, $\pi^+\pi^-\pi^0$, $\pi^0\pi^0$, $\pi^0\pi^0\pi^0$, $\pi e\nu$ and $\pi\mu\nu$. In order to study the tiny effect of CP-violation, the initial strangeness of K^0 ($\overline{\mathrm{K}}^0$), the lifetime and the decay channel must be measured accurately and with sufficient statistics. This leads to the following experimental requirements and the corresponding chosen solutions:

1. **The neutral kaons must be produced with a known initial strangeness.** This requirement is satisfied by producing the neutral kaons in $\mathrm{p\overline{p}}$-annihilations at rest in the processes (*Golden Channels*):

$$\begin{aligned} \mathrm{p\overline{p}} &\rightarrow \mathrm{K}^-\pi^+\mathrm{K}^0 \quad \text{and} \\ \mathrm{p\overline{p}} &\rightarrow \mathrm{K}^+\pi^-\overline{\mathrm{K}}^0, \end{aligned}$$

   each of them with a branching fraction of $\approx 0.2\%$. Most of the other annihilation channels are purely pionic (charged and neutral). This choice has the following interesting features:

   - Due to strangeness conservation in the strong interaction, a K^0 ($\overline{\mathrm{K}}^0$) is always associated with a K^- (K^+). This allows the strangeness identification of the neutral kaon by identifying the sign of the charge of the detected kaon.
   - The total energy in these processes is

$$E_{\mathrm{tot}} = 2m_{\mathrm{p}} = (1876.54462 \pm 0.00056)\mathrm{MeV},$$

     which is used as a constraint in the determination of the K^0 ($\overline{\mathrm{K}}^0$) momentum.

2. **The K^0 ($\overline{\mathrm{K}}^0$) lifetime is deduced from the kinematical configuration of the event.** In $\mathrm{p\bar{p}}$-annihilations at rest, the particles are produced isotropically. Moreover, from the fact that a CP-symmetric detector is required in order to minimise systematic effects, a spherical detector would be natural. However, for practical reasons, a cylindrical almost-4π geometry of the detector with the target at its centre is used. A tracking device of radius R around the target provides the measurement of the kinematical configuration of the event. In order to measure the sign and the momentum of the charged particles, the whole volume is embedded in a uniform magnetic field of 0.44 T, parallel to the cylinder axis. The radius R necessary to observe $\mathrm{K_S}$-$\mathrm{K_L}$ interference can be estimated through the following approximation: the interference is observable within a time of about 20 τ_S after the neutral kaon production, and the kaon has a typical momentum of 700 MeV/c ($\Rightarrow$ a velocity $\beta_{\mathrm{K}^\pm} = \frac{v}{c} = 0.81$). This corresponds to a distance of flight d:

$$d = 20 \cdot \beta \cdot c\tau_S = 43.6\,\mathrm{cm},$$

which is, by requirement, the lower bound for the radius R.

3. **The decay channel of the neutral kaon must be recognised.** The charged particles of the decay products ($\pi^+\pi^-$, $\pi^+\pi^-\pi^0$, $\pi e\nu$) also have to be detected. Thus, approximately 20 cm more are necessary, and the chosen radius R for the tracking device must be of the order of 60 cm. A minimum of material inside this volume is required to minimise the regeneration process of neutral kaons. In addition, an e/π-separator and a π^0-identification are needed (cf. following points).

4. **Charged kaon identification.** The recognition of a charged kaon is a good signature for the *Golden Events* (cf. point 1), as $\mathrm{p\bar{p}}$-annihilations at rest have produced mainly pions. Then, a good particle identification detector (PID) is necessary. The chosen solution is a threshold Čerenkov counter (C) surrounded by two scintillators (S1 and S2) placed outside the tracking device. Indeed, all charged particles give light in the scintillators, though only fast particles give light in the Čerenkov counter. Therefore, since kaons are heavier and thus slower than pions, they are not detected by the Čerenkov counter, even though pions are. Thus, kaons are characterised by a S1·$\overline{\mathrm{C}}$·S2 signal, while pions give S1·C·S2. This difference is used to distinguish these particles. In addition, the information provided by the PID is also used in the e/π-separation necessary for semileptonic event identification (cf. Section 6.3.2).

5. **Detection of events containing neutral pions.** Some decay channels contain neutral pions ($\pi^+\pi^-\pi^0$, $\pi^0\pi^0$, $\pi^0\pi^0\pi^0$). The photons resulting from their decay are detected by an electromagnetic calorimeter placed between the PID and the magnet.

6. **Necessity for high statistics.** A high rate of $\mathrm{p\bar{p}}$-interactions ($\approx$ 1MHz) counteracts the small branching fraction of the *Golden Channel* and provides the high statistics needed by the experiment. The online selection of this small fraction of *Golden Events* is performed by a dedicated multilevel trigger which reconstructs the desired events and rejects the unwanted ones. The rejection by a factor, close to 2000, reduces the trigger rate to a few hundred Hertz.

The CPLEAR detector was built according to the choices mentioned above. Figure 3.1 shows the detector layout. The characteristics of each subdetector are now briefly discussed. A more detailed description can be found in ref. [38].

3.3 Coordinate System

The origin of the coordinate system is at the centre of the detector. The $\bar{\mathrm{p}}$-beam direction, which is aligned with the axis of the cylinder, as well as the magnetic field, corresponds to the z-coordinate, with

Figure 3.1: The CPLEAR detector layout (longitudinal view). The antiprotons enter from the left side and stop in the hydrogen target at the centre of the detector.

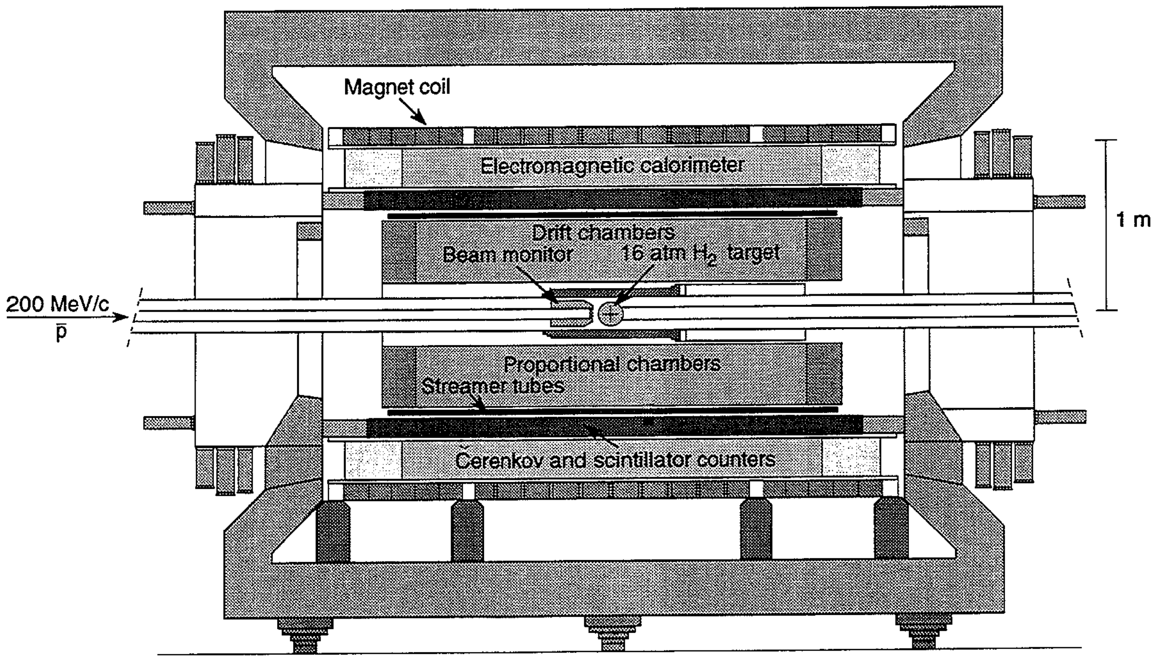

positive z downstream. The y-axis is vertical and points upwards, while the x-axis is horizontal, with positive x such that the coordinate system is right-handed.

In the xy-plane, called *transverse plane*, polar coordinates r and ϕ are natural since each subdetector corresponds to a constant r. In this plane, the transverse momentum p_t ([MeV/c]) is determined by the track-curvature R ([cm]) of the particle, its charge q (in units of the electron charge) and the magnetic field B ([kG]=[10^{-1}T]) (cf. e.g. [8, §24.8]):

$$p_t = 0.3qBR.$$

For practical reasons, the transverse plane was divided into 32 sectors, and 64 mini-sectors.

Finally, the r- and z-coordinates define the *longitudinal plane*, in which the z-component p_z of the momentum is determined.

3.4 Beam and Target

From 1989 to 1996, a 200 MeV/c $\bar{p}$-beam was provided by the CERN Low Energy Antiproton Ring (LEAR) to the CPLEAR experiment at a rate of $\approx$ 1 MHz. After entering the detector, the antiprotons passed through two orthogonal Multi-Wire Proportional Chambers (MWPC) which monitored the beam profile. Then, a beryllium degrader reduced the momentum of the antiprotons so that they were stopped inside a hydrogen target. Between the degrader and the target, a scintillator (the Beam Counter) provided the "start" signal to the trigger electronics. While the antiprotons stop in the hydrogen, they form $p\bar{p}$-atoms before annihilating, such that the reactions occur at rest. Two different targets were used in the CPLEAR detector: until spring 1994, a spherical target of radius 7 cm filled with 16 bar gaseous hydrogen was used, and since then a 1.2 cm cylindrical target filled with 26 bar gaseous hydrogen.

3.5 Tracking Devices

The tracking was performed, from the inside to the outside, by Multi-Wire Proportional Chambers, which provided fast information about the event configuration to the trigger, six Drift Chambers, for a good resolution in both transverse and longitudinal planes, and two Streamer Tube layers, for further good z-resolution and fast information to the trigger.

3.5.1 Proportional Chambers (PC)

PC0: Half of the recorded events were collected in 1995 with the cylindrical target, surrounded by a cylindrical Proportional Chamber (PC0) of 1.5 cm radius at the wire plane. PC0 was used to select events where the neutral kaons decayed after PC0, to ensure a sufficient separation between the production and decay vertices and thus removing $p\bar{p}$-annihilation background.

PC1 and PC2: These two Proportional Chambers were built to provide fast information about the event configuration to the trigger. They were 70 cm long cylinders of 9.525 cm (PC1) and 12.7 cm (PC2) radius at the wire-plane. More informations and a detailed study of their performance (efficiency) is presented in Chapter 4.

3.5.2 Drift Chambers (DC)

Outside the PCs were the six 2.34 m long Drift Chambers (DC1 to DC6) with radii between 25 cm and 51 cm (table 3.1). Drift-cells of only 5 mm ensured a drift time shorter than 120 ns in a gas mixture made of 50% Ethane and 50% Argon. Left-right ambiguities were avoided by using sense-wires doublets, separated by 0.5 mm. The electrostatic repulsion at the operating voltage of 2200 V was overcome by gluing spacers, made of 1 mm epoxy balls, placed every 20 cm along the wire doublets. The cathode strips of DC1, DC2, DC4 and DC6 were used for the determination of the z-coordinate of the tracks. The total amount of material in the DCs was equivalent to $7 \cdot 10^{-3}$ radiation lengths (X_0) and the resolution achieved was $\approx 300\,\mu$m in the transverse plane and ≈ 3 mm in the longitudinal plane. The mean wire efficiency was about 95%.

Table 3.1: Drift Chambers geometrical parameters.

Chamber	Mid-plane radius [cm]	Active length [cm]	Number of wires	Number of U-strips (inner cathode)	Number of V-strips (outer cathode)
DC1	25.46	234	160	275	285
DC2	30.56	234	192	324	336
DC3	35.65	234	224	378	385
DC4	40.74	234	256	424	432
DC5	45.84	234	288	465	477
DC6	50.95	234	320	510	520

3.5.3 Streamer Tubes (ST)

Further outwards, two layers of 192 Streamer Tubes, 2.52 m long, were situated at radii between 56.8 cm and 62.0 cm (table 3.2), and provided a fast read-out of the longitudinal z-position for every charged track, by measuring the time difference of the signal arriving at both ends of the tube. A 50% isobutane, 46% argon and 4% methylal gas mixture provided an efficiency of 98.2% per layer and a z-resolution of 1.4 cm when operating at a voltage of $\approx$ 4100 V.

Table 3.2: Streamer Tubes geometrical parameters.

Chamber	Mid-plane radius [cm]	Active length [cm]	Number of tubes
ST1	58.22	252	$32 * 6$
ST1	59.97	252	$32 * 6$

3.6 Particle Identification Detector (PID)

As was seen in Section 3.2, the kaons were identified by using a Čerenkov counter (C) surrounded by two scintillators (S1 and S2). This constituted the Particle Identification Detector (PID). It was composed of 32 modules, one per sector, each of 3.1 m length and with radii between 62.5 cm and 75 cm (table 3.3). The light produced by the particles was collected and amplified at both ends of the PID by a total of 256 photo-multipliers (two at each end for a Čerenkov module, and one at each end for each scintillator module). The first scintillator (S1), 3 cm thick, was also used for $\mathrm{d}E/\mathrm{d}x$ and time-of-flight (TOF) measurements. The Čerenkov counter was 8 cm thick and filled with C_6F_{14} liquid whose refractive index was such that particles with velocities below $\beta = 0.81$ did not give light (kaons in this experiment). This threshold velocity, being very sensitive to external factors such as temperature or aging, needed a time-dependent calibration. The calibration was performed by analysing minimum-bias data, once per day. The second scintillator (S2), 1.4 cm thick, was mainly used to check that the particles passed completely through the Čerenkov counter of the same module. The efficiency of the S1$\cdot\overline{\mathrm{C}}\cdot$S2 method for kaon identification was found to be $\approx$ 75% for momenta larger than 350 MeV/c.

Table 3.3: PID geometrical parameters.

Chamber	Mid-plane radius [cm]	Active length [cm]	Thickness [cm]	Number of elements
S1	63.84	310	3.0	32
C	69.43	310	8.0	32
S2	74.21	310	1.4	32

3.7 Electromagnetic Calorimeter (ECAL)

The Electromagnetic Calorimeter (ECAL) [39] was designed to detect photons produced by neutral pion decays, and was also used for e/π-separation. It was 2.64 m long, placed after the PID, and covering

75% of the solid angle. The ECAL was made of 18 layers of lead plates (converter) and 18 sampling chambers (a total of 17112 wires). The $\approx$ 8 tons of the ECAL corresponded to $\approx$ 6 radiation lengths, enough for stopping photons of less than 500 MeV in energy, as was predominantly the case in the CPLEAR experiment. The obtained energy resolution in the ECAL was $\sigma(E)/E \approx 0.13\%/\sqrt{E(\mathrm{GeV})}$ and the spatial resolution of the photon conversion point was found to be $\approx$ 5 mm.

3.8 Magnet

The outermost element of the CPLEAR detector was its magnet. It provided an uniform magnetic field of 0.44 T parallel to the z-axis. The possibility to change the sign of this field was necessary to control the systematic effects due to the residual CP-asymmetries of the detector.

3.9 Trigger

A multilevel hardwired processor system (HWP) performed the fast selection of the good events [40]. After the "start" signal, provided by the Beam Counter, the selection involved five steps (fig. 3.2):

1. The **Early Decision Logic (EDL)** requested at least two charged tracks ($\geq$ 2 S1) and at least 1 kaon candidate ($\geq$ 1 S1$\cdot\overline{\mathrm{C}}\cdot$S2). Using the DCs wire information, the transverse momentum (p_T) of the kaon candidates was determined and required to be larger than a minimum of 270 MeV/c, in order to reject false kaons. Since 1995, PC0 was used at this level to reject $\mathrm{p\overline{p}}$-annihilation background by asking for exactly two tracks in that chamber.

2. The **Intermediate Decision Logic (IDL)** performed a first pattern recognition on charged tracks and classified them into *primary* and *secondary* tracks, depending on whether they had at least one hit in one of the PCs or not.

3. The **HWP1** computed the track parameters and rejected events which did not match the *Golden Event* hypothesis.

4. The **HWP2** improved the charged kaon identification and selection by using the $\mathrm{d}E/\mathrm{d}x$ and TOF informations from the S1.

5. The **HWP2.5** determined the number of showers detected in the ECAL. This information was used to select *Golden Events* whose neutral kaon decayed into a state containing neutral pions, and which had thus only two charged tracks.

As already mentioned, a rejection factor close to 2000 was achieved, reducing the trigger rate to a few hundred Hertz.

3.10 Data Acquisition System (DAQ)

A fast and efficient information transfer between the subdetectors and the trigger was required to reach the needed read-out rate. Therefore, the following communication protocol was designed.

Each subdetector digitised the information it had collected and stored it until a command was sent by the trigger. Schematically, four types of commands were possible:

1. Start data taking: a new $\overline{\mathrm{p}}$ was detected by the Beam Counter.

2. Send useful informations to the trigger.

Figure 3.2: Description of the trigger decision procedure.

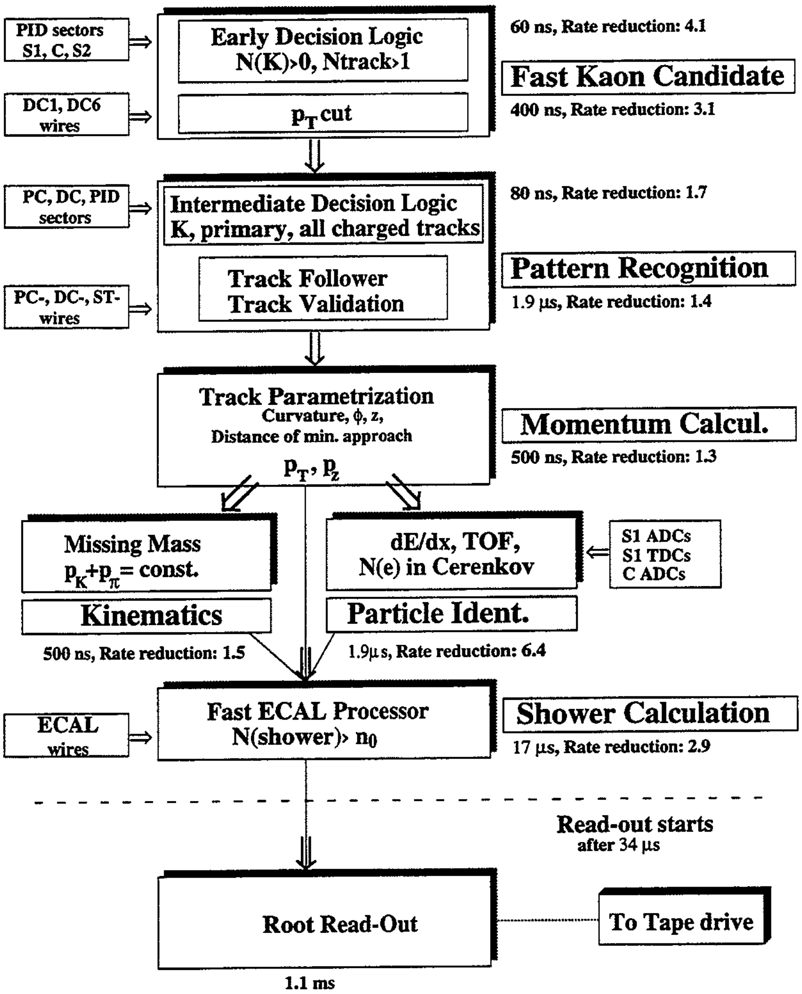

3. Clear the stored data and wait for the next coming event signal.

4. Good event: read-out the stored data.

Each time a read-out signal was sent, every Front-End electronics sent its data to its "Root Read-Out System" (RRO) which formated the data into a standard form. Then, the Event Builder collected all these informations from all the subdetector RROs and compiled them into one single event of ≈ 2 Kb. The events were then sent to tapes of 200 Mb capacity at a rate of about 400 Hz. A small sample was also analysed for the online monitoring. A full event analysis was performed online for this sample to check the detector performance and the data quality.

Chapter 4

The Proportional Chambers: Performances

4.1 Introduction

In this Chapter are presented the results of an analysis of the performance of the two CPLEAR proportional chambers PC1 and PC2. Firstly, a brief introduction to the general operating principles of the Multi-Wire Proportional Chambers (Section 4.2) is given. Then, the characteristics specific to PC1 and PC2 are treated (Section 4.3). Finally, their performance are analysed (Section 4.4).

4.2 Operating Principles

The task of the Multi-Wire Proportional Chambers (MWPC), as for any tracking detector, is to determine the spatial position of the particles crossing their active region, by measuring the electric signal triggered by their charge. The shape and the intensity of this signal might also be used for particle identification. This measurement should be done with a minimal amount of material, to avoid particle scattering and absorption. To achieve this goal, the MWPCs are built according to the following general principles.

The charged particles pass through a gas mixture, in which ionizations occur through energy-loss processes, creating primary electron-ion pairs along their tracks. In order to collect these charges, and to create the detectable signal, an electric field separates the electrons from the positive ions. They are collected at the anode and the cathode, respectively. However, given the number of primary pairs alone, this would not be sufficient to generate a distinguishable signal from random noise. Therefore, a purposely strong electric field accelerates the electrons and gives them enough energy to produce secondary ionization pairs. Thus, an avalanche is trigged leading to a detectable signal.

In practice, thin wires (the anode) are placed between two planar cathode walls (fig. 4.1). The anode is connected to the ground (0 V) while the cathode voltage V_0 is set to a negative voltage of a few kV. This creates an electric field which increases in strength from the cathode to the anode. The maximum of the field E_{wire} is obtained close to the surface of the wires (cf. refs [41], [42], [43]):

$$E_{wire} = \frac{CV_0}{2\pi\epsilon_0}\frac{1}{r_a}, \tag{4.1}$$

where r_a is the wire radius (7.5 μm in PC1 and PC2) and C is the capacitance per unit length of the anode wire with respect to the cathode [41]:

$$C = \frac{2\pi\epsilon_0}{\frac{\pi l}{s} - ln(\frac{2\pi r_a}{s})}, \tag{4.2}$$

Figure 4.1: Transverse view of a cylindrical proportional chamber.

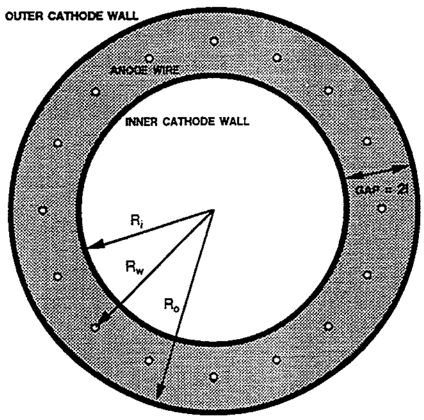

where l is the half-gap between the cathode walls, and s is the separation between 2 consecutive wires.

For the CPLEAR MWPCs PC1 and PC2, the corresponding parameters are given in table 4.1 and lead to a capacitance

$$C = 4.4578 \cdot 10^{-12}\,\mathrm{Fm}^{-1}$$

and to a maximum electric field

$$E_{wire}(2700V) = 28312.5\,\mathrm{kVm}^{-1}$$

at the nominal voltage of 2700 V. Such an electric field is sufficient to give an electron the necessary energy of 26 eV to ionize argon atoms, within less than 1 μm, and thus trigger the avalanche process.

The properties of the gas used in such chambers are also very important. It must have a low ionization potential to allow a high primary and secondary ionization rate. This is achieved by using a noble gas as the main component. Argon is the most commonly used because of its low cost. However, although the avalanche would be efficiently created, the process would diverge. A continuous discharge would appear, because the exited and ionized atoms would return to their ground state by emitting photons. These photons would be energetic enough to extract new electrons from the cathode, thus maintaining the discharge. In order to counteract this effect, a quencher gas is added to the argon. The quencher is usually a polyatomic gas (isobutane C_4H_{10} in PC1 and PC2), which absorbs the photons emitted by the de-excitation of the Argon atoms over a large energy range. A third component is added to the gas mixture, in order to reduce the mean free path of the electrons, and thus avoid that the avalanche propagates to more than one or two wires, thus reducing the spatial resolution. This is achieved by adding a small amount of an electronegative gas (freon 13B1 (CF_3Br) in PC1 and PC2). The proportions and the components of the final gas mixture were chosen after an extensive study [41] and re given by the volume fractions, for PC1 and PC2:

argon:	79.5%
isobutane:	20.0%
freon:	0.5%.

This gas mixture gave the best signal amplification, without electric discharge. The signal amplification is characterised by the gas gain G, defined as the ratio

$$G = \frac{N}{n_0}, \tag{4.3}$$

where N is the total number of charges collected, forming the signal, and n_0 is the number of primary electron-ion pairs created. In order to calculate G, α is defined as the probability of ionisation per unit path length, due to the passage of an electron,

$$\alpha = \frac{1}{\lambda}, \tag{4.4}$$

where λ is the mean free path. λ depends on the nature of the gas, as well as on the electric field E. So, α is also a function of E, itself dependent on the position x. Thus $\alpha = \alpha(x)$. There will then be

$$\mathrm{d}n = n\alpha(x)\mathrm{d}x \tag{4.5}$$

electrons created along a path $\mathrm{d}x$ for n initial electrons. In a simple cylindrical geometry, with one single wire, the total number of electrons N is then by integration

$$N = n_o \exp\left[\int_{r_a}^{r_b} \alpha(x)\mathrm{d}x\right], \tag{4.6}$$

where r_a is the wire radius and r_b is the cathode inner wall radius. Hence, from eqs (4.3) and (4.6)

$$\boxed{G = exp\left[\int_{r_a}^{r_b} \alpha(x)\mathrm{d}x\right].} \tag{4.7}$$

Different models were proposed to describe the form of $\alpha(x)$. Rose and Korff [44] e.g. proposed

$$\frac{\alpha}{p} = A\exp\left(-\frac{Bp}{E}\right), \tag{4.8}$$

where p is the gas pressure, E the electric field, A and B are gas-dependent constants.

4.3 PC1 and PC2 Characteristics

The CPLEAR proportional chambers PC1 and PC2 were built to provide the trigger with fast information about the event configuration. They were 70 cm long cylinders of 9.525 cm (PC1) and 12.7 cm (PC2) radius at the wire-plane. Each chamber had a wire spacing of 1.039 mm so that PC1 and PC2 had 576 and 768 wires, respectively. The 15 μm diameter wires made of gold-plated tungsten were placed in a 6 mm gap between the inner and outer walls, and filled with agas mixture of 79.5% argon, 20% isobutane and 0.5% freon 13B1 (proportions by volume). The 2 mm thick walls were made of a sandwich structure of aluminized kapton-foils, used as cathodes, rohacell foam used as support, and aluminised kapton-foils again. Each chamber had a total surface density of 41.5 mg/cm^2, corresponding to $1.1 \cdot 10^{-3}$ radiation lengths (X_0). The voltage between the anode and the cathode was set between 2600 V and 2750 V. In order to counteract the repulsive electrostatic forces between the wires, two rohacell wire-support rings were included 17 cm and 15 cm, from the centre of PC1 and PC2, respectively. The main geometrical characteristics are summarised in table 4.1.

Table 4.1: Proportional Chambers PC1 and PC2 characteristics (cf. fig. 4.1).

characteristic	PC1	PC2
Inner cathode radius R_i	92.25 mm	124.00 mm
Wires plane radius R_w	95.25 mm	127.00 mm
Outer cathode radius R_o	98.25 mm	130.00 mm
Gas gap ($= 2l$)	6.00 mm	6.00 mm
Wire spacing s	1.039 mm	1.039 mm
Number of wires	576	768
Wire diameter ($= 2r_a$)	15 μm	15 μm
Active length L	700.0 mm	700.0 mm
Covered solid angle [sr]	$0.965 \cdot 4\pi$	$0.940 \cdot 4\pi$

4.4 Efficiency of PC1 and PC2

4.4.1 Introduction

The influence of various geometrical parameters such as z, ϕ, and the track inclination angle α_T on the efficiency of the proportional chambers PC1 and PC2 was studied. The dependence of the efficiency on the track total momentum p_0, the cluster-size CS and the polarity of the magnetic field were also investigated. The data used were "minimum bias" (trigger T1) events taken using two different target geometries: that of run period P26, using the spherical gas target and that of period P29, using the cylindrical high-pressure target together with the chamber PC0. Both geometries were found to give compatible results. These results were then used to check the simulation data description of the proportional chambers (PCs).

4.4.2 Method

The efficiency is determined by comparing the number of reconstructed tracks which have all eight tracking chamber hits to those which have only seven hits, where the missing hit is in one of the proportional chambers. It is assumed that the pattern-recognition and track-fitting programmes reconstruct 7- and 8-hit tracks with the same efficiency. One defines η_i as the efficiency of the i^{th} chamber (PC1 to DC6). Then the probability for a track to have eight hits is given by

$$P_8 = \prod_{i=1}^{8} \eta_i,$$

and the probability to have seven hits with the i^{th} chamber missing is

$$P_{7i} = P_8 \cdot \frac{1 - \eta_i}{\eta_i}$$

If the observed number of 8-hit tracks is A_8 and 7-hit tracks is A_{7i} (one hit missing in i^{th} chamber), then

$$A_8 = N \cdot P_8 \qquad \text{and} \qquad A_{7i} = N \cdot P_{7i},$$

where N is the number of tracks crossing the active part of the detector. A_8 and A_{7i} are the measurable quantities. One deduces that

$$N = \frac{A_8}{P_8}$$

and

$$A_{7i} = \frac{A_8}{P_8} \cdot P_{7i} = A_8 \cdot \frac{1-\eta_i}{\eta_i}$$

Finally,

$$\boxed{\eta_i = \frac{A_8}{A_8 + A_{7i}}} \tag{4.9}$$

The number of successful observations A_8 follows a binomial distribution for a total of $N = A_8 + A_{7i}$ independent observations. Then the unbiased variance of η_i is

$$\boxed{\sigma_i^2 = \frac{A_8 \cdot A_{7i}}{(A_8 + A_{7i})^2 \cdot (A_8 + A_{7i} - 1)}} \tag{4.10}$$

4.4.3 Input Data

In order to avoid any bias due to the efficiencies of the chambers being used as a data selection criterion, only "minimum bias" trigger T1 data were used. All the runs analysed from periods P26 (spring 1994) and P29 (summer 1995) had constant PC running conditions (HV = 2650V, threshold voltage for the output signal $V_{\text{threshold}}$ = 3.0V and constant gas mixture). For the simulation data, true pions were selected from trigger T23 semileptonic golden events, also based on period P25 conditions, in order to simulate as close as possible the trigger T1 characteristics. The data used are summarised in table 4.2.

Table 4.2: Selected raw and simulated data (Monte-Carlo) used in the study.

P26 data	P29 data	P25 Monte-Carlo
27 M1 runs	21 M1 runs	25 M1 runs
27 M2 runs	20 M2 runs	0 M2 runs

4.4.4 Analysis Programme

The raw data from each run were first processed by reconstructing the tracks of each event using the pattern recognition and the track-fitting programmes (version 5) and then written-out in MINRAW format. The efficiency analysis is then performed on the MINRAW data by a separate programme which applies the following selection criteria:

1. For each track the parameters of "closest approach" to the centre of the detector, in the transverse plane (EPSFIT), and in the longitudinal plane (Z00FIT), are computed and the following cuts applied:

   $$|\text{EPSFIT}| \leq 3.0\,\text{cm} \qquad\qquad |\text{Z00FIT}| \leq 5.0\,\text{cm}$$

   No significant change in the results was found when a cut at 0.5 cm was applied to both parameters.

2. A track is kept if it contains 7 or 8 hits (not counting the streamer tubes). If it has 7 hits, the missing chamber must be one of the PCs.

3. The cluster-size (CS) of the hits in the PCs and the track inclination angle (α_{T}) with respect to the perpendicular, at the crossing point of the wire plane in the transverse projection are determined. Then for each of the variables ϕ, z, p_0 and $\cos\alpha_{\mathrm{T}}$ and for each chamber, two histograms are filled. One contains events with 8 hits (providing the A_8 observable) and the other with only 7 hits (providing the A_{7i} observable for chamber i only). Finally the efficiency histogram for each variable and chamber (figs 4.2, 4.4, 4.7 and 4.8) is obtained by applying equations (4.9) and (4.10) to the relevant pair of histograms on a bin-by-bin basis.

4.4.5 Mean Efficiency

The mean efficiency of each of the chambers was computed by leaving the total momentum p_0, the z at the crossing point and the angle α_{T} as free parameters. Thus the mean efficiency in the standard data taking detector configuration is obtained. Table 4.3 shows the number of tracks observed with eight

Table 4.3: Number of tracks having 7- or 8-hits, for magnetic field polarities M1 and M2.

A_8	M1	M2	A_{7i}	M1	M2
PC1	1899376	1761020	PC1	80375	73242
PC2	1899376	1761020	PC2	63952	59621

hits (A_8) or seven hits (A_7) in PC1 and PC2 for both magnetic field polarities (M1 and M2). These values give the following efficiencies:

$$\Rightarrow \eta_{\mathrm{PC1}}(\mathrm{M1}) = (95.940 \pm 0.014)\% \qquad \eta_{\mathrm{PC1}}(\mathrm{M2}) = (96.007 \pm 0.014)\%$$
$$\Rightarrow \eta_{\mathrm{PC2}}(\mathrm{M1}) = (96.743 \pm 0.013)\% \qquad \eta_{\mathrm{PC2}}(\mathrm{M2}) = (96.725 \pm 0.013)\%$$

The above quoted uncertainties are purely statistical. The trigger T1 data were however taken over an extended period of time and therefore subject to fluctuations in detector conditions, beyond a purely statistical nature. An estimate of the uncertainty introduced by such effects gave an additional uncertainty contribution of $\pm 0.21\%$ [1]. Thus, it can be concluded that within the uncertainties the efficiencies are independent of the magnetic field polarity and that the mean efficiencies of the PCs, under the specified running conditions are:

$$\eta_{\mathrm{PC1}} = (95.97 \pm 0.21)\%$$
$$\eta_{\mathrm{PC2}} = (96.73 \pm 0.21)\%.$$

Specifying that the tracks should cross the chambers with an angle α_{T} such that $\cos\alpha_{\mathrm{T}} > 0.995$ causes the efficiencies to increase to (96.18±0.21)% for PC1 and (96.84±0.21)% for PC2 (see Section 4.4.12).

The trigger however uses the PCs information in an "OR" logic, such that a track is recognised as a "primary" at the IDL level if *"PC1 OR PC2"* have a hit. This then gives the relevant combined PC efficiency of

$$\eta = 1 - (1 - \eta_{PC1}) \cdot (1 - \eta_{PC2}) = (99.87 \pm 0.01)\%.$$

During the P26 data taking period, PC1 had 8 dead channels (in 576) and PC2 had 5 (in 768). This corresponds to a loss of efficiency of 1.39% for PC1 and 0.65% for PC2. This then gives the intrinsic efficiencies of $\eta_{\mathrm{PC1}} = (97.36 \pm 0.21)\%$ and $\eta_{\mathrm{PC2}} = (97.38 \pm 0.21)\%$ (see also Section 4.4.10).

[1] The variance of the distribution of the efficiencies measured for each run is a measure of these fluctuations, convoluted with the statistical uncertainty. The latter are known and have been deconvoluted to obtain the uncertainty due to fluctuations.

4.4.6 ϕ-dependence of the Efficiency

The plots of figure 4.2 show the ϕ-dependence of the efficiency (64 bins, each corresponding to a chamber sector, i.e. 9 wires/sector for PC1 and 12 wires/sector for PC2). The inefficient sectors are unambiguously related to the dead channels. The frequency plots (fig. 4.3) are constructed from the ϕ-plots and show the scattering of efficiencies about their means. The mean efficiencies as determined from the frequency plots are consistent with those obtained using the method outlined in Section 4.4.2 (equations (4.9) and (4.10)) and thus serve as a consistency check.

Figure 4.2: Efficiency versus ϕ in PC1 and PC2.

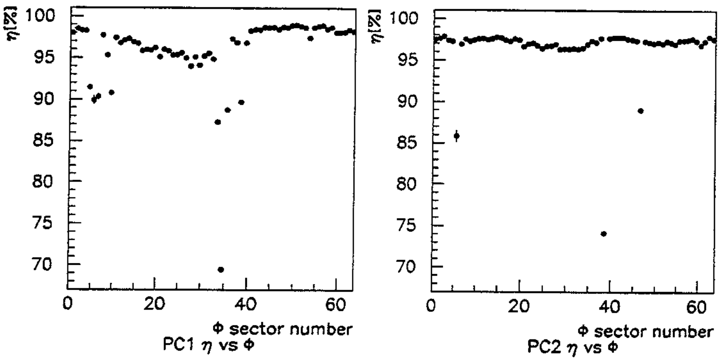

Figure 4.3: Frequency plots of the efficiencies in the ϕ-distributions.

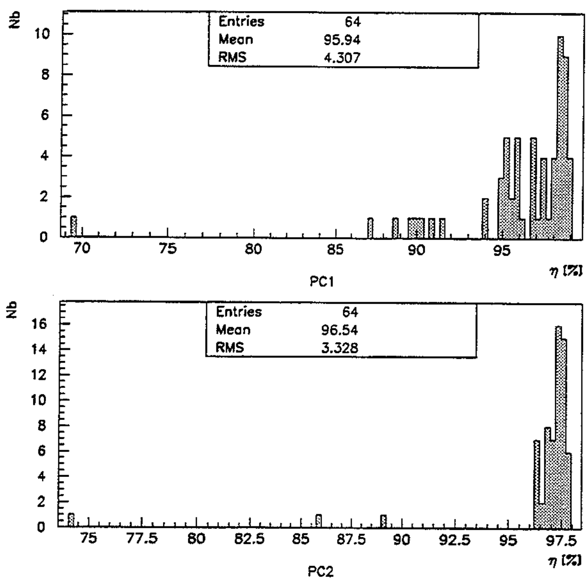

4.4.7 Z-dependence of the Efficiency

Figure 4.4 shows the efficiencies of PC1 and PC2 as a function of the z-position of the track when crossing the chamber. The track selection was the following: p_0 was left free and the angle α_T had to fulfil the condition $\cos\alpha_T > 0.995$, in order to remove tracks with significant transverse momentum. The two "spacers" [41], to which the anode wires are attached, in order to counteract the repulsive electrostatic force between neighbouring wires, can clearly be seen and their positions used to perform several checks. Firstly, since these spacers have geometrically fixed positions, they can be used as a sensitive and relatively bias-free [2] test of magnetic field polarity invariance, by comparing their positions as reconstructed by tracks from both field polarities M1 and M2. Secondly, the longitudinal positions of the chambers and their active lengths can be checked. Finally, the efficiency loss due to the spacers can also be checked.

Figure 4.4: Efficiency versus z in PC1 and PC2.

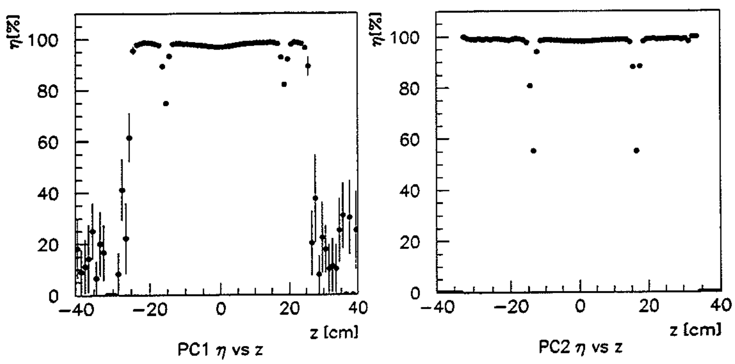

4.4.8 Position of the Spacers

By fitting an inverted Gaussian to the z-efficiency profiles (e.g. fig. 4.5), the positions and separations of the spacers could be determined (table 4.4) and the above mentioned checks performed. By looking

Table 4.4: Position of the spacers, their separations and the deduced z-shifts.

Field	Chamber	First spacer [mm]	Second spacer [mm]	Separation [mm]	z-shift [mm]
M1	PC1	-156.11 ± 0.09	185.28 ± 0.14	341.39 ± 0.17	14.59 ± 0.08
	PC2	-137.05 ± 0.05	164.79 ± 0.04	301.84 ± 0.06	13.87 ± 0.03
M2	PC1	-155.73 ± 0.09	185.68 ± 0.14	341.41 ± 0.17	14.98 ± 0.08
	PC2	-136.91 ± 0.04	164.94 ± 0.04	301.85 ± 0.06	14.02 ± 0.03

at the difference (M1-M2) for each of the two spacers, the magnetic field polarity invariance can be tested. The values are consistent for each chamber but non-zero with a significance of $(2.0 - 2.9)\sigma$ corresponding to a confidence level of $(2.3 - 0.2)\%$, thus showing an incompatibility between M1 and M2 at this level.

[2]The only known biases are: the magnetic field knowledge, the pattern recognition logic and the track fitting procedure.

Figure 4.5: M1-fits of the z-positions of the spacers.

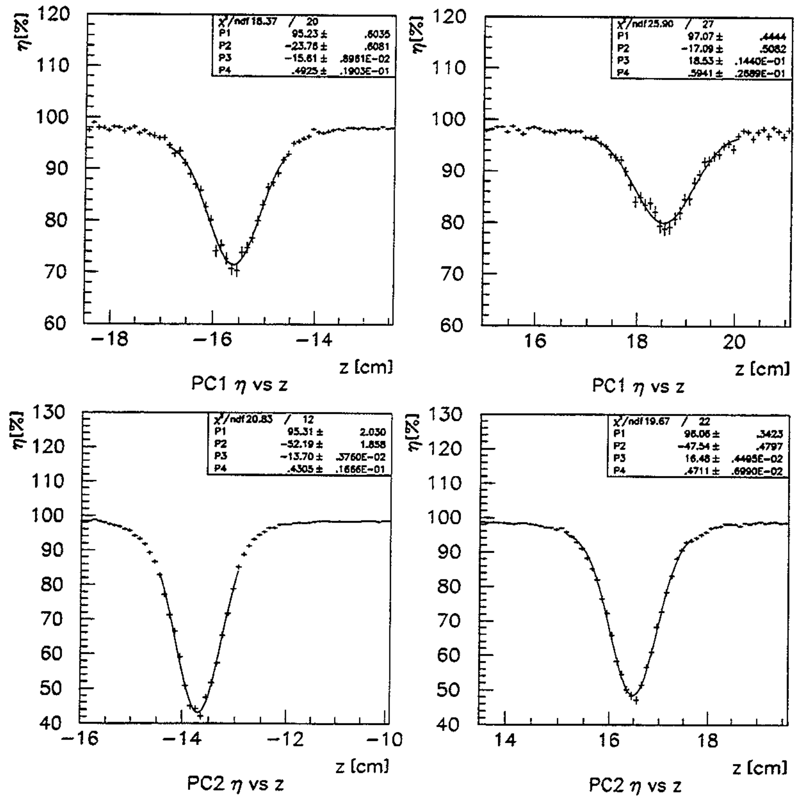

The spacer separations for each chamber are very consistent with each other (table 4.4) and compatible to better than 2 standard deviations with the construction values of (340 ± 1.0)mm and (300 ± 1.0)mm for PC1 and PC2 respectively. A possible increase in the separation values and a shift of the centre of the spacer positions due to the track inclination angle with respect to the z-axis ("z-dilation effect") was calculated to be negligible.

The spacer positions also lead to a mean z-shift (downstream) of the centre of the PCs with respect to the "official" (offline) centre of the detector. From an analysis of the four z-shift values (table 4.4) and assuming an M1/M2 compatibility, justified by the the small absolute differences, as compared to the size of the effect, a chamber dependent shift is found. The chamber shifts with respect to the official centre of the detector are:

$$\text{PC1:} \quad (+14.79 \pm 0.28)\,\text{mm}$$
$$\text{PC2:} \quad (+13.95 \pm 0.11)\,\text{mm}.$$

The quoted uncertainties have been pessimistically chosen to include both extreme values, as the deviation from the common mean for PC1 as well as for PC2 is 2.5σ. Nevertheless, the shift values are highly significant! This rather surprising result was checked by looking at the extremes of the z-distribution of track-hits in the other tracking devices i.e., DC4, DC5 and DC6 for the Drift Chambers (DC) and ST1 and ST2 for the Streamer Tubes (ST) by using only the inner chambers for the track selection, thus ensuring the ends of the active region could be seen. These tracking devices confirm a general downstream shift of the centre of the detector. Considering all values together however suggests a radial dependence of this shift, with the individual values being:

DC4: $(+11.0 \pm 2.1)$mm
DC5: $(+12.5 \pm 2.1)$mm
DC6: $(+10.5 \pm 2.1)$mm
ST1: $(+7.5 \pm 2.5)$mm
ST2: $(+10.0 \pm 2.5)$mm

Figure 4.6 shows two separate straight line fits to the seven shift values. Assuming a radial dependence gives a $\chi^2/\text{dof} = 0.88$ corresponding to a confidence level of 49.7%, whereas assuming no radial dependence gives a $\chi^2/\text{dof} = 3.79$ corresponding to a confidence level of 0.08%, thus confirming the significance of a radial dependence. Whether this is physical effect or an artifact of e.g. the track fitting would need further investigation.

Figure 4.6: z-shift of the sub-detectors as a function of their radii.

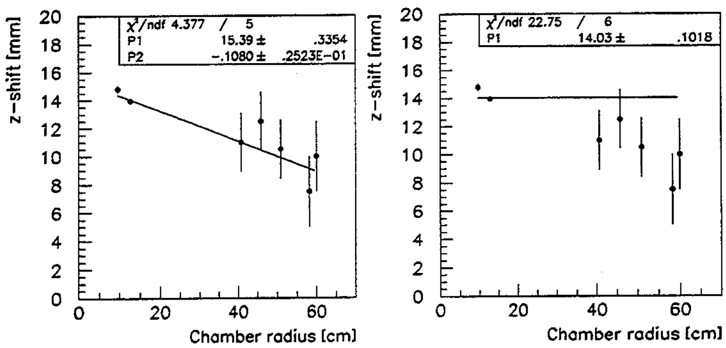

4.4.9 Active Length and Geometry of the PCs

By asking for all drift chambers to be present, the expected active lengths of the PCs using "minimum bias" data are constrained by the active length of the DC6 drift chamber. Taking into account the finite size of the selected region of tracks from within the target these maximum lengths are 519 mm for PC1 and 658 mm for PC2. From figure 4.4, one measures a non-zero efficiency in PC1 between (-257 ± 10)mm and $(+260 \pm 10)$mm. This gives a measured total active length of (517 ± 14)mm. For PC2 the corresponding value is (652 ± 14)mm. So, the different shape of the z-dependence for PC1 and PC2 is confirmed to be consistent with the difference in geometrical acceptance.

4.4.10 Loss of Efficiency Due to the Spacers

The efficiency loss due to the spacers can be evaluated by an integration of the fitted Gaussian to the spacer inefficiencies (fig. 4.5). The effect of the two spacers is (548 ± 19)[mm·%] in PC1 and (1125 ± 31) [mm·%] in PC2, where [mm·%] is the unit of integration of the efficiency over z. Normalising these values to the full active length of 700 mm in the PCs [41], one obtains the following efficiency losses due to the spacers:

$(0.78 \pm 0.03)\%$ loss in PC1
$(1.61 \pm 0.04)\%$ loss in PC2

These are consistent with the value of about 2% per chamber obtained in a test using a pion beam at normal incidence [41]. For inclined tracks (with respect to the spacers), as is the case in the CPLEAR detector, the inefficiency is expected to be reduced. This qualitatively also accounts for the difference between the values for PC1 and PC2, as each set of spacers were purposely placed so as to be misaligned for inclined tracks.

4.4.11 p_0-Dependence of the Efficiency

Figure 4.7 shows the momentum dependence of the efficiency and is characterised by three main features:

- a relatively flat momentum dependence above 350 MeV/c;
- a rise in the efficiency below 350 MeV/c;
- a fall in the efficiency at low and high momentum in PC1, while remaining rather constant in PC2.

Figure 4.7: Efficiency versus total momentum p_0.

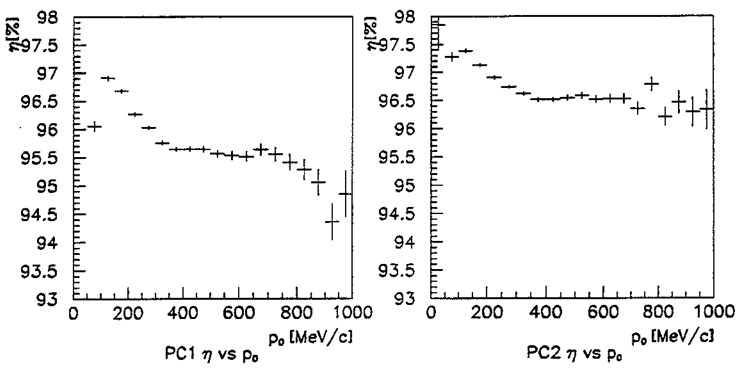

The first two features are consistent with that expected from the energy-loss of charged pions. Indeed, since "minimum bias" trigger data were selected, the dominant type of charged particles are pions. Their energy-loss calculated for the PC gas medium shows a relatively flat momentum dependence above 350 MeV/c and a rise below 350 MeV/c.

The third feature is related to the momentum resolution which is directly proportional to the track curvature resolution. The latter has various contributions arising from: the spatial resolution, track-length, number of sampling points and multiple scattering [8, §24.8]. The largest contribution to the momentum uncertainty comes from the track-length L and is proportional to $1/L^2$. Thus different track lengths, which can be caused by a difference in the number of hits, lead to a difference in the width of the measured momentum spectra. This difference in width leads directly to a momentum dependence of the 7-hit to 8-hit track ratio, which is essentially a measure of the efficiency of the chamber (cf. eq. (4.9)).

Thus for PC1 the track-length for 7-hit tracks is approximately given by the radius difference between DC6 and PC2 ($L_7^{\mathrm{PC1}} \simeq r_{\mathrm{DC6}} - r_{\mathrm{PC2}} = 382.5\,\mathrm{mm}$), which is smaller than that of 8-hit tracks, given by the radius difference between DC6 and PC1 ($L_8^{\mathrm{PC1}} \simeq r_{\mathrm{DC6}} - r_{\mathrm{PC1}} = 414.25\,\mathrm{mm}$). Hence the momentum uncertainty for 7-hit tracks in PC1 is approximately 17% larger than that for 8-hit tracks ($(L_8^{\mathrm{PC1}}/L_7^{\mathrm{PC1}})^2 = 1.17$). This ratio is unity for PC2 as there is no radius difference for the two cases.

It is this difference between the two chambers, together with the sensitivity to the 7-hit to 8-hit track ratio which causes the loss of efficiency at the ends of the PC1 spectrum compared with that of PC2.

4.4.12 cosα_T-dependence of the Efficiency

In the track selection, z and p_0 are left free. The efficiency of the chambers is plotted as a function of cos α_T (fig. 4.8). The observed behaviour has been qualitatively reproduced by a simulation taking into account the geometry of the chambers and the primary ion-pair production and collection in the gas mixture used. The overall behaviour of the efficiency versus cos α_T is governed by two partly compensating effects; as cos α_T increases, the path-length and therefore the primary ion statistics increases, while the survival probability due to capture decreases.

Figure 4.8: Efficiency versus cos α_T.

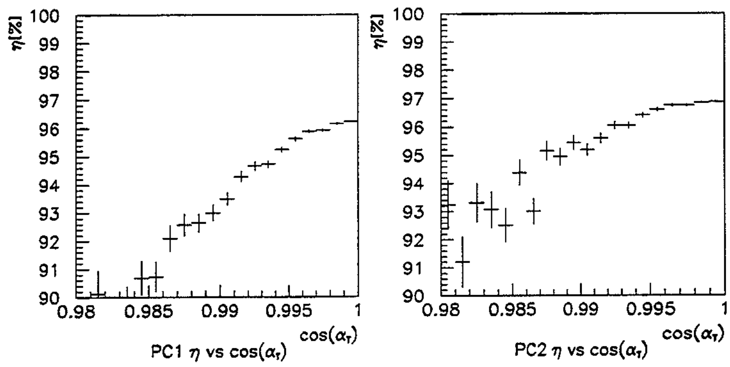

4.4.13 Cluster-Size versus cosα_T

The interest of this relationship is to show quantitatively the correlation between the cluster-size (CS) and α_T, where the cluster-size is defined as the number of adjacent hit wires per track crossing. The mean CS is found to be the same in PC1 and PC2:

$$\overline{\mathrm{CS}} = 1.12$$

The probabilities for different cluster-sizes is shown in table 4.5, from which one concludes that for both PC1 and PC2, the probability to have a CS greater than 1 is about 10%, while there is less than 1.5% probability of having a cluster-size larger than 2.

Table 4.5: Absolute cluster-size probabilities.

CS	$=1$	$=2$	≥ 3
PC1	90.01%	8.84%	1.15%
PC2	88.45%	10.37%	1.16%

4.4.14 Results from the Analysis of Simulated Data

The same analysis was applied to simulated data. Pions from 25 runs of semileptonic golden events (Trigger T23) were used, corresponding to about 130000 tracks. One finds a mean efficiency 0.5% and 1.5% lower than that of the real data for PC1 and PC2, respectively. The ϕ-, z- and p_0-dependences of the efficiency are also comparable. However, the spacer positions of ±150 mm and ±130 mm for PC1 and PC2 respectively, are 20 mm different compared to the construction values and significantly different to the real data values (cf. table 4.4). This difference makes the simulated separations wrong by 40 mm. The efficiency losses due to the spacers are respectively 1.9% and 2.2% for PC1 and PC2. This corresponds to the value of 2% per chamber quoted in reference [41] for non-inclined tracks. However in the real data (see Section 4.4.10) the selection of inclined tracks due to the spacer positions leads to smaller efficiency losses (0.8% for PC1 and 1.6% for PC2).

The $\cos\alpha_{\mathrm{T}}$-dependence as described by the simulation programme is qualitatively in agreement with that of the real data. The mean cluster-size of 1.16 found from simulated data originates from reference [41] and corresponds to a chamber high-voltage of 2700V. The value of 1.12 as found in the real data (see Section 4.4.13) is understandably somewhat smaller because a high-voltage of 2650V was standard for running periods P26 and later.

Finally the probability for a particle to give a signal in more than one wire is about 15% (10% in real data), while less than 1.0% (1.5% in real data) give a signal in more than two wires.

4.4.15 Summary and Conclusions

Using a simple and reliable method to determine the chamber efficiency, the dependence on various parameters was investigated and checked against the corresponding response from simulation data. The main points of this study may be summarised as follows:

- The mean running efficiencies of the chambers were found to be:

$$\begin{aligned} \eta_{\mathrm{PC1}} &= (95.97 \pm 0.21)\% \\ \eta_{\mathrm{PC2}} &= (96.73 \pm 0.21)\% \end{aligned}$$

  The simulation data essentially gave the above results except for a 0.5% and 1.5% lower efficiency for PC1 and PC2 respectively.

- The ϕ- and z-response from simulation data were found to be comparable to that of the detector data, apart from the simulated z-positions of the spacers. From a study of the tracking devices it was found that there was a significant downstream shift of the centre of these devices with respect to the "official" offline centre. For the PC1 and PC2, this shift corresponds to $(+14.79 \pm 0.28)$ mm and $(+13.95 \pm 0.11)$ mm, respectively.

- The difference in the M1 and M2 spacer positions, although being small, provides a sensitive test of magnetic field invariance. These differences were found to be significant at the level of $(2.0 - 2.9)\sigma$, indicating that the effect can only be due to one, or a combination of, the three presently known sources: the magnetic field knowledge, the pattern recognition logic or the track fitting procedure.

- The observed difference in momentum dependence of the efficiency between PC1 and PC2, for the detector data, can be understood by the difference in momentum resolution for 8-hit and 7-hit tracks in PC1. However the general form of the spectrum is governed by the energy-loss of charged pions in the chamber gas. The equivalent simulated spectra show a similar behaviour.

- Qualitative agreement was found between the detector and the simulation data results for the $\cos\alpha_{\mathrm{T}}$-dependence of the efficiency.

- The difference found in mean cluster-size between detector and Monte-Carlo data can be explained by a different assumption of the detector running conditions in the simulation.

- Finally, the probability for a particle to give a signal in more than one wire is about 10%, while less than 1.5% of events give a signal in more than 2 wires. The corresponding results from Monte-Carlo were found to be 15% and 1% respectively.

Thus, it has been shown that the operational characteristics of the proportional chambers are well understood and that apart from some minor descriptive errors in the Monte-Carlo, they are reasonably well reproduced.

Chapter 5

The CPLEAR Simulation Data

5.1 Why Use Simulation Data?

When an experiment involves many physical processes in a complicated detector geometry, such as CPLEAR, it is not possible to describe its behaviour analytically. But the individual physical (particles), geometrical (detector) and logical (trigger) properties of the system are known. This knowledge can then be used to simulate events with the same characteristics as the real events. This simulation is described in Section 5.2 for the specific case of CPLEAR, and the produced database is presented in Section 5.3.

The simulated events are first used to check the understanding of the experimental setup by comparing them with the real data.

Another interesting feature of the simulated data is their ability to describe the signal as well as the background events, and thus to determine the acceptance of the experiment for different kinds of events.

The simulated data may also be used to measure a real physical effect, which is not included in the generation of the simulated events, but which is of course present in real events. Thus any deviation from one sample to the other may signal either the use of a wrong parameter in the simulation programme, such as one of the detector characteristics, or a new, or a neglected physical process which was not included in the simulation programme. The analysis presented in Chapter 7 relies on this technique to measure the $\mathrm{K}^0_{\mathrm{e}3}$ form factor in the semileptonic decays. Therefore, it is necessary that the simulation reproduces correctly the real events, however some corrections might eventually be needed (Section 5.4). After the final data selection (cf. Chapter 6), the quality of the simulated data will be checked by comparison with the real data.

5.2 Principles of the Event Generation

The CPLEAR detector was simulated with the programme CPGEANT [45], which is the adapted version of the GEANT programme [46] to the geometry of the CPLEAR apparatus. The principle of the event generation was the following:

Generation: The $\mathrm{p\bar{p}}$-annihilation *Golden Channel* was selected and the particles momenta were generated according to the available phase space, using the routine GENBOD [47]. The intermediate resonances ($K^{\pm *}$, K^{0*}, ...) were also simulated.

Tracking: The particles then evolved in the detector material and the magnetic field. Multiple scattering, energy-loss and δ-ray emissions were taken into account according to the material distribution.

However, the regeneration of K^0_L into K^0_S in matter was not simulated and have to be corrected for separately (cf. Section 6.5).

Digitization: When a particle crossed a sensitive medium, its position, momentum and energy-loss were used to define the signal observed by the corresponding subdetector, according to its known performances. The random noise inherent to any detector was also generated and included in the event data.

The decay of the generated kaons, pions and muons was simulated with the corresponding lifetime. The neutral kaon decay channels were chosen according to their respective branching fractions, and the decay product kinematics was generated by GENBOD in the available phase space. It must be noted that the linear parameter of the K^0_{e3} and $K^0_{\mu 3}$ form factors was included in the simulation with the value $\lambda_+ = 0.03$. The following effects were not included:.

- The matrix element of the K^0-decays into three pions was neglected, and the decay products were generated uniformly in the phase space.
- No radiative decays were generated.

The event generation was finished when all particles had decayed or had reached the outside of the apparatus.

Trigger Simulation: The trigger decision was then simulated and if the event was accepted, it was transfered on tape. The generated history of each event was recorded together with the simulated detector response, because both of these informations are necessary to associate the observed behaviour to the generated characteristics of an event.

The next steps of the simulated data analysis are the same as for the real data. The two analysed samples are directly comparable. The selection criteria (Chapter 6) and the data structure are identical. The sole difference is that the generated (*true*) information is stored together with the simulated detector response.

5.3 The CPLEAR Simulation Event Sample

The CPLEAR simulation data includes *Golden Events* in which the neutral kaon decays into one of the following channels: $\pi^+\pi^-$, $\pi^+\pi^-\pi^0$, $\pi^0\pi^0$, $\pi^0\pi^0\pi^0$, $\pi e\nu$ and $\pi\mu\nu$. Independent data samples were generated for each decay channel. The characteristics of the simulation data used in this thesis are the following:

- The generated neutral kaons are restricted to lifetimes in the range $(0-30)\,\tau_S$, and the decay must occur within 45 cm radius, and ± 40 cm in the z coordinate. The K^0 ($\overline{K}^0$) decay rate was generated uniformly (FLAT) or exponentially (EXP). The latter case was only applied to the K^0_S decay channels, i.e. $\pi^+\pi^-$ and $\pi^0\pi^0$, since the K^0_L decay rate varies only by 5% in the above lifetime range.
- One sample of simulation events was generated according to the running conditions of period P25 (autumn 1993), with the spherical target. After the introduction of the cylindrical target and PC0, a new simulation was generated, based on the running conditions of period P28 (spring 1995).
- In order to reduce the data size, a minimal trigger was applied (T23≡ EDL), asking for one kaon candidate with $p_t > 270$ MeV/c plus one other track (cf. Section 3.9).

The number of generated events with these conditions for each decay channel is summarised in table 5.1.

Table 5.1: Number of events generated in each decay channel.

Period	Type	$\pi^+\pi^-$	$\pi^+\pi^-\pi^0$	$\pi e\nu$	$\pi\mu\nu$
P25	FLAT	301'442'800	60'000'000	130'000'000	60'000'000
P25	EXP	105'520'000	0	0	0
P28	FLAT	89'950'000	48'900'000	791'787'044	122'560'000
P28	EXP	380'000'000	0	0	0

5.4 Corrections to the CPLEAR Simulation Data

From the simulation data, the generated spectrum of different variables was compared with the corresponding spectrum from the real data. It was found that the simulation of the energy loss $\mathrm{d}E/\mathrm{d}x$ of the scintillators (S1 and S2), the number of photo-electrons $\mathrm{d}n/\mathrm{d}x$ from the Čerenkov counter (C) and the time-of-flight tof were not compatible with the real data. It was clear then that the simulation of the particle identification detector (PID, cf. Section 3.6) needed to be improved. Similarly, the simulated Dalitz distribution of the particles generated in the $\mathrm{p\bar{p}}$-annihilation was not compatible with the real data, and again the simulation had to be improved.

Two different methods were investigated to perform the correction (Section 5.4.1). Their advantages and disadvantages lead to the choice of the best method for each case. Then, the corrections and their results are described (Sections 5.4.2 and 5.4.3).

5.4.1 Method: Weights or Modification of the Event Characteristics

This section shows how the simulated data can be corrected. Two methods are discussed. Also shown is how the number of generated events is modified when the correction is applied to the measured distribution of the simulation data.

It is assumed here that the measured spectrum of a variable x in the simulation data $M_{mc}(x)$ is incompatible with the corresponding measured distribution in the real data $M_{rd}(x)$. The measured distribution $M_{mc}(x)$ from the simulation data is related to the generated distribution $G_{mc}(x)$ by

$$M_{mc}(x) = a(x) \cdot G_{mc}(x), \tag{5.1}$$

where $a(x)$ is the acceptance. Similarly, the measured distribution $M_{rd}(x)$ from the real data is related to the generated distribution $G_{rd}(x)$ of the real events by

$$M_{rd}(x) = a(x) \cdot G_{rd}(x), \tag{5.2}$$

where it is assumed that $a(x)$ is the same for real and simulation data, since their selection procedures are identical.

Corrections with weights: For the correction, one defines a weight

$$w(x) = \frac{M_{rd}(x)}{M_{mc}(x)}, \tag{5.3}$$

and multiply the number of simulated events localised at x by $w(x)$, such that the corrected distribution has the same shape as the real data[1]. This correction modifies the generated distribution $G_{mc}(x)$ into

$$G'_{mc}(x) = G_{mc}(x) \cdot w(x), \tag{5.4}$$

Then, the number of generated events $N_{mc} = \int G_{mc}(x)dx$ becomes

$$N'_{mc} = \int G'_{mc}(x)dx = \int G_{mc}(x) \cdot w(x)dx. \tag{5.5}$$

It is then necessary to know the function $G_{mc}(x)$ to determine the value of N'_{mc}, which will be used to normalise the simulated decay channels (cf. Section 7.2).

If $G_{mc}(x)$ is unknown, the corrected number of generated events N'_{mc} cannot be evaluated by eq (5.5). Nevertheless, using the approximation that the weight $w(x)$ is approximately constant over x,

$$w(x) \approx \overline{w}, \tag{5.6}$$

one can compute from eq (5.5)

$$\boxed{N'_{mc} \approx \overline{w} \int G_{mc}(x)dx = \overline{w} \cdot N_{mc}} \tag{5.7}$$

Correction by modification of the measured spectra: Difficulties arise if the approximation given by eq (5.6) does not hold. In this case, an alternative solution is to modify the distribution of x by moving an appropriate fraction of the simulated events from one value of x to another value x', such that the measured simulated event distribution $M'_{mc}(x)$ is equivalent to the real distribution $M_{rd}(x)$. By this method, the total number of measured simulated events is conserved,

$$\int M'_{mc}(x)dx = \int M_{mc}(x)dx. \tag{5.8}$$

The modified number of generated events N'_{mc} is

$$N'_{mc} = \int G'_{mc}(x)dx = \int \frac{M'_{mc}(x)}{a(x)}dx. \tag{5.9}$$

In eq. (5.9), the integral can be evaluated if one uses the approximation

$$\int \frac{M'_{mc}(x)}{a(x)}dx \approx \int \frac{M_{mc}(x)}{a(x)}dx, \tag{5.10}$$

which is justified by eq (5.8), if the acceptance $a(x)$ is approximately constant. Then, from eqs (5.9) and (5.10), one obtains that the number of generated events is not modified by the correction:

$$\boxed{N'_{mc} \approx \int \frac{M_{mc}(x)}{a(x)}dx = \int G_{mc}(x)dx = N_{mc}} \tag{5.11}$$

[1]See Section 6.5 for more explanations about the method of the weights.

Conclusion about the correction method: The validity of the approximations given by eqs (5.6) and/or (5.10) will determine which method should preferably be used. The choice will also depend on the necessity to avoid large weights. Furthermore, using weights, correlated variables will have to be corrected all by one single weight[2]. The statistics in each bin would then decrease, diminishing the quality of the correction. On the other hand, the modification of the detector response $x \to x'$ avoids this statistical limitation, but it does not ensure that the simulation of the trigger decision is the same after the correction. So, in any case, the correction cannot be perfect, and the best solution would have been to re-generate the simulation data, taking into account all the corrections.

The calibration data: In order to avoid biases, the corrections must be determined with data that are independent of the data used for the K^0_{e3} form factor analysis ($\pi e \nu$ data). These independent data are called *calibration data.* Two types of calibration data were used:

- The decay channel $K^0(\overline{K}^0) \to \pi^+\pi^-$ was used for the correction of the PID response to charged pions (Section 5.4.2) and for the calibration of the primary vertex kinematics (Section 5.4.3). The $\pi^+\pi^-$ events were selected by asking for

  1. one kaon candidate,
  2. a good event quality,
  3. the probability of the $K^0 \to \pi^+\pi^-$ constrained fit (9C) larger than 5%, and
  4. the lifetime t of the neutral kaon in the range $(0.5 - 4)\, \tau_S$.

  Since most of these cuts are similar to the semileptonic selection, they are described in more details in Section 6.4.2. It must be noted that no cut specific to $\pi e \nu$ data was applied (e.g. e/π-separation by neural network technique programme). In particular, no selection of the $\pi^+\pi^-$ events was done using the PID response, except for the primary kaon candidate.

- Photon conversion data (*Golden Events* containing a neutral pion decaying into two photons, followed by the process $\gamma \to e^+e^-$) were used for the calibration of the PID response to the electrons and positrons (Section 5.4.2). These events were selected by asking for

  1. one kaon candidate,
  2. a good event quality,
  3. the constrained fit probabilities for $\pi^+\pi^-$, $\pi^+\pi^-\pi^0$ and $\pi e \nu$ channels less than 10%, and
  4. the opening angle between the secondaries in the laboratory frame smaller than 0.1 radians.

  The condition on the opening angle was found to be the most efficient selection criteria to identify the $\gamma \to e^+e^-$ events.

5.4.2 PID Response

The charged tracks reaching the PID give a signal in each of its subdetectors: S1, C and S2 (cf. Section 3.6). The particles deposit energy in the first scintillator S1 (measuring the energy loss per unit length $d1dx \equiv \frac{dE}{dx}$, in units of [MeV/cm]), where the time-of-flight ($= tof$, in units of [ns]) is also measured. Then the particles cross the Čerenkov counter C (measuring the number of photo-electrons

[2]The preceding development can be applied for more than one variable. Then, the functions depend on x, y, z, ... , and every integral should be replaced by multiple integrals.

per unit length $dndx$, in units of [number of photo-electrons/cm]) and the second scintillator S2 (measuring the energy loss per unit length $d2dx \equiv \frac{dE}{dx}$, in units of [MeV/cm]). But the signal given by each subdetector depended on the energy deposited in the previous subdetectors. Their responses are thus correlated. From the real $\pi e \nu$ data, the measured spectra of the 4 variables for the electrons (fig. 5.1) and the pions (fig. 5.2) present evident discrepancies between real and simulation data. This can be

Figure 5.1: Uncorrected PID response to the **electrons**. The four rows correspond to the $d1dx$, $dndx$, $d2dx$ and tof. In each row, the real and simulation data distributions, as well as their ratio are presented. This ratio is expected to be constant if the variable is correctly described by the simulation. It should be noted that the number of events in the distributions is arbitrary.

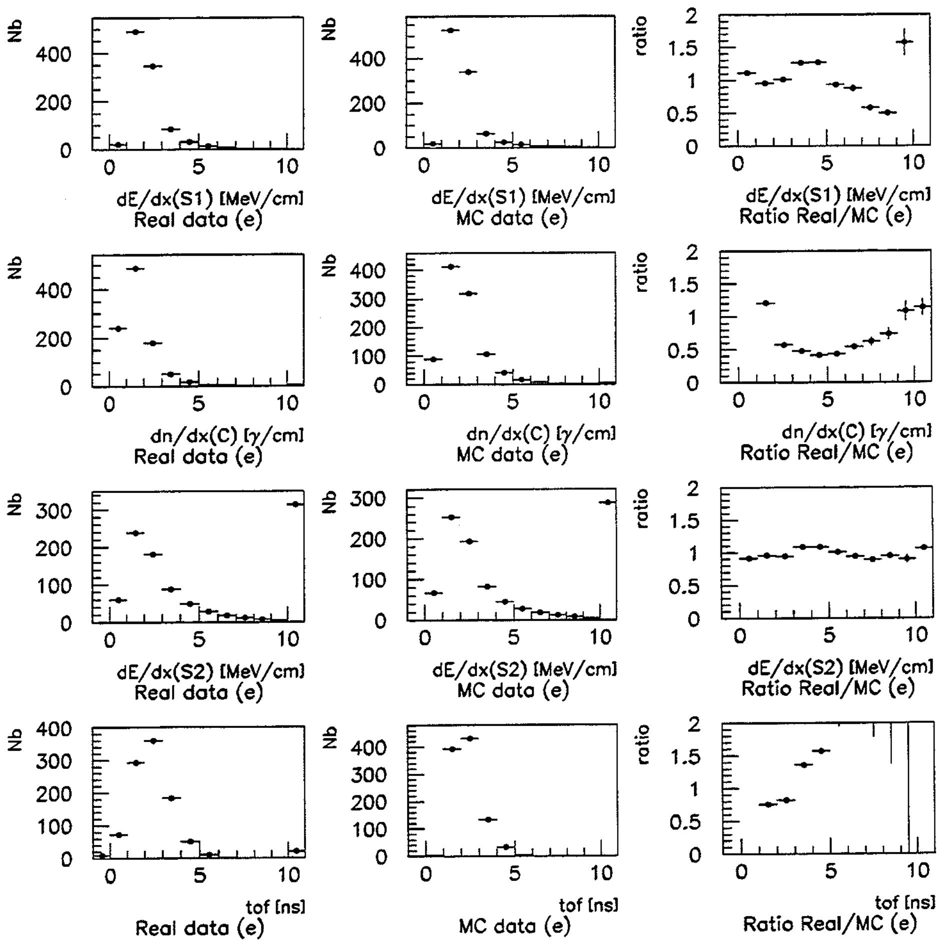

seen in the ratios between the real and the simulated distributions, which are expected to be constant, if the variables are correctly described by the simulation. It appears that the $dndx$ and the tof were badly described for both types of particles. The probabilities computed from the neural network using the PID informations for the e/π-separation (cf. Section 6.3.2) were also incompatible (fig. 5.3). Similar distributions were found from the calibration data. These discrepancies had to be corrected for, otherwise the cuts based on the e/π-separation programme would affect the momentum spectra and thus the q^2-distribution, needed for the measurement of the K^0_{e3} form factor.

The choice of the correction method depended on the following points, all discarding the method of

Figure 5.2: Uncorrected PID response to the **pions**. The four rows correspond to the $d1dx$, $dndx$, $d2dx$ and tof. In each row, the real and simulation data distributions, as well as their ratio are presented. This ratio is expected to be constant if the variable is correctly described by the simulation. It should be noted that the number of events in the distributions is arbitrary.

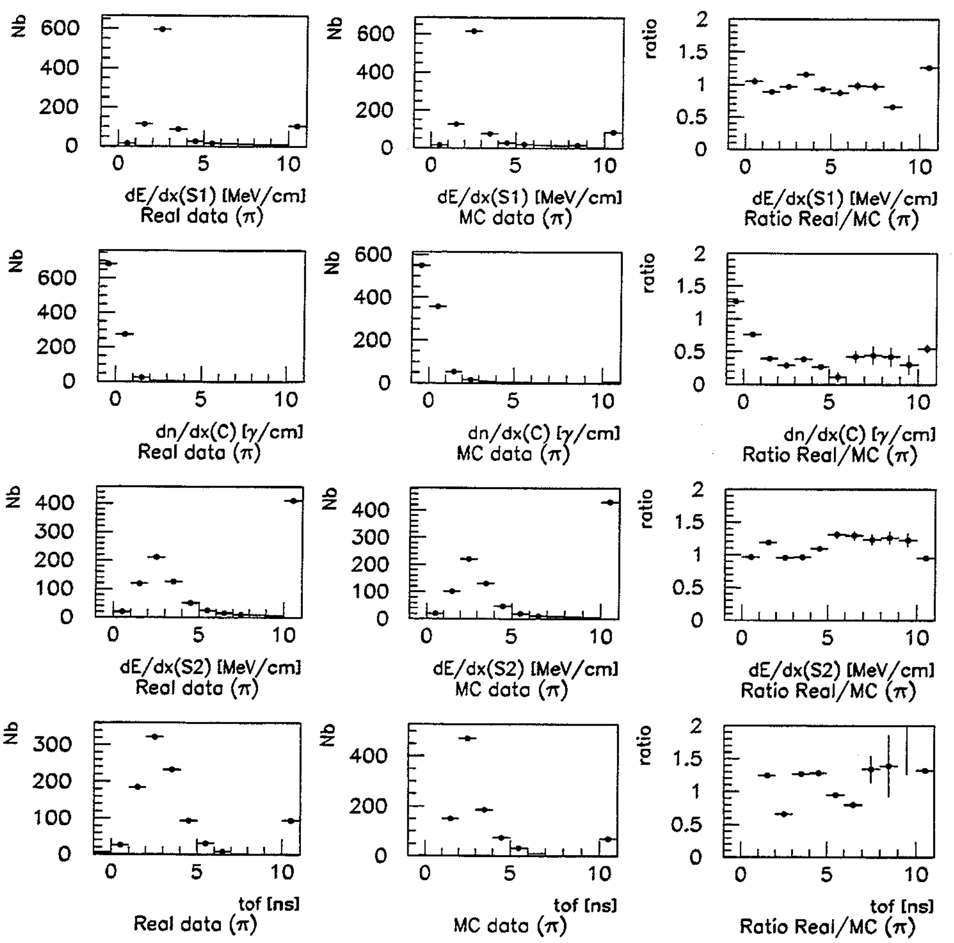

Figure 5.3: The e/π-separation programme output distributions from the uncorrected PID response for electrons and pions. In each row, the real and simulation data distribution, as well as the ratio are presented. This ratio is expected to be constant if the variable is correctly described by the simulation. It should be noted that the number of events in the distributions is arbitrary.

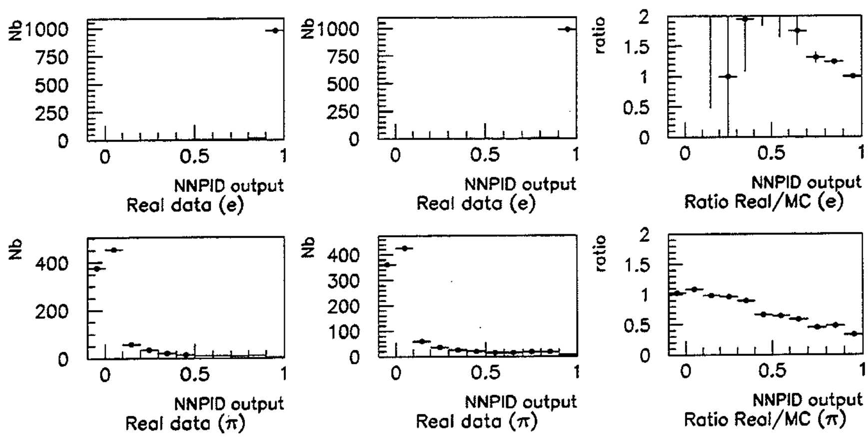

the weights:

- The 4 correlated variables had to be corrected simultaneously.
- From figures 5.1 and 5.2, one sees that the corrections were large (of the order of about ±40%).
- Both secondary particles of each event should have their PID response corrected. Since they had correlated momenta, each kinematical configuration of the secondaries should have its own weight, which could not be determined from the calibration data.

These reasons suggested the modification of the PID response rather than applying weights.

To this purpose, each variable ($d1dx$, $dndx$, $d2dx$ and tof) was divided into 12 bins in the range $[-1; 11[$ [3]. The first bin, $[-1; 0[$, was the inefficiency bin and the last one, $[10; 11[$, contained all values larger than 10. The real and the simulation calibration data provided the measured distributions in a 4-dimensional array of the PID response for each of the 4 particles e^+, e^-, π^+ and π^- and for 15 momentum bins of 50 MeV/c width in the range (50 – 800)MeV/c. The tracks used for the correction were secondary tracks selected such that they were unbiased by the trigger decision, by asking that the associated secondary track was seen by the trigger, i.e. had fired an S1 and was seen by the pattern recognition. Indeed, in the case of 3-track events (only 3 tracks seen by the trigger, but 4 tracks recognised by the offline analysis), the secondary track which was seen had in any case a signal in the first scintillator S1 and could not be used for the PID calibration.

Using the selected tracks, the correction for the scintillator S1 was computed for each momentum bin, from the projected real and simulated distributions on $d1dx$. The S1 correction was then applied to the complete array. Then, the Čerenkov response was projected on the 2-dimensional space defined by the momentum p and the $d1dx$, and the correction was computed as a function of these two variables. Again, the array was corrected. Similarly, the TOF correction was determined from the same p and

[3]The neural network (cf. Section 6.3.2) uses the 4 variables ($d1dx$, $dndx$, $d2dx$ and tof) in the range $[-1; 11[$ (in their respective units).

$d1dx$ space, independently of the Čerenkov and of the scintillator S2. Finally, the S2 was corrected as a function of p, $d1dx$ and $dndx$. This way, the correction took into account the correlations between the variables. The method was checked on the unbiased tracks selected from the calibration data. The corrected simulated distributions had the same shape as those of the real data. However, applying the correction to all the secondary tracks, differences appeared, due to the trigger simulation. Indeed, the modification of the $d1dx$ implied a modification of the trigger simulation:

- If $d1dx$ became negative while it was positive, the number of tracks seen by the trigger was decreased by 1 unit.
- If $d1dx$ became positive while it was negative, the number of tracks seen by the trigger was increased by 1 unit and the S1 module hit by the track had to be simulated having a hit.

This was the only modification which could be applied to the trigger simulation, without reprocessing all the simulation data from a very low level.

Finally, as the trigger depended mainly on the primary particles, it was not possible to modify the PID response of the primary pions without reprocessing the trigger simulation. Then, the correction was applied only to the secondary pions and electrons.

In the $\pi e\nu$ data, the corrected PID distributions (figs 5.4 and 5.5) are found to be compatible to within 20% of the real data distributions, except the tof, which deviates up to 40%. However, the e/π-separation programme output distribution of the selected electrons is correctly accumulated near 1 (fig. 5.6), although large differences ($\sim$ 80%) appear at lower values. However, this is not problematic, since only a negligible fraction of the electrons give an output smaller than 0.9. On the other hand, the pions e/π-separation distribution is only correct within 40% in the region where it can be misidentified with an electron (fig. 5.6).

To conclude this section on PID corrections, it is interesting to see its effect on the q^2-distribution. Figure 5.7 shows the ratio of the corrected and the uncorrected q^2-distributions. The first effect is the reduction by about 15% of the simulation data statistics. The second effect, more important for this analysis, is the fact that at low q^2 ($< 0.02\,\mathrm{GeV}^2$), and high q^2 ($> 0.10\,\mathrm{GeV}^2$), the distribution is strongly modified. These regions are then more sensitive to the quality of the simulation of the PID. The effect due to the remaining differences will be studied with the systematics (Section 7.3).

Figure 5.4: Corrected PID response to the **electrons**. The four rows correspond to the $d1dx$, $dndx$, $d2dx$ and tof. In each row, the real and simulation data distributions, as well as their ratio are presented. This ratio is expected to be constant if the variable is correctly described by the simulation. It should be noted that the number of events in the distributions is arbitrary.

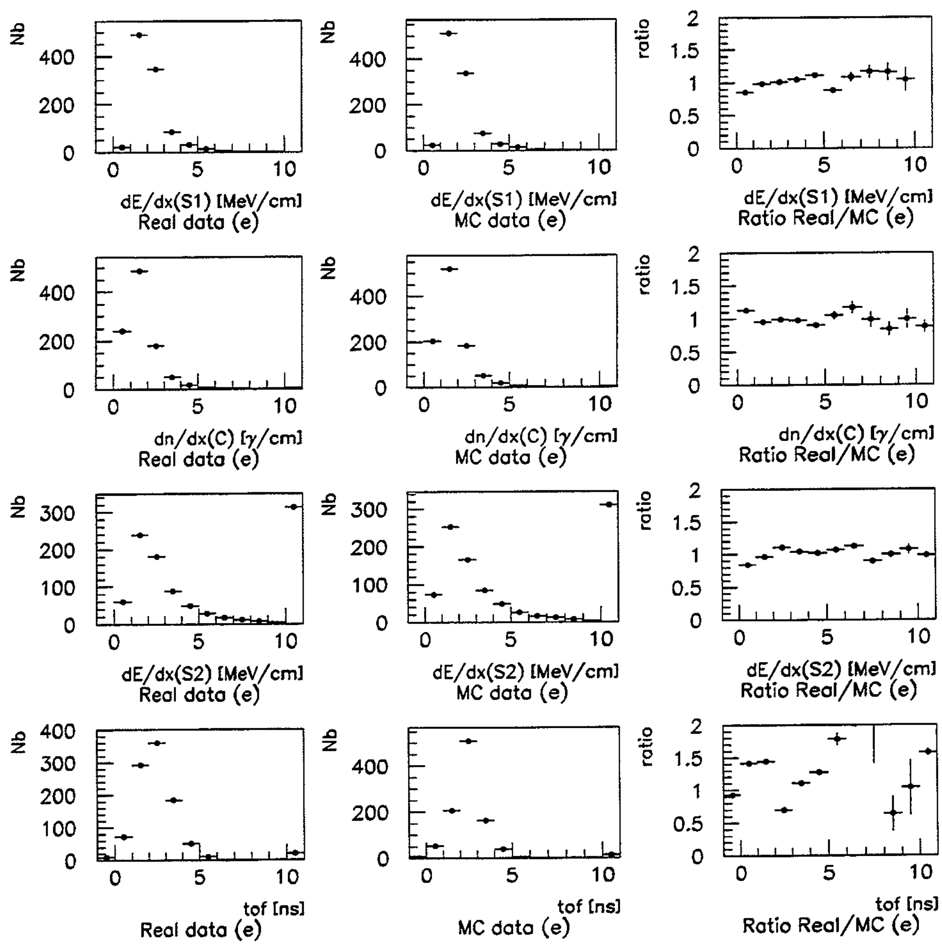

Figure 5.5: Corrected PID response to the **pions**. The four rows correspond to the $d1dx$, $dndx$, $d2dx$ and tof. In each row, the real and simulation data distributions, as well as their ratio are presented. This ratio is expected to be constant if the variable is correctly described by the simulation. It should be noted that the number of events in the distributions is arbitrary.

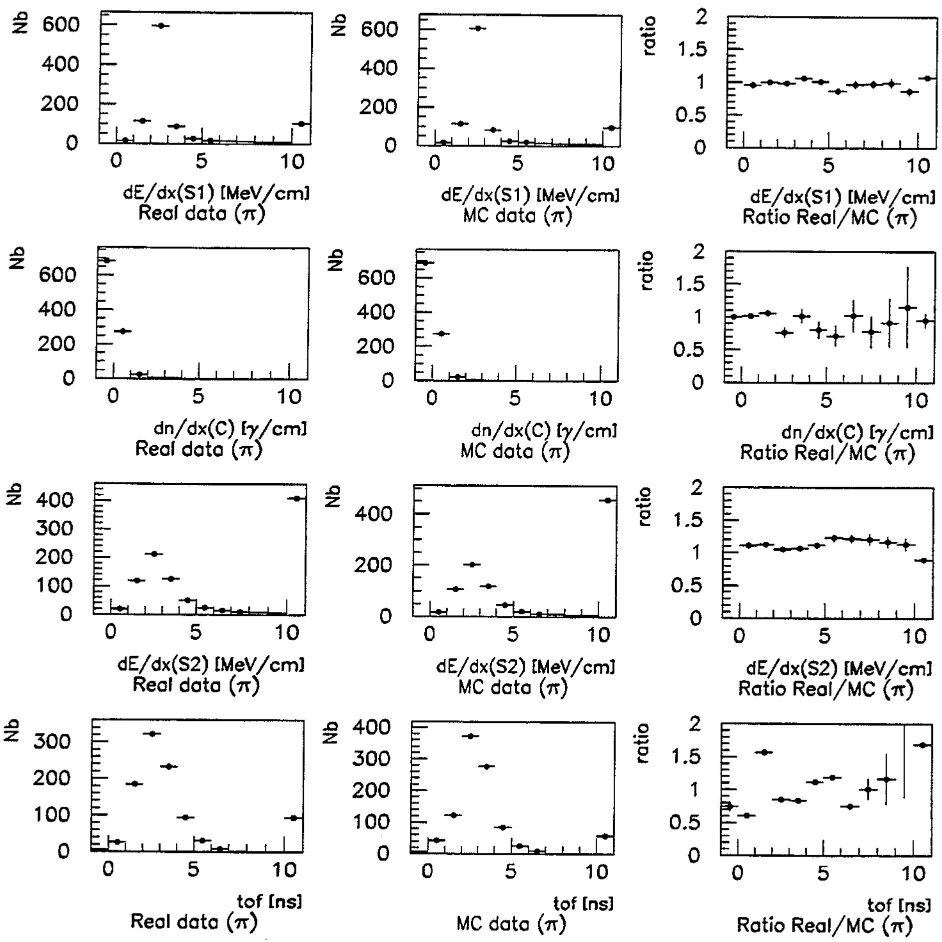

Figure 5.6: The e/π-separation programme output distributions from the corrected PID response for electrons and pions. In each row, the real and simulation data distribution, as well as their ratio are presented. This ratio is expected to be constant if the variable is correctly described by the simulation. It should be noted that the number of events in the distributions is arbitrary.

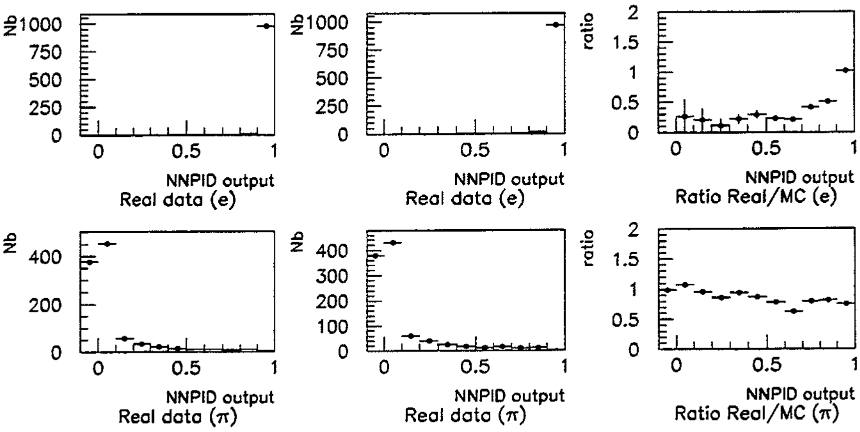

Figure 5.7: Ratio of the q^2-distributions of simulated $\pi e\nu$ events after and before the PID correction.

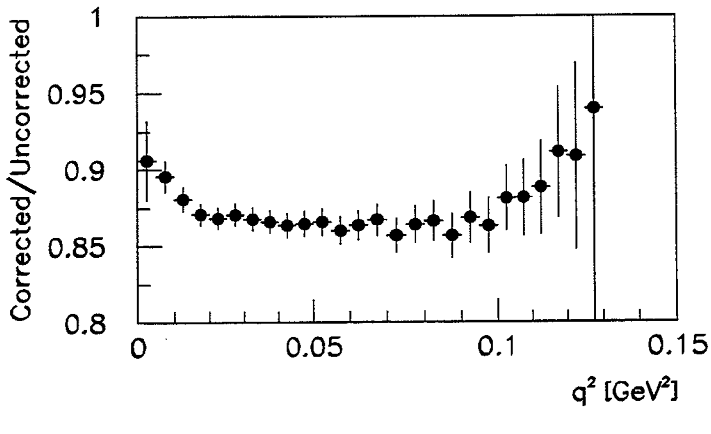

5.4.3 Primary Vertex Kinematics

The kinematics of the particles created in the p$\bar{\text{p}}$-annihilations (*Golden Channel*) is constrained by the available phase space. The amplitude of the reaction also depends on the intermediate resonances (K^{0*}, $K^{\pm *}$, a_0 and a_2 [41]). The measured distributions of two independent variables defining the phase space (the neutral kaon momentum p_{K^0} and the cosine of the angle between the 3-momentum vectors of the charged primaries, $\cos\alpha_{prim}$) show differences of about $\pm 40\%$ between real and simulation data (fig. 5.8). The observed discrepancies need to be corrected, since the momentum p_{K^0} is used as input in the calculation of the four-momentum transfer q^2.

Figure 5.8: Neutral kaon momentum p_{K^0} (first row) and cosine of the opening angle of the charged primaries $\cos\alpha_{prim}$, **before the corrections**. The plots present the real and simulation distributions, as well as their ratio. This ratio is expected to be constant if the variable is correctly described by the simulation. The structures seen in both variables are due to the intermediate resonances.

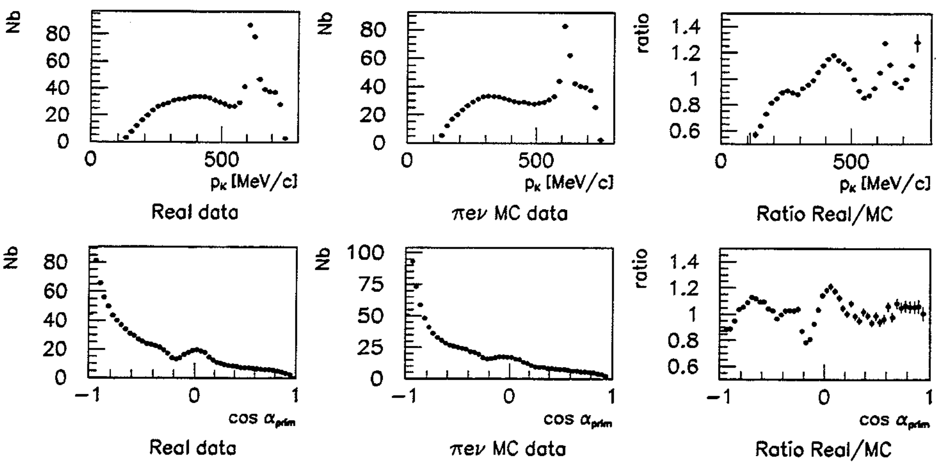

From the kinematics, the generated phase space distribution is well known, and the needed correction is not too large. Moreover, only one correction must be applied to each event, depending on two variables only. In this case, the application of a weight to each event is the most appropriate method to apply the correction.

Using the $\pi^+\pi^-$ calibration data, the weight was computed from the real and the simulated distributions of the phase space defined by the invariant mass of the neutral and charged kaon pair $m_{K^0K^\pm}$ and that of the neutral kaon and the pion pair $m_{K^0\pi^\pm}$. The phase space was divided into bins of 0.025 GeV^2 $*$ 0.025 GeV^2. Each distribution was normalised, such that the weights had values close to one.

For $\pi e \nu$ data, the corrected p_{K^0} and $\cos\alpha_{prim}$ simulated distributions (fig. 5.9) are compatible with the real data within $\pm 5\%$ over most of their respective range. However, at high values of $\cos\alpha_{prim}$, the correction introduces a difference of about 30% between real and simulation data, but this affects only few events.

Finally, the effect of this correction on the q^2-distribution (fig. 5.10) shows mainly an increase at low q^2. Again, this region is found to be very sensitive to the quality of the simulation. Thus, the effect of the remaining differences will be studied with the systematics (Section 7.3).

Figure 5.9: Neutral kaon momentum p_{K^0} (first row) and cosine of the opening angle of the charged primaries $\cos\alpha_{prim}$, **after the corrections.** The plots present the real and simulated distributions, as well as their ratio. This ratio is expected to be constant if the variable is correctly described by the simulation. The structures seen in both variables are due to the intermediate resonances.

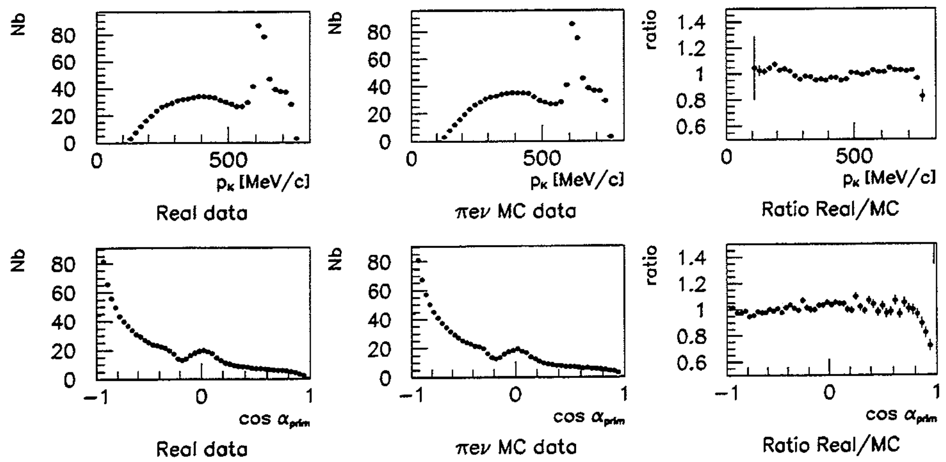

Figure 5.10: Ratio of the q^2-distributions of simulated $\pi e \nu$ events after and before the correction of the primary vertex kinematics.

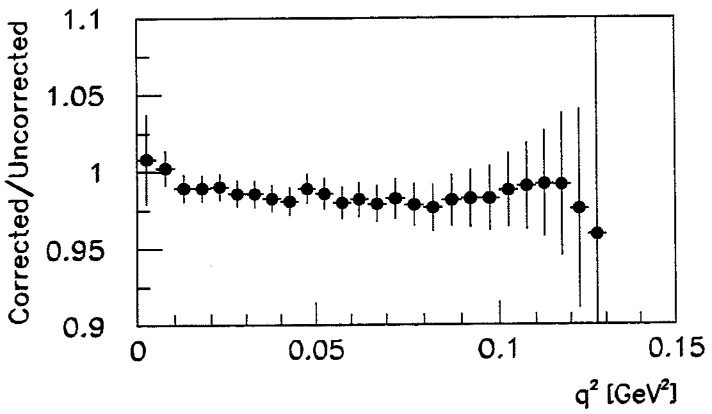

Chapter 6

The Data Selection

6.1 Introduction

In this Chapter are presented the different selection steps of the data analysis from the raw data, written on tape after the online trigger selection, up to the final sample on which the K^0_{e3} form factor analysis was performed. Section 6.2.1 describes the offline analysis which was applied on the raw data (*Production*), leading to the selection of events according to the K^0 decay channel type (*Filtering*). Some technical aspects of this procedure are emphasized in Section 6.2.2. The analysis tools used in the data selection (Kinematical *Constrained Fits*, and *neural network technique* for e/π-separation) are described in Section 6.3. The selection criteria specific to the semileptonic $\pi e \nu$ events are presented in Section 6.4, and the selected real and simulation data are compared, in order to check the quality of the simulation (Section 6.6). Finally, the acceptance (Section 6.7) and the background fractions (Section 6.8) are determined.

6.2 The Production and Filtering

6.2.1 Principle and Logic

The raw data written on tapes contained the informations given by the different subdetectors (wire-numbers, ADC and TDC informations for example). The goal of the *Production* was to translate these informations into physical values by means of geometrical and physical calibration constants. At this stage, the physical values were e.g. the space coordinates of track hit-points, the number of photo-electrons in the Čerenkov, or the energy-loss in each scintillator.

The *Pattern Recognition Logic* was then applied to the hit-point list of all the tracking subdetectors (PC, DC and ST). Its task was to group the hits track-by-track. Then, the *Track Fit* programme fits a spiral of axis parallel to z to every track. The momentum, the charge, a reference point in space and the χ^2 of the fit were determined.

The Track Fit results, as well as the PID and ECAL informations were then used for the offline *Golden Event* selection. A flag was attributed to every selected event according to its possible decay channel(s). Note that one event could be candidate for more than one channel.

In the next step, the *Filtering*, the data were split into decay channel candidates and were transfered to tapes. After this stage, each channel was analysed separately.

6.2.2 Technical and Computational Aspects of the Production

Technically, the computing performances were limited by the storage capacity, the data transfer capacity and the CPU power of the computer system:

- The large amount of data implied the use of a large number of magnetic tapes. Furthermore, the events were written on tape once after the *Production* and once after the *Filtering*. As an example, the CPLEAR experiment collected a total of a few billion events. During a typical data taking period, P28 ($\approx$ 40 days, spring 1995), about 8000 IBM3480 tapes of 200 Mb capacity were written. Each tape contained 10^5 events of raw data ($\approx$ 2 Kb/event). At the production, $60 - 70\%$ of the events were rejected. The raw informations together with the Track Fit and the other pre-analysis results were written on tape (MINRAW format). These additional informations increased the size of each event to $\approx$ 6 Kb, so that for each input tape, one output file of $180 - 200$ Mb was produced. After the *Production*, the total amount of data was doubled, and even more than tripled after the *Filtering*. Depending on the type of magnetic support, Exabytes of 5 Gb, DLT2000 of 10 Gb or IBM3590 of 10 Gb capacity, 20 to 50 files were written on each tape.

- All the data on tapes had to be read and copied on a disk directly accessible by the processing units (*Stagein* procedure). The analysed events were also written on the disk before being copied on tapes (*Stageout* procedure).

- The large number of events and the complexity of the analysis programme needed an enormous CPU-time. The mean CPU-time necessary to produce $\approx$ 200 Mb of data was about 40 minutes with the MOTOROLA RS6000 processor. The CPU-time needed for the production of one period like P28 was then $\approx 2 \cdot 10^7$ s (or $>$ 200 days for one processor).

Because of these constraints, the operational scheme of the production was chosen to optimise the *Production* rate. The *Production* programme, used in 1995 to produce the P28 data, controlled the *Stagein* and the *Stageout*, and submitted the analysis programme to the available processing units for all the input files. It worked within a loop proceeding periodically ($\approx$ every minute) through a sequence of five steps:

1. Selection of the next tape in the list of all the tapes to be analysed as well as the associated output tapes for the produced data. Once a tape was selected for the analysis, it was removed from the list.

2. Start the *Stagein* procedure for the first input tapes not yet analysed. The number of these tapes depended on the available space on the disk. Occasionally, no new tape could be *staged in* until the analysis of a previous tape was finished. Disk space was also reserved for each output file (200 Mb). All these commands were submitted in background to allow the main programme to continue running.

3. Submit the analysis programme for the tapes which have been completely copied on the disk.

4. Look for the data whose analysis was finished and send the *Stageout* command for the output file.

5. The analysed input files and the already *staged out* output files were cleared from the disk, in order to prepare free space for the next tapes.

This procedure allowed an optimal use of the computing capacities: the disk space was at all time used maximally, as well as the available processors. Quantitatively, the computational limitations were the following:

- The maximum transfer capacity achieved from the tapes to the disk, and vice versa, was up to $\approx$ 9 Mb/s for the IBM3590 tapes.
- The number of tape reading/writing units was limited.
- The storage space on disk was limited. In autumn 1995, it was less than 40 Gb, however it increased the year after.
- The processing power was also limited and shared with other CERN experiments. Typically 10 to 15 jobs were running in parallel, one for each input tape.

With these technical constraints, a maximum of about 150 tapes could be analysed every day. Unfortunately, problems occurring randomly reduced this rate by a factor of two. These were mainly tape reading errors, but also tape drive hardware problems, communication interrupted between devices due to an overload, or no disk space available. Actually, the 5100 tapes analysed at CERN for the P28 data taking period were *produced* and *filtered* within about $2\frac{1}{2}$ months at a mean rate of 70 tapes/day.

6.3 The Analysis Tools for the Data Selection

6.3.1 Constrained Fits

A *Constrained Fit* searches for the kinematical and geometrical configuration which is most compatible with the measured event, and satisfying one or more constraints, e.g. the conservation laws [48].

In the CPLEAR experiment, the parameters used to characterise an event are the momentum (vector) at a reference point for each track, the x and y coordinates of the intersection in the transverse plane (vertex) for every pair of tracks and their z-separation at the vertex. The mass and vertex assignments to the tracks, and the momentum and energy conservation laws lead to an over-constrained system of equations. The number of constraints (1C, 2C ...) corresponds to the difference between the number of available equations and the number of unknowns. Practically, the constrained fit is performed by minimising the χ^2 function

$$\chi^2 = \sum_{i=1}^{N}\sum_{j=1}^{N}(x_i^{meas} - x_i^{fit})V_{ij}^{-1}(x_j^{meas} - x_j^{fit}),$$

under a set of M constraints defined by the M equations

$$c_k(x^{fit}) = 0, \qquad\qquad k = 1, \dots , M$$

where the c_k are functions defining the constraints. The x_i's are the parameters used to describe the event and V is their error matrix. The x^{meas} and V are provided for each track by the Track Fit results. The minimisation is performed by using the Lagrange multiplicators method. The results are the fitted x_i^{fit} and the value of the minimised χ^2 from which the probability of the fit is computed. This probability will be used as a selection criterium, as it is a measure of the level of compatibility between the event kinematics with the hypotheses given by the constraints. The constrained fits used in the semileptonic analysis are the following:

1C-Fit This fit is used to select the *Golden Events*. It applies the hypothesis that the primary track candidates are a $K^{\pm}$ and a $\pi^{\mp}$, and that there is an unseen K^0. The four-momentum conservation at the primary vertex gives four constraints, three of which are used to determine the momentum of the K^0. There is therefore one constraint left for the fit (1C-Fit).

2C-Fit Under the $K^0 \rightarrow \pi e \nu$ hypothesis, this fit imposes the four-momentum conservation at both primary and secondary vertices. There are then 8 equations. The K^0- and ν-momenta give 6 unknowns, therefore the fit is a 2C-Fit.

6C-Fit Under the $K^0 \rightarrow \pi e \nu$ hypothesis, this fit imposes the four-momentum conservation at both vertices (8 equations), the alignment of the K^0-momentum with the vector relating the primary vertex to the secondary vertex in the transverse plane (1 equation) as well as in the longitudinal plane (1 equation), and the crossing in the longitudinal plane of the primary and secondary tracks at their respective vertex (2 equations). These 12 equations and the 6 unknowns (K^0- and ν- momenta) lead to a 6C-Fit.

$\overline{4\mathrm{C}}$-Fit Under the $K^0 \rightarrow \pi^+\pi^-$ hypothesis, the four-momentum conservation is required at the secondary vertex (4 equations). The K^0-momentum determined from the 1C-Fit is used so that there are no unknowns. Therefore the fit is a 4C-Fit. It is used to reject $\pi^+\pi^-$ events which are characterised by a good probability of this fit ($\overline{4\mathrm{C}}$-Fit).

$\overline{2\mathrm{C}}$-Fit Under the $K^0 \rightarrow \pi^+\pi^-\pi^0$ hypothesis, this fit is analogous to the 2C-Fit($\pi e \nu$). Similarly to the $\overline{4\mathrm{C}}$-Fit, it is used to reject $\pi^+\pi^-\pi^0$ events ($\overline{2\mathrm{C}}$-Fit).

6.3.2 Neural Network Technique for e/π-Separation

In the semileptonic analysis, an electron identification method is needed to complete the constrained fit results. Since most of the events contain pions, it is necessary to distinguish electrons from pions. In addition to their different momentum spectra, their different interaction characteristics in matter are used:

- For a given momentum, their velocities and therefore their time-of-flight (tof) are different.
- Their different velocities produce a different amount of Čerenkov light.
- At the momenta under consideration ($<$ 400 MeV/c), the electrons are all minimum ionising particles, while most of the pions deposit more energy due to ionisation.

All these differences can be exploited by using the PID informations, together with the measured momentum of the particle. Thus, 6 parameters are determined for each track (cf. fig. 6.1):

1. The momentum, computed by the Track Fit [1].
2. The $\mathrm{d}E/\mathrm{d}x$ in the S1 scintillator.
3. The number of photo-electrons $\mathrm{d}n/\mathrm{d}x$ in the Čerenkov counter.
4. The $\mathrm{d}E/\mathrm{d}x$ in the S2 scintillator.
5. The difference between the measured tof of the particle and the expected one *if it was a pion.*
6. The difference between the measured tof of the particle and the expected one *if it was an electron.*

This 6-dimensional information is best analysed using the neural network technique [49]. It has the advantage to perform an analogical treatment of the informations in the multi-dimensional space and gives optimum results. The present neural network, called NNPID [49], was trained with pions

[1] The *Constrained Fit* momenta cannot be used, because they are biased by the particle hypotheses applied to the event.

Figure 6.1: PID response for the dE/dx in S1, the dn/dx in the Čerenkov (number of photo-electrons per cm, npe/cm) and the differences of the measured tof, and the expected tof under $e^{\pm}$ or $\pi^{\pm}$ hypotheses, as a function of momentum p.

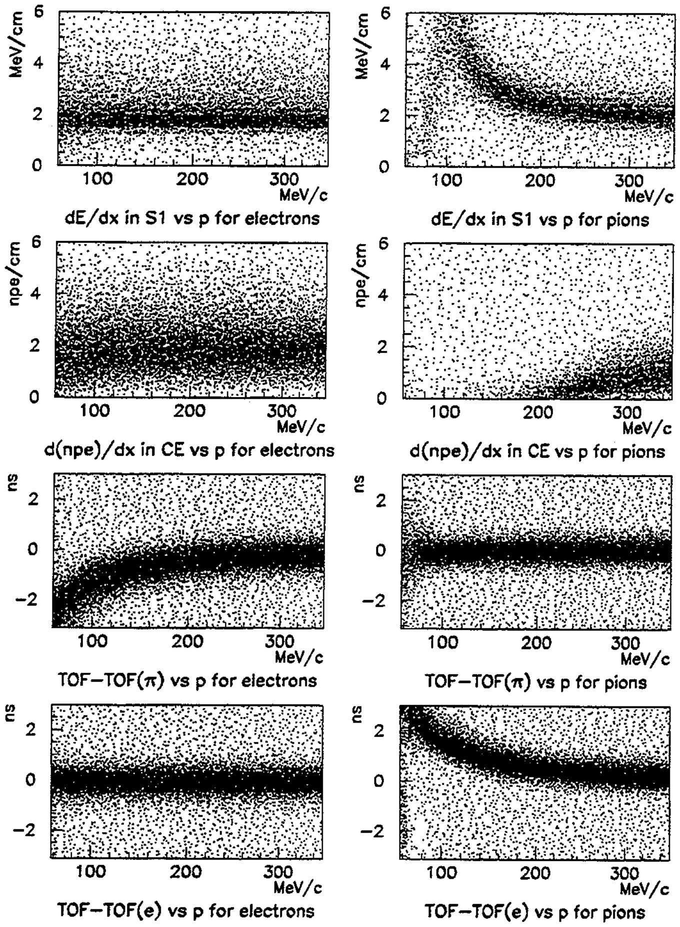

recognised without ambiguities from minimum bias data ("trigger T1") and with electrons from photon conversion data. These electrons have momenta in the range (50 – 350)MeV/c, defining the NNPID working conditions. The best performances were obtained with one hidden layer composed of 6 "neurons". The output of the network is a number between 0 and 1. The training was done such that the NNPID gives the value 0 if the particle was a pion, and 1 if it was an electron (cf. fig. 6.2).

Figure 6.2: NNPID output for pions and electrons. All the values lie in the range $(0-1)$. The pion distribution is situated close to zero, while the electrons are situated close to one. The e/π-separation is based on this difference.

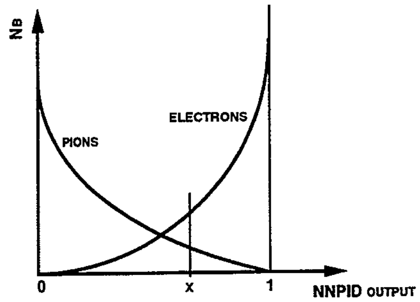

The efficiency of the neural network depends on its ability to distinguish electrons from pions. To characterise it, a kind of probability of recognition is defined. The NNPID output distributions for pions and electrons between 0 and 1 overlap in each momentum bin. For a given value x of the NNPID output, one defines the probability for the particle to be an electron (pion) as the fraction of the electron (pion) distribution laying below (above) the value x. In the following analysis, an electron is defined as a particle of momentum in the range (50 – 350) MeV/c with a defined probability to be an electron, i.e. larger than zero and for which the probability to be a pion P_π is less than 2%. With that definition, the NNPID electron recognition efficiency, with 2% pion background, is larger than 95% for 140 MeV/c electrons (fig. 6.3, b), where the momentum spectrum is maximum in $K^0 \to \pi e \nu$ events (fig. 6.3, a).

Figure 6.3: Electron spectrum in K^0 semileptonic decays (a) and the NNPID electron recognition efficiency (b) defined with 2% pion background.

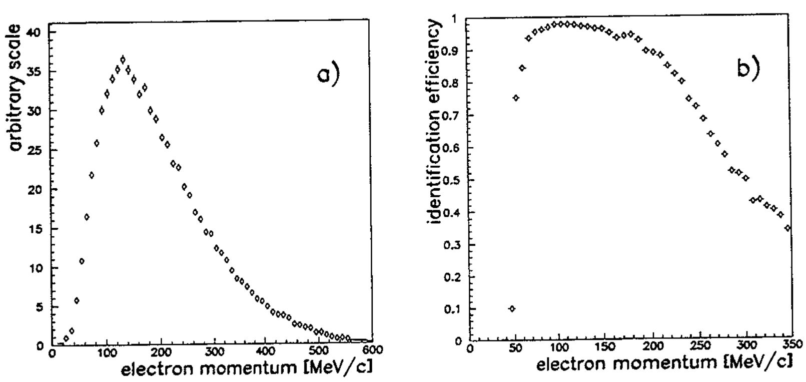

The calorimeter (ECAL) [39] was also used for the e/π-separation. The method relies on the different shower topologies produced by the electrons and the pions in the calorimeter. Indeed, the electrons produce an electromagnetic shower, while most of the pions pass through. This method is described in ref. [50]. It applies to electron momenta in the range (200 – 550) MeV/c and it can thus be used as a complementary selection criterium to the NNPID. Its efficiency is about 60 – 70% with 6% pion contamination. However, this tool will not be used in the present analysis, because it could introduce a bias due to the unknown quality of the simulation programme for the calorimeter.

6.4 The Semileptonic Data Selection

6.4.1 Introduction

In this section, the data selection criteria specific to the K^0_{e3} form factor analysis are presented. The cuts were optimised to reduce the background fraction and to select to most comparable samples between real and simulation data. Only data from the periods P28-P29 (1995) using the proportional chamber PC0 were used for the present analysis. A typical semileptonic event is presented on figure 6.4.

Figure 6.4: Semileptonic event selected in the real data. One sees the primary tracks on the right. Their vertex is situated inside the target, at the centre of the detector. The kaon candidate was not detected by the Čerenkov counter. The secondary vertex is found to be outside the proportional chambers. Of course, no hit is visible on the neutral kaon path, relating both vertices.

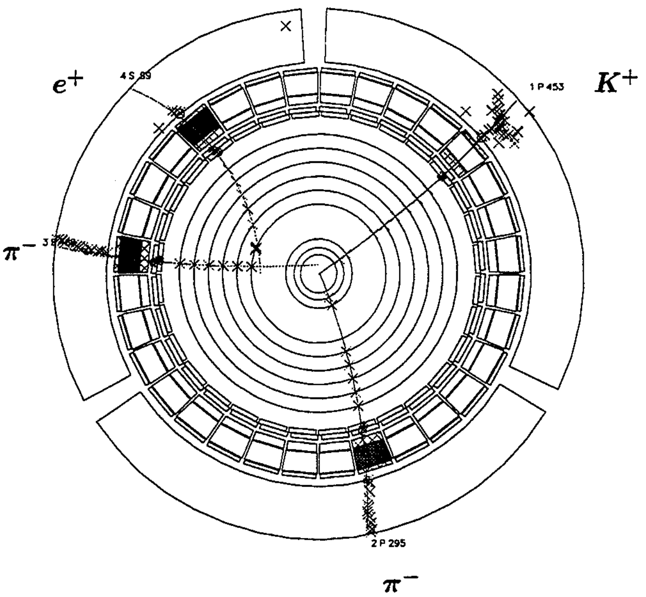

6.4.2 Selection Criteria

The semileptonic events must be efficiently separated from the other decay channels, mainly from $K^0 \rightarrow \pi^+ \pi^-$. Indeed, $\pi^+\pi^-$ events represent the main fraction of the charged decay channels written on tapes. The semileptonic $\pi\mu\nu$ events represent the other important background, mainly due to its similarities with the $\pi e\nu$ events. A special cut based on the missing mass at the secondary vertex was developed to reject these $\pi\mu\nu$ background events. Then, in order to select the semileptonic $\pi e\nu$ events, the following criteria were applied:

1. **Kaon candidate selection.** There must be at least one kaon candidate, which has an S1·$\overline{\text{C}}$·S2 signature in an efficient PID sector. Its p_t must be larger than 300 MeV/c and its total momentum p larger than 350 MeV/c. Its $\mathrm{d}E/\mathrm{d}x$ and $\mathrm{d}n/\mathrm{d}x$ must lie within 3 standard deviations from the expected values.

2. **Event quality cuts.** The event must contain 4 charged tracks. All the tracks must pass through different S1 sectors. Two or more tracks are primaries, i.e. containing at least one PC-hit. Each primary (secondary) track must have at least 5 (4) hits in the tracking chambers and each track at least 2 hits in the longitudinal plane. The reduced χ^2 of the Track Fit is required to be smaller than 5, and the primary vertex must lie within the target wall ($r_{prim} < 1$ cm and $|z_{prim}| < 3$ cm). Furthermore, the distance of closest approach of the 2 primary candidates to the vertex must be less than 10 cm. The probability for the 4 tracks to originate from the same vertex must be less than 5%. The primary and secondary vertices are well defined, separated by more than 1 cm in the transverse plane, and are associated to tracks of opposite charge. The secondary vertex must be outside PC0 ($r_{sec} > 1.7$ cm) and the two primaries must be seen by PC0. The secondary vertex satisfies $r_{sec} < 36$ cm, $|z_{sec}| < 40$ cm, with the lifetime t less than $30\,\tau_S$. The innermost tracking hit of the secondaries must be at a larger radius than that of the secondary vertex, in order to remove bad track associations.

3. **Logical cuts.** Among 16 possible particle-track associations[2], one and only one configuration satisfies the entire set of cuts. The event passes the offline simulation of the trigger and the chosen primary K-π pair is the one recognised by the trigger (*matching*).

4. **Kinematical cuts.** The primary and secondary pions must have a momentum larger than 80 MeV/c and lower than 1000 MeV/c, which is more than the maximum momentum allowed for particles produced in p$\overline{\text{p}}$-annihilations at rest. The secondary electron must have a momentum larger than 60 MeV/c and less than 350 MeV/c. To remove backscattered tracks from the external part of the detector as well as events whose primaries are too close to each other, the opening angle α_{prim} of the primaries must be such that $|\cos\alpha_{prim}| < 0.98$. To remove photon conversion e^+e^--pairs, the opening angle α_{sec} of the secondaries in the laboratory frame must be such that $\cos\alpha_{sec} < 0.90$. The probability of the 1C-Fit must be larger than 10%, and that of the 2C- and 6C-Fits larger than 5%. To remove $\pi^+\pi^-$ and $\pi^+\pi^-\pi^0$ events, the probability of the $\overline{\text{4C}}$- and $\overline{\text{2C}}$-Fit are required to be less than 10% and 5% respectively.

5. **K/π and e/π-separations.** There must be one and only one particle recognised as a charged kaon. Similarly, one and only one particle is identified as an electron. An electron is defined as a particle whose probability to be a pion is less than 2% (but larger than 0% in order to be defined). This probability is computed by the NNPID for the momentum range (50 – 350) MeV/c. Any particle outside this momentum range is not an electron candidate (cf. Section 6.3.2).

6. **Special cuts.**

   - As a complement to the NNPID decision, and in order to select more carefully the electrons, a new cut based on the *dndx* can be defined. Indeed, the *dndx* of the electrons is most of

[2] The charged kaon can be one of the 4 tracks. Then the primary pion can be only one of the 2 remaining tracks of opposite charge. This leaves 2 possibilities for the secondary electron. The total number of possible configurations is then $4\cdot 2\cdot 2 = 16$.

the time positive, while that of pions is smaller than 1 (cf. figs 5.4 and 5.5). This is expected since the electrons are always faster than $\beta = 0.81$, the minimum velocity for a particle to give light in the Čerenkov, while pions are not. This suggests the cut for the selection of the electrons:

$$dndx(\mathrm{e}^{\pm}) > 0.$$

This is an efficient way to eliminate pions from the electron sample.

- The electrons must be seen by the trigger, i.e. the trigger did recognise a track associated to this electron. This cut is justified for two reasons:
  (a) If an electron is not seen, the trigger simulation relies entirely on the simulated PID response of the pions, which is known to be poorer than that of electrons.
  (b) If the event is kept, the electron was recognised by the NNPID, which requires an S1. This means that the electron has in any case an S1 signature. Then, if it is not seen by the trigger, one can suspect some effects, which might not be well simulated, e.g. not enough hits in the tracking chambers or two tracks too close together.
- $\pi^+\pi^-$ events are efficiently rejected by a cut on the opening angle of the secondaries in the neutral kaon rest frame $\alpha_{\pi e}$, under the hypothesis of the semileptonic $\pi e\nu$ decay (fig. 6.5):

$$\cos\alpha_{\pi e} > -0.9.$$

Figure 6.5: Cosine of the opening angle between the secondary tracks, in the K^0 rest frame, from simulated $\pi e\nu$ and $\pi^+\pi^-$ data. These distributions were obtained by selecting events with all the criteria (1 to 5), except the "special cuts". The $\pi^+\pi^-$ events are mainly situated at low values of $\cos\alpha_{\pi e}$ and can thus be efficiently rejected be asking for a $\cos\alpha_{\pi e}$ larger than -0.9.

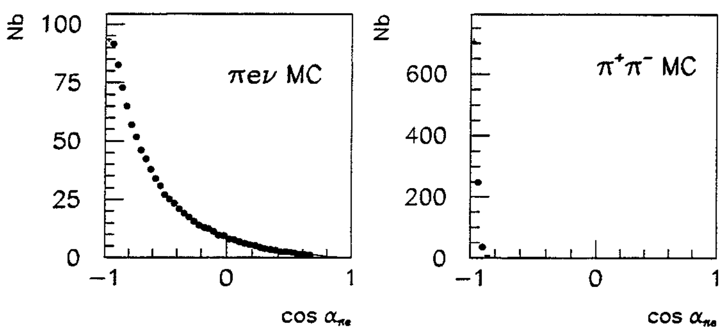

- Semileptonic $\pi\mu\nu$ events have a behaviour very similar to that of $\pi e\nu$ events, mainly due to the lepton universality. Since the NNPID was not tuned for e/μ-separation, because of the lack of a clean muon sample, the kinematical variables are the only variables used to distinguish the two types of events. Indeed, a certain fraction of $\pi\mu\nu$ events was already rejected by the constrained fits. Still, there remains a fraction close to 15%. Hence, a new cut based on the missing mass at the secondary vertex was developed. Since the missing particle is a neutrino, the missing mass should be zero. But a mass m_ℓ must be attributed to the charged lepton. If $m_\ell = m_e$ ($m_\ell = m_\mu$), the missing mass is expected to be zero in the $\pi e \nu$ ($\pi \mu \nu$) sample, while it should be different from zero in the other one. The missing mass $M(m_\ell)$ (function of the lepton mass hypothesis) depends on the measured momentum of the neutral kaon and of the two secondaries, as well as on the event type hypothesis:

$$M^2(m_\ell) = E^2(m_\ell) - p^2,$$

where $E(m_\ell)$ is the missing energy,

$$E(m_\ell) = \sqrt{p_{\mathrm{K}^0}^2 + m_{\mathrm{K}^0}^2} - \sqrt{p_\pi^2 + m_\pi^2} - \sqrt{p_\ell^2 + m_\ell^2},$$

and p is the missing momentum,

$$p^2 = (\vec{p_{\mathrm{K}^0}} - \vec{p_\pi} - \vec{p_l})^2.$$

The simulation of this missing mass $M(m_l)$ for the semileptonic events, taking into account the resolution on the momentum measurement suggest the cut

$$M^2(m_l) < 0.$$

However, the improvement of the signal/noise ratio is different for both lepton mass hypotheses, suggesting that one could attribute to m_l a value between m_e and m_μ in order to find an optimum of the ratio and of the rejection factor. It was found that $m_l = 0.75 m_\mu$ is a good choice removing a large part of muonic events without removing too many $\pi e \nu$ events. Thus, the following cut was applied:

$$M^2(0.75 m_\mu) < 0.$$

6.5 Further Corrections to the Real and Simulation Data

In order to have the simulation data comparable to the real data, all known physical effects must be included in the simulation. The corrections for the PID response (Section 5.4.2) and for the primary vertex kinematics (Section 5.4.3) previously described were applied to correct effects not well simulated. In this section, further correction for neglected effects are described.

If an effect was neglected at the event generation (cf. Section 5.2), it can be included later by attributing to every event a weight w. Then, one single generated event is counted "w-times", without changing its statistical significance:

> Each single event follows a Poisson distribution ($1 \pm \sqrt{1}$). Multiplying it with a constant w, one get $w \cdot (1 \pm \sqrt{1}) = (w \pm w)$ events, what is statistically identical. Then, N independent events with weights w_i become $N' = \sum w_i \pm \sqrt{\sum w_i^2}$, which is different from $\sum w_i \pm \sqrt{\sum w_i}$.

However, if more than one effect must be corrected, attention must be payed to their correlations. Let's define each correction of type "i" by the weight $w_i = 1 + \epsilon_i$. Then, the global weight W applied to an event is:

$$W = \prod_i w_i = \prod_i (1 + \epsilon_i) \simeq 1 + \sum_i \epsilon_i + \sum_i \sum_j \epsilon_i \epsilon_j + \ldots \tag{6.1}$$

It appears that if two weights are correlated, then eq (6.1) is not true anymore. The correlation must be taken into account in the third term, unless the weights are very close to 1 (i.e. $\epsilon_i \ll 1$). Then,

$$W = 1 + \sum_i \epsilon_i \tag{6.2}$$

would be a good approximation. Hence, the problems due to the correlations can be avoided if all the weights have values close to 1.

As was seen in Section 5.2, some effects were not included in the simulation. These are reviewed now, plus two weights specific to the real data. Figure 6.6 shows the effects of each weight on the q^2-distributions.

Figure 6.6: Effect of the weights w_{decay}, $w_{\Delta RC}$ and w_λ on the simulated semileptonic $\pi e \nu$ q^2-distribution, of $w_{3\pi slope}$ on the simulated $\pi^+\pi^-\pi^0$ events, and of w_{reg} and α on the real data. For a description of the weights, see the text.

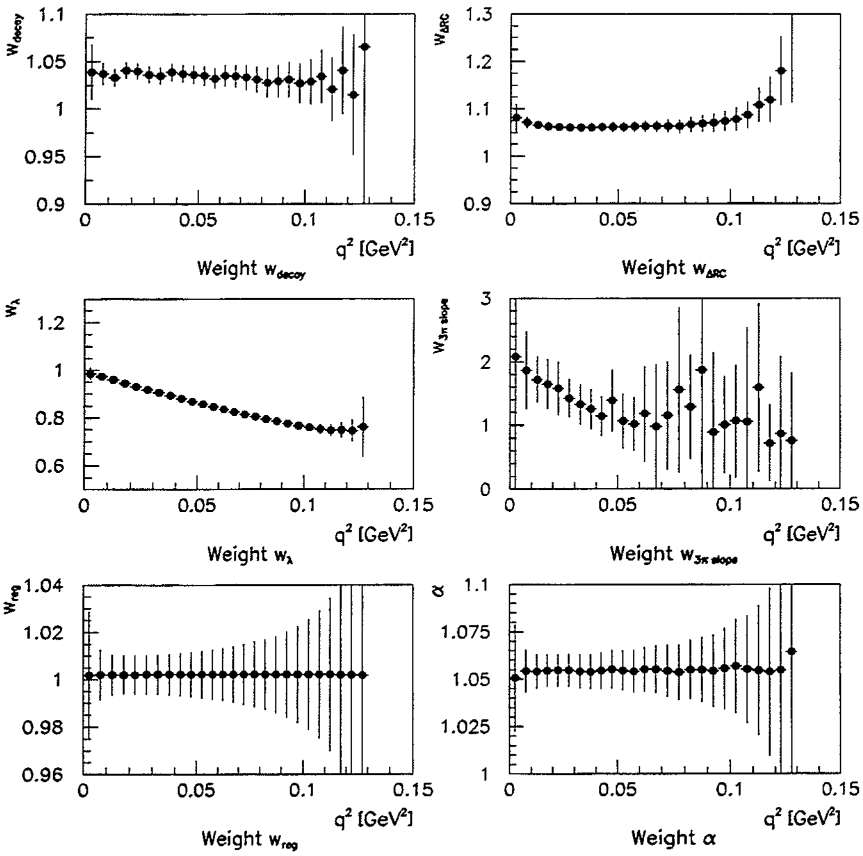

Decay Rate: The simulated $\pi e \nu$, $\pi \mu \nu$ and $\pi^+\pi^-\pi^0$ events were generated flat in lifetime (Section 5.2). The exponential decay rate of the neutral kaon was introduced in these simulated channels by applying the following weight, according to the decay rate expressions eq. (2.17) (w_i or equivalently w_{decay} in fig. 6.6):

$$w_i = a_i e^{-t/\tau_S} + b_i e^{-t/\tau_L} + c_i e^{-(1/\tau_S + 1/\tau_L)t/2} \cdot \cos(\Delta m \cdot t - \alpha_i), \tag{6.3}$$

where i stands for each of the channels. This weight includes CP-violation effects and the coefficients a_i, b_i, c_i and α_i depend on the decay channel. Figure 6.6 shows that the q^2-distribution is not very sensitive to this correction.

Radiative corrections to the $\mathbf{K^0_{e3}}$ decays: Radiative corrections to the $\pi e \nu$ decay channel were computed according to the calculations of Ginsberg [51]. These corrections include the contribution of virtual and real photons. They were applied with the weight $w_{\Delta RC}$. Its effect on the rates is shown on figure 6.7. The q^2-distribution is modified by introducing a small slope in the medium region. However, at low and high values, the correction is larger (fig. 6.6).

Figure 6.7: Radiative corrections $\Delta_{RC}(E_\pi, E_e)$ in [%] in the Dalitz plot E_π versus E_e.

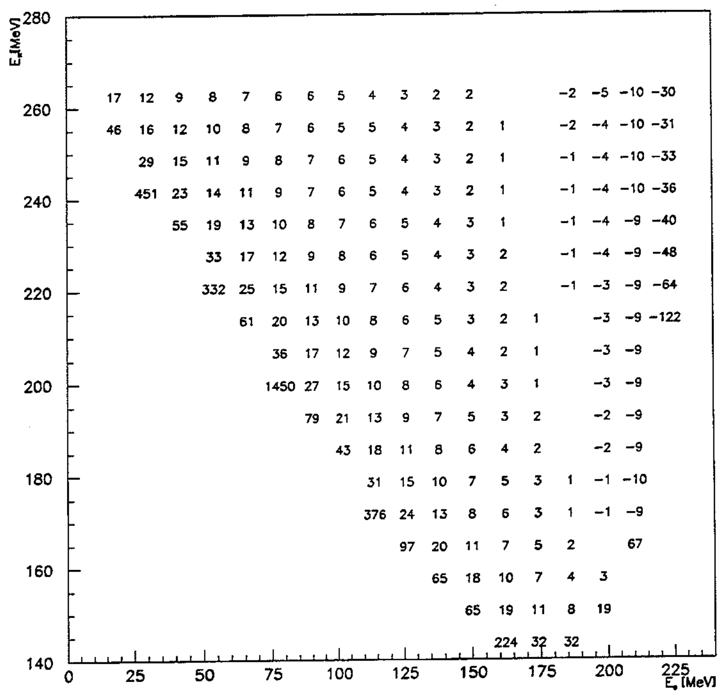

Form Factor: The semileptonic $\pi e \nu$ events were generated according to a linear q^2-dependence of the K^0_{e3} form factor using the value $\lambda_+ = 0.03$. As a constant form factor ($\lambda_+ = 0$) is needed for this analysis, a weight w_λ, defined as

$$w_\lambda = \frac{1}{(1 + \lambda_+ \frac{q^2}{m_\pi^2})^2}, \tag{6.4}$$

was applied to counteract the effect introduced by the form factor dependence on q^2, eq. (2.47).

Slope Parameters in 3π decays: The Dalitz plot distribution for the $K^0 \to \pi^+\pi^-\pi^0$ decays, parametrised by the variables X and Y (cf. ref. [8] or ref. [52]), depends on the coefficients g, h, j and k

defined in ref. [8]. The weight $w_{3\pi slope}$, defined as

$$w_{3\pi slope} = 1 + gY + hY^2 + jX + kX^2, \tag{6.5}$$

using the values $g = 0.670$, $h = 0.079$, $j = 0.0011$ and $k = 0.0098$ [8], was then applied to the $\pi^+\pi^-\pi^0$ events. The effect on the q^2-distribution (cf. fig. 6.6) is not negligible, justifying thus the correction. However, it is not necessary to check the quality of this correction, because the $\pi^+\pi^-\pi^0$ decay channel is very much reduced by the selection criteria (cf. Section 6.8 concerning the background levels).

Regeneration: The regeneration of K^0_L into K^0_S in the detector material was neglected in the simulation. This effect was studied in an independent analysis [53] and a weight w_{reg} was deduced for each real event in order to eliminate it. As it can be seen on figure 6.6, this correction has a negligible effect on the q^2-distribution.

Normalisation α at primary vertex: The detector efficiency was different for detecting K^+ and K^-, due to their different interaction probability with the detector material. This effect was corrected separately in the real and simulation data, using each data sample to determine the weight α which should be applied. However, this correction, like the regeneration correction, has a negligible effect on the q^2-distributions.

6.6 Quality Check of the Simulation Data

6.6.1 Method

The quality of the simulation data was checked by comparing the spectra of the relevant variables with those of real data. For that purpose, the semileptonic $\pi e \nu$ simulated events were corrected using the K_{e3} form factor's linear energy dependence parameter $\lambda_+ = 0.03$, according to the value given in ref. [8]. Three types of variables were checked:

1. Geometrical: the radius and the z coordinates of the primary and secondary vertices, and the neutral kaon lifetime t.

2. Kinematical: the momenta, the opening angles at both vertices, and the constrained fits probabilities.

3. Physical: the light generated in the scintillators and the Čerenkov counters, and the measured time-of-flight for each particle (cf. Section 5.4.2).

These characteristic variables were checked by plotting their distributions measured from real and simulation data, as well as their ratio. For each variable, the consequences of remaining discrepancies were analysed. Three types of conclusions can be drawn:

1. The differences, if any, do not have a direct influence on the form factor measurement. Therefore, possible remaining effects will be included in the systematic errors.

2. The differences are localised in a relatively small region, such that they can be removed by applying a cut on the data. In most cases, differences of this type are due to a specific background, thus justifying the cut.

3. The differences are important and the Monte-Carlo description needs to be corrected for.

However, since the corrections to the simulation described previously (cf. Sections 5.4 and 6.5) were applied, large discrepancies are not expected and the first conclusion applies.

6.6.2 PID Response: Energy Loss, Čerenkov Light and Time-of-Flight

For these variables, one refer to Section 5.4.2.

6.6.3 Primary Vertex Position: r_{prim} and z_{prim}

The position of the p$\bar{\text{p}}$-annihilation vertex depends on the beam and the target geometries, as well as on the hydrogen pressure. Fluctuations in time are expected but they are not included in the simulation, because of a lack of predictability. These facts might explain the differences in the shape of the distributions of the vertex position between real and simulation data (fig. 6.8). However, in the region of large statistics the discrepancy is small. In addition, the position of the primary vertex is uncorrelated with the four-momentum transfer q^2, used in the form factor analysis. Hence, it is not necessary to correct for the observed differences.

Figure 6.8: Distribution of the primary vertex position (r vs z) from real data (firt plot), simulation data (second plot). The third plot show the ratio of the real over simulation distributions. The ratio lies in the range (0-2.5), with the dark region for large ratio.

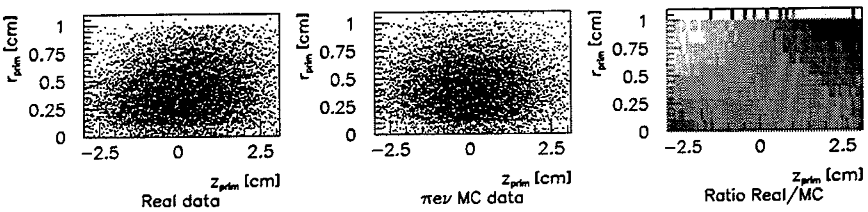

6.6.4 Primary Vertex Kinematics: p_{K^0} and $\cos\alpha_{prim}$

For these variables, one refer to Section 5.4.3.

6.6.5 K^0-Lifetime

The next interesting variable is the reconstructed neutral kaon lifetime t. The agreement between real and simulation data is particularly good (fig. 6.9) and no correction is necessary.

Figure 6.9: Distribution of the K^0 lifetime.

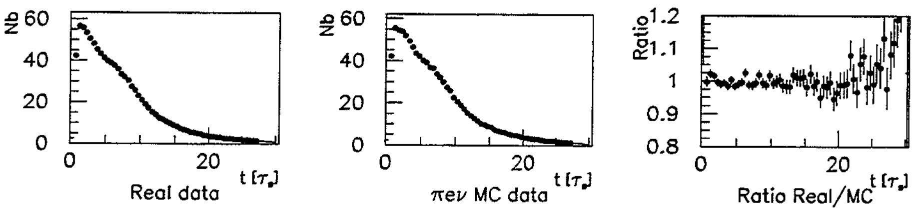

6.6.6 Secondary Vertex Position: r_{sec} and z_{sec}

The distributions of the secondary vertex radius r_{sec} and z_{sec} depend on the momentum distribution of the K^0 (previously corrected), its lifetime and on its direction in space. The observed distributions (fig. 6.10) are qualitatively correctly described by the simulation. In particular, the excess of events at the wire-plane of the different chambers is due to neutral kaons decaying close to the chamber and creating two tracks giving hits in neighbouring wires. For these events, the detector electronics applied the clustering [3], such that the same position at the wire-plane was assigned to both tracks. Thus, the vertex was forced to lay on the wire-plane. However, the ratio of the two distributions shows some structure with variations within $\pm 10\%$. Similarly, the z_{sec} distributions differ within the same proportion. These variations will be discussed with the systematics (Section 7.3).

Figure 6.10: r_{sec} and z_{sec} distributions of the secondary vertex.

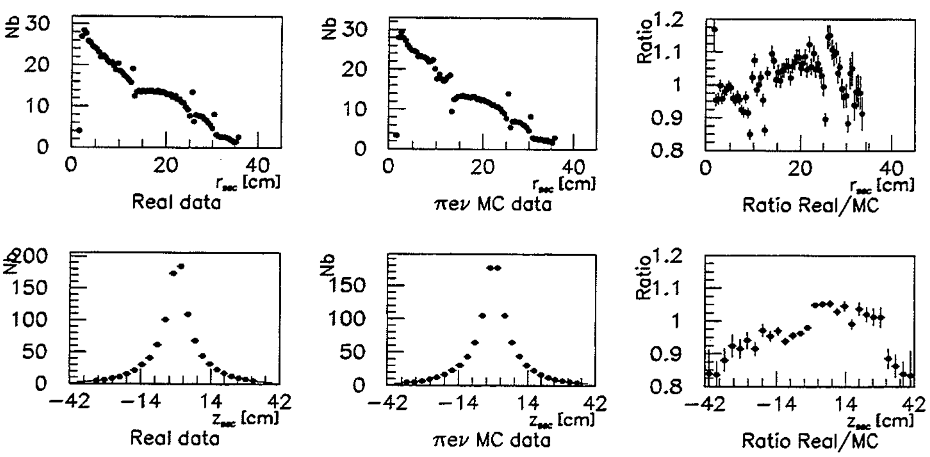

[3]Association of two or more adjacent hits, based on the hypothesis that one single track can fire more than one wire.

6.6.7 Kinematic Variables of the Secondary Vertex

The distributions related to the secondary vertex kinematics depend on the K^0_{e3} form factor. Since this is the parameter to be measured, one cannot modify these distributions. Moreover, *the phase space was generated flat and this is the reference to which the real data is compared. Then any difference between the real data and the simulated phase space has either an independent source (K^0 momentum, PID response, trigger simulation), or it is due to the effect one want to measure.* Nevertheless, it is necessary to check that these variables are correctly described. Figure 6.11 shows the distributions for p_e, p_π, $\cos\alpha_{\pi e}$, $\cos\alpha_{sec}(lab)$ and $\cos\alpha_{K\pi}$. All these variables are relatively well described, i.e. remaining differences lie within ±5%.

Figure 6.11: Secondary vertex kinematics variables: p_e, p_π, $\cos\alpha_{\pi e}$, $\cos\alpha_{sec}(lab)$ and $\cos\alpha_{K\pi}$.

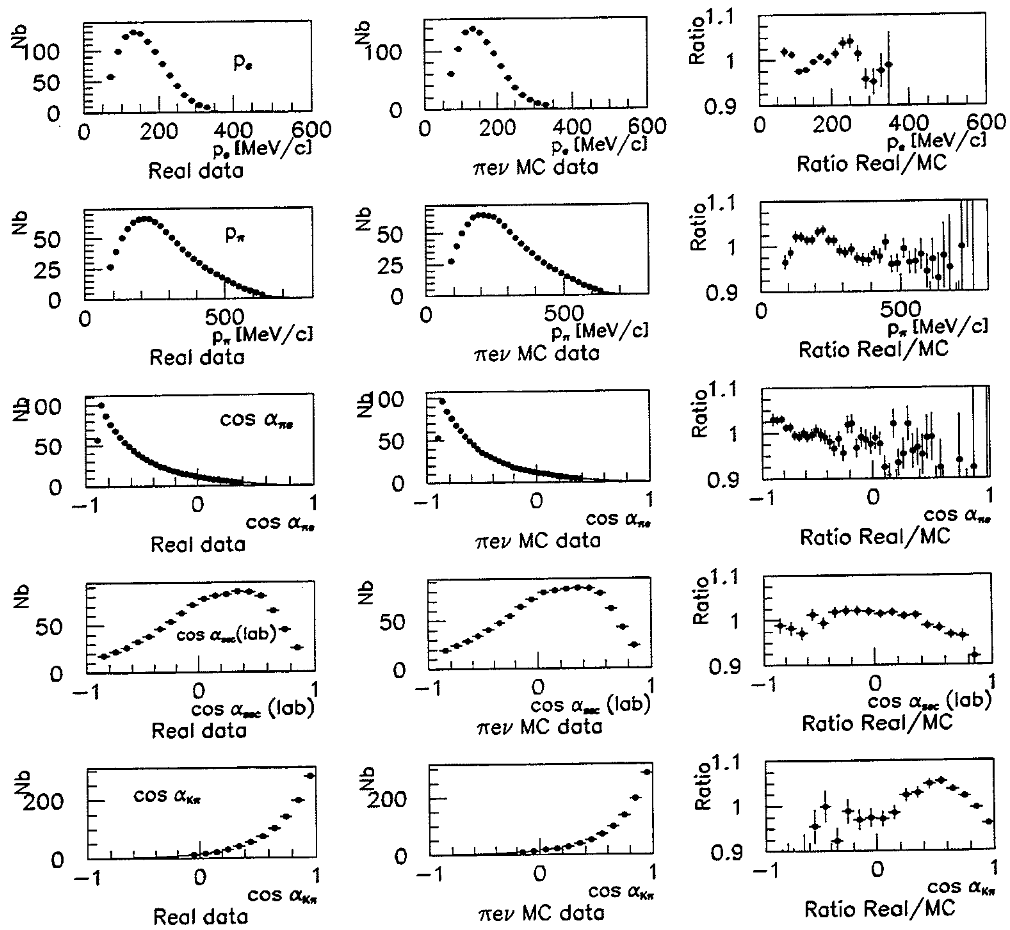

6.6.8 Constrained Fit Probabilities: 1C, 2C and 6C

Last but not least, the constrained fit probabilities are some of the most constraining parameters in the event selection. The simulated distributions of the 1C-Fit and of the 2C-Fit probabilities P_{1C} and P_{2C} are found to be good, but the 6C-Fit shows a large discrepancy between the real and the simulation data (fig. 6.12). This suggests that the uncertainties of the spatial coordinates of the vertices, used specifically in the 6C-Fit, are underestimated in the simulation. However, it will be seen that this has no influence on the q^2-distribution, because the correlation between P_{6C} and q^2 is smaller than 1%. It is thus not necessary to correct for that effect.

Figure 6.12: 1C-, 2C-, and 6C-Fit probabilities.

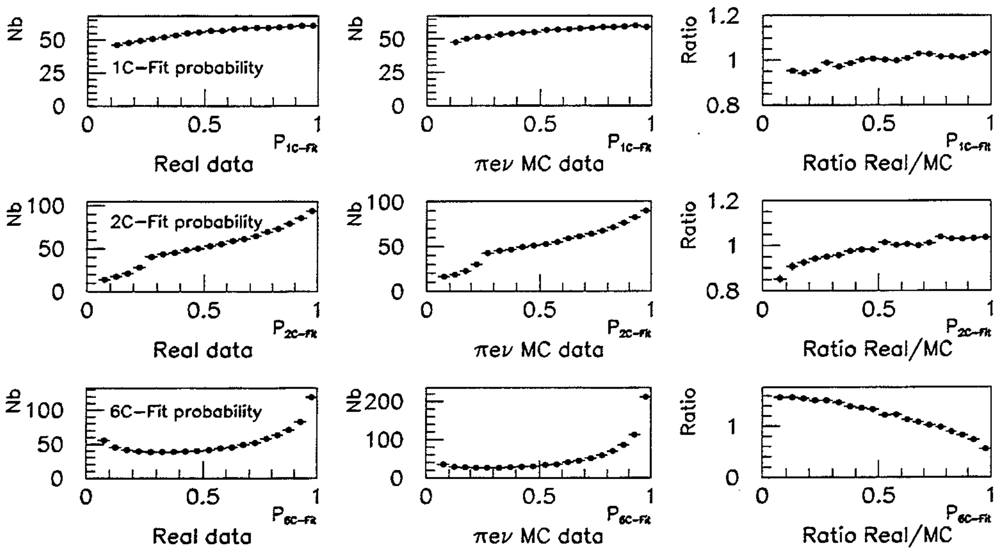

6.7 Acceptance

The acceptance of the whole event selection procedure, from data taking to the final cuts, was determined by comparing the selected and the generated distributions of the simulation data. In order to illustrate the effect of the selection cuts, the rejection factors of the different classes of cuts for the signal ($\pi e\nu$) and the backgrounds ($\pi\mu\nu$, $\pi^+\pi^-$ and $\pi^+\pi^-\pi^0$) are firstly presented. These rejection factors were determined from an analysis of a pre-selected sample of events. For the pre-selection sample, a kaon candidate was requiered, and the 6C-fit cut and the cut on the opening angle of the secondaries in the neutral kaon rest frame were applied. However, no cut on the NNPID probabilities for e/π-separation was applied to obtain this sample. Table 6.1 presents the rejection factors of the different kind of selection criteria for signal and background events. The efficiency of the kinematical cuts for rejecting $\pi^+\pi^-$ events, and of the e/π-separation for all backgrounds can be seen. Finally, the total rejection factors and the number of simulation events selected in each decay channel are also given. From the real data, a total of **366'000** events were selected from the P28-P29 data sample (1995).

Table 6.1: Rejection factors for different classes of criteria applied to the signal and background events. The last row shows the final number of selected simulated events. Note that these numbers are not normalised for branching fractions.

	Rejection factors			
Cuts	$\pi e\nu$	$\pi\mu\nu$	$\pi^+\pi^-$	$\pi^+\pi^-\pi^0$
Pre-selection	821.3	977.9	525.2	4036.4
Event quality cuts	1.3	1.1	1.1	1.2
Logical cuts	1.5	2.1	1.8	2.0
Kinematical cuts	1.4	1.4	30.7	1.3
C-fit probability cuts	1.6	1.1	1.0	7.9
e/π-separation	1.7	7.9	23.4	18.8
Missing mass cut	1.2	2.6	2.1	2.3
Total rejection	7.3×10^3	71.4×10^3	1568.8×10^3	4301.9×10^3
Number of selected events	3'161'338	47'939	197	355

For the measurement of the K^0_{e3} form factor's linear energy dependence parameter λ_+, the relevant variable is the four-momentum transfer q^2 (cf. Section 2.6.1). Therefore, the acceptance should be studied against the q^2 variable. From the generated and the selected distributions, the acceptance against q^2 was found to be relatively constant in the range (0.02 – 0.12) GeV^2 (cf. fig 6.13, first column). The mean absolute acceptance was found to be $\approx$ 0.02% in this range. The decrease at low q^2 is due to the cuts on the opening angle in the K^0 rest frame, and the increase at high q^2 is due to the radiative corrections (cf. Section 6.5). A more detailed analysis on the Dalitz plot ($q^2 = m^2_{e\nu}$ vs $m^2_{e\pi}$) shows that the acceptance is relatively constant in the region of high statistics (cf. fig 6.13, second column).

Figure 6.13: In the left column, the top and the middle plots show the generated and the selected $\pi e\nu$ event distributions of the q^2-variable. The acceptance (third row) is obtain from the ratio of the selected divided by the generated distribution. Similarly, in the right column, one sees the generated and the selected distributions, and the derived acceptance (in units of $10^{-2}\%$) in the Dalitz plot ($q^2 = m^2_{e\nu}$ vs $m^2_{e\pi}$). In both cases, the acceptance is found to be relatively flat in the region of high statistic.

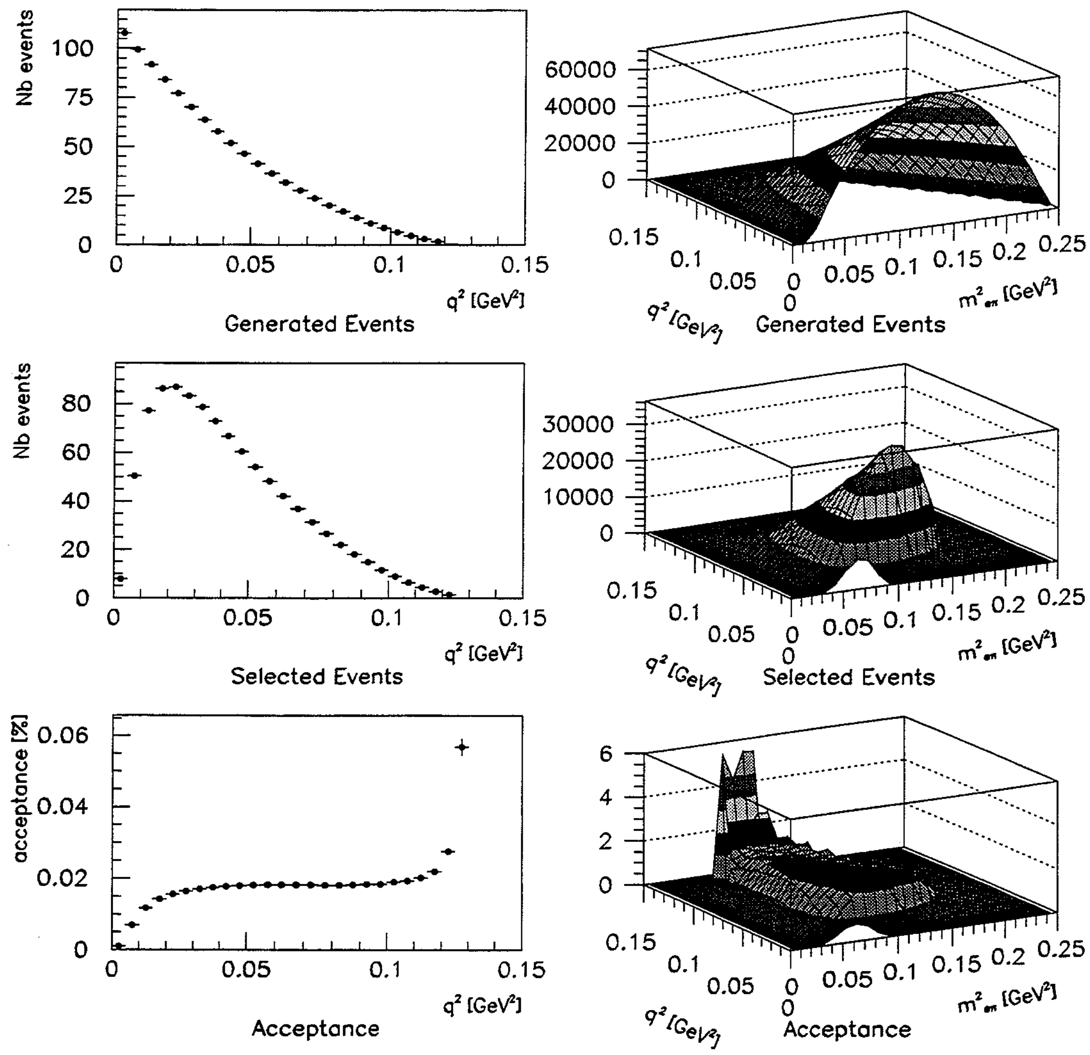

6.8 Backgrounds

The backgrounds were analysed from the Monte-Carlo simulated events for the different decay channels. From their respective branching fractions, the normalised distribution of each decay-channel was determined (fig. 6.14). The $\pi e \nu$ decay channel constitutes the signal. The $\pi e \nu$ events for which the secondary pion was misidentified with the electron, and the electron seen as a pion, were considered as a background, called $e \pi \nu$. For the measurement of the K^0_{e3} form factor however, the $e \pi \nu$ events were considered as signal events, since they also depend on the form factor. These events added to the uncertainty on the determination of q^2 (resolution). The $\pi \mu \nu$, $\pi^+\pi^-$ and $\pi^+\pi^-\pi^0$ events were also considered as backgrounds. Figure 6.15 shows the fraction of each background as a function of q^2. The main contribution was due to the $\pi \mu \nu$ events. These $\pi \mu \nu$ events are distributed all over the q^2-range, with a maximum at high q^2. Although much less important, the $e \pi \nu$ events also contaminate the region at high q^2. On the other hand, the $\pi^+\pi^-$ events are mainly concentrated at low q^2. Finally, the $\pi^+\pi^-\pi^0$ events are so much suppressed by the data selection, that their contribution to the final sample is negligible. Photon conversion events ($\gamma \to e^+e^-$) represent another type of background, but they were rejected by the cut on the opening angle in the laboratory frame. The measured average fractions on the full q^2-range of signal and backgrounds are shown in table 6.2.

Table 6.2: Signal ($\pi e \nu$) and background fractions measured from the simulation data.

Decay-channel	Fraction of the distribution [%]
$\pi e \nu$	92.3
$e \pi \nu$	0.8
$\pi \mu \nu$	6.2
$\pi^+\pi^-$	0.6
$\pi^+\pi^-\pi^0$	0.1

Figure 6.14: Distribution of the signal ($\pi e \nu$) and of the different backgrounds as a function of q^2. Note the logarithmic vertical scale.

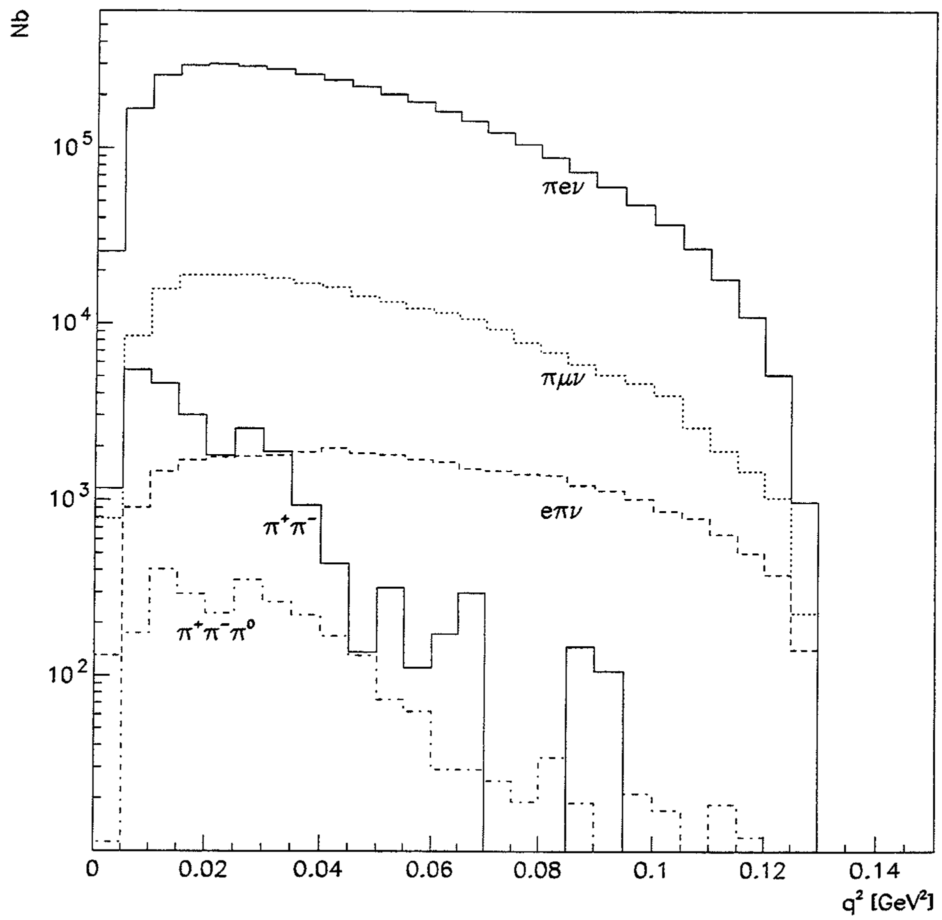

Figure 6.15: Fraction in [%] of each of the backgrounds, as a function of q^2. The total of the backgrounds is shown as a full line. The $\pi^+\pi^-\pi^0$ background is the full line at less than 1%. It is thus negligible.

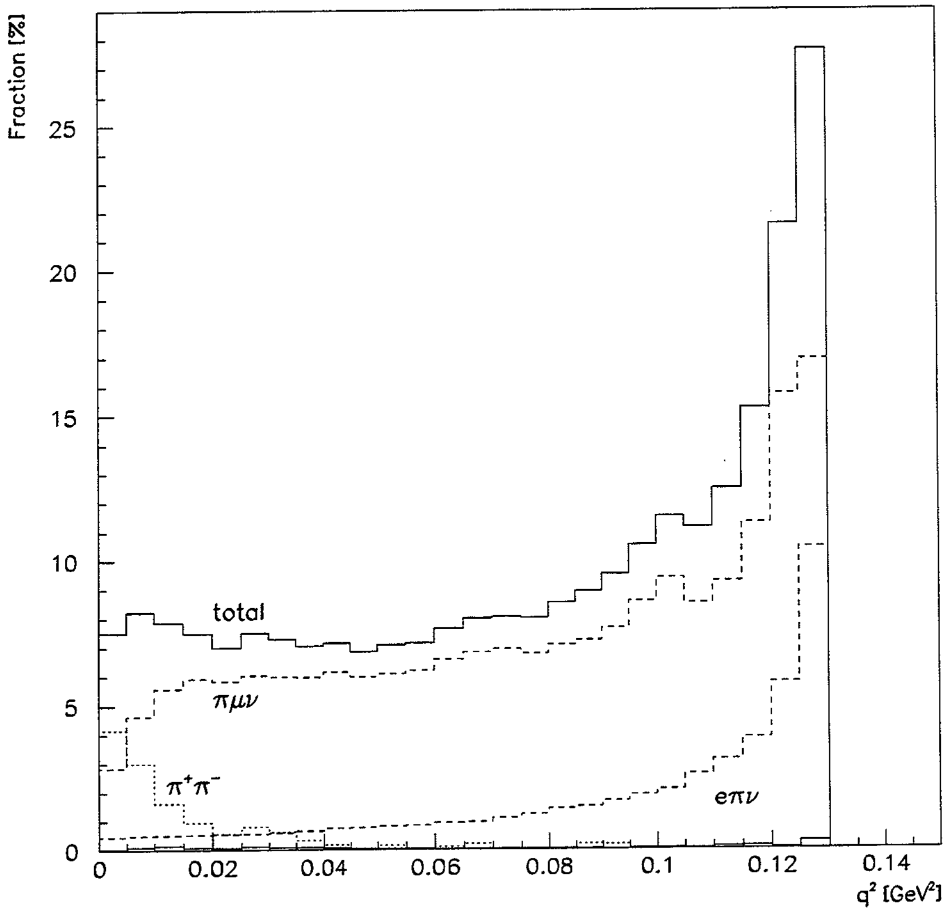

Chapter 7

The K^0_{e3} Form Factor

7.1 Introduction

The principle of the measurement is the following. From Section 2.6), it is known that the K^0_{e3} form factor f_+ depends only on the four-momentum transfer q^2 from the K^0 to the lepton pair. This dependence is expected to be linear (cf. eq. (2.47)). Since the decay amplitude is proportional to f_+, and thus depends on q^2, the parameter λ_+ can be determined by comparing the q^2-spectrum of real data to that of simulation data. Indeed, λ_+ was extracted by fitting the q^2-distribution of the simulation data the q^2-distribution of the real data (Section 7.2). Then, the systematic uncertainties are determined (Section 7.3) and the final result is quoted with all the uncertainties in Section 7.4.

7.2 Fitting Procedure

7.2.1 Relation between Real- and Simulation-Data

The four-momentum transfer q^2 from the K^0 to the lepton pair is given by eq (2.38). The assumed linear dependence of the form factor $f_+(q^2)$ on q^2 is given by eq (2.47). One defines $N_D(q^2)$ as the number of real data events measured in a bin centred at q^2 and $N_S^{\lambda+=0}(q^2)$ as the number of simulated $\pi e\nu$ events (Signal) without q^2-dependence of the form factor ($\lambda_+ = 0$), and $N_i(q^2)$ is the number of selected events of the background channel i.

Since the number of generated events of each channel (signal or background) is arbitrary, one needs a normalisation factor ξ_i for each channel ($\xi_{\pi e\nu}$, $\xi_{\pi\mu\nu}$, $\xi_{\pi^+\pi^-}$ and $\xi_{\pi^+\pi^-\pi^0}$) such that the respective branching fractions are respected. Their values will be determined in Section 7.2.3.

One more overall normalisation constant $\xi_{real\ data}$ is necessary to normalise the number of real data events to the total number of the simulated events ($\pi e\nu$ + backgrounds).

With these definitions, one can write the relation between the real and the simulated q^2-spectra:

$$\xi_{real\ data} \cdot N_D(q^2) = \xi_{\pi e\nu} \cdot N_S^{\lambda+=0}(q^2) \cdot (1 + \lambda_+ \frac{q^2}{m_\pi^2})^2 + \sum_{i=bkg} \xi_i \cdot N_i(q^2) \tag{7.1}$$

where i stands for the background channels.

7.2.2 Resolution

The resolution was studied from the simulation data by distinguishing the generated four-momentum transfer q^2_{gen} from the reconstructed one q^2_{rec}. Their difference $(q^2_{rec} - q^2_{gen})$ is a measure of the detector resolution. In the ideal case of a perfect resolution ($q^2_{gen} = q^2_{rec}$), one could use q^2_{rec} in the fit of λ_+. However, figure 7.1 shows that the mean resolution is of the order of 0.008 GeV^2 (RMS), and depends on the value of q^2. Therefore, since only q^2_{rec} was measured in the real data, the simulation data must

Figure 7.1: The three plot show the resolution ($q^2_{rec} - q^2_{gen}$) for different q^2-ranges: $0.00 < q^2 < 0.05\,\mathrm{GeV}^2$, $0.05 < q^2 < 0.10\,\mathrm{GeV}^2$ and $0.10 < q^2 < 0.15\,\mathrm{GeV}^2$. These plots show the dependence of the resolution on q^2_{rec}. The asymmetric tails seen on the first and last plots are due to the physical limits of the full q^2-range.

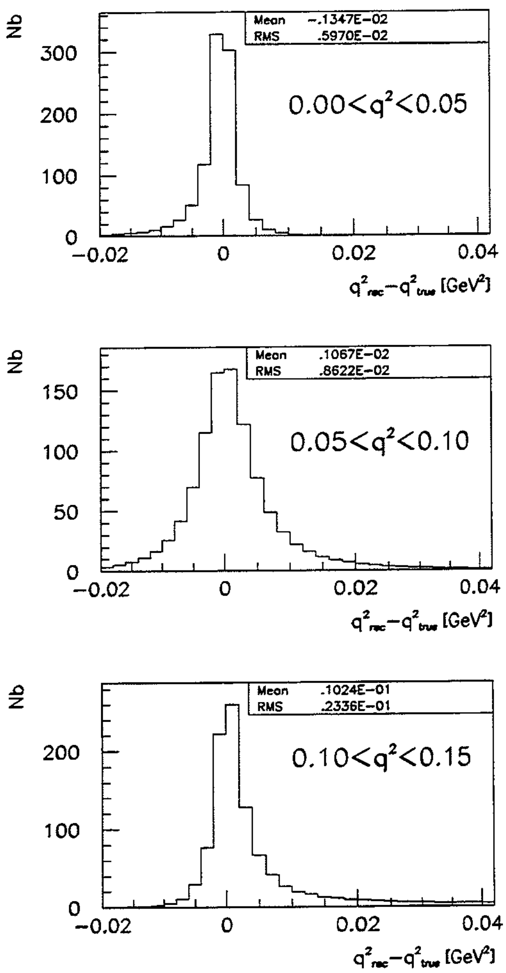

also be presented as a function of q^2_{rec}, to be comparable. However, the amplitude of the process does not depend on q^2_{rec}, but on q^2_{gen}. Hence, the form factor (eq. (2.47)) must be a function of q^2_{gen}, and eq (7.1) becomes

$$\xi_{real\,data} \cdot N_D(q^2_{rec}) = \xi_{\pi e\nu} \cdot N_S^{\lambda_+=0}(q^2_{rec}) \cdot (1 + \lambda_+ \frac{q^2_{gen}}{m^2_\pi})^2 + \sum_{i=bkg} \xi_i \cdot N_i(q^2_{rec}), \tag{7.2}$$

which may also be written as

$$\xi_{real\,data} \cdot N_D(q^2_{rec}) = \xi_{\pi e\nu} \cdot \left[\sqrt{N_S^{\lambda_+=0}(q^2_{rec})} + \frac{\lambda_+}{m_\pi^2}\sqrt{N_S^{\lambda_+=0}(q^2_{rec}) \cdot q^4_{gen}}\right]^2 + \sum_{i=bkg} \xi_i \cdot N_i(q^2_{rec}). \tag{7.3}$$

However, because of the finite resolution, there is not a one to one correspondence between q^2_{rec} and q^2_{gen}, hence, eq. (7.3) cannot be applied. A new variable must therefore be defined in order to be use instead of the term $N_S^{\lambda_+=0}(q^2_{rec}) \cdot q^4_{true}$:

$$N_{S(q^4)}^{\lambda_+=0}(q^2_{rec}) = \sum_j w_j(q^2) \cdot q^4_{true(j)}, \tag{7.4}$$

i.e. the sum of the products of the weights $w_j(q^2)$ of the events reconstructed at the value q^2_{rec}, multiplied by the fourth power of the true four-momentum transfer, $q^4_{gen(j)}$. With this definition, and with

$$N_{S(1)}^{\lambda_+=0}(q^2_{rec}) = N_S^{\lambda_+=0}(q^2_{rec}), \tag{7.5}$$

eq. (7.3) becomes:

$$\boxed{\xi_{real\,data} \cdot N_D(q^2_{rec}) = \xi_{\pi e\nu} \cdot \left[\sqrt{N_{S(1)}^{\lambda_+=0}(q^2_{rec})} + \frac{\lambda_+}{m_\pi^2}\sqrt{N_{S(q^4)}^{\lambda_+=0}(q^2_{rec})}\right]^2 + \sum_{i=bkg} \xi_i \cdot N_i(q^2_{rec})} \tag{7.6}$$

The resolution is now correctly included because each event is weighted with the generated q^2 even if it was reconstructed at a different value. Hence, the same amount of simulated events will be "incorrectly" reconstructed (i.e. events for which the reconstructed q^2_{rec} is different of the true q^2_{gen}) as in real data and the samples may be compared. In other words this procedure introduces the q^2-dependence of the form factor in the simulation data using q^2_{gen}, "like does nature" for the real data, and it displays both samples as a function of q^2_{rec}. Moreover, this is done independently of λ_+.

7.2.3 Determination of the Normalisation Parameters ξ_i

7.2.3.1 Definitions

To satisfy the condition that the relative branching fractions are respected, the parameters ξ_i are defined by

$$\frac{\xi_i \cdot N_i^0}{N^0_{\pi e\nu}(\lambda_+ = 0.03)} = \frac{BR_i^S + BR_i^L}{BR^S_{\pi e\nu} + BR^L_{\pi e\nu}}, \tag{7.7}$$

where BR_i^S and BR_i^L are the branching fractions from the respective K^0_S and K^0_L decays, and N_i^0 is the total number of generated events of channel i (sum of K^0_S and K^0_L decays). One deduces from eq (7.7)

$$\xi_i = \frac{N^0_{\pi e\nu}(\lambda_+ = 0.03)}{N_i^0} \cdot \frac{BR_i^S + BR_i^L}{BR^S_{\pi e\nu} + BR^L_{\pi e\nu}}. \tag{7.8}$$

For semileptonic $\pi e\nu$ events, the effective number of generated events depends on the value of λ_+ and has to be corrected to obtain the reference number $N^0_{\pi e\nu}(\lambda_+ = 0.03)$. One may thus define $\xi_{\pi e\nu}$ as

$$\xi_{\pi e\nu} = \frac{N^0_{\pi e\nu}(0.03)}{N^0_{\pi e\nu}(\lambda_+)}, \tag{7.9}$$

which is exactly what is obtained from eq (7.8) for $i = \pi e\nu$.

7.2.3.2 Number of Generated Events N_i^0

The total number of generated events N_i^0 must be determined in order to be used in eq (7.8). This number is known for the uncorrected simulation events (cf. table 5.1). However, it was modified by the applied corrections. The new value will be calculated now.

Some of the simulation data were generated "flat" in the range of lifetimes between 0 and $30\tau_S$, decay radii between 0 and 45cm and of z-values at the decay vertex within ± 110 cm. One defines A_i as the number of such generated events and B_i as the corresponding number of events without the cuts on the K^0 ($\overline{K}^0$) flight distance. The ratio of B_i over A_i was determined for the events generated flat in lifetime (cf. Section 5.3) from a simulation of "golden events":

$$\frac{B_i}{A_i} = 1.4514. \tag{7.10}$$

For the $\pi^+\pi^-$ events, generated with an exponential decay rate, this ratio is equal to unity.

The effect of the lifetime cut was deduced from the form of the "decay rate weight" w_i (eq (6.3)). Defining C_i as the total number of events, without any time or spatial cuts and weighted by a factor w_i to reproduce the time dependent decay probability of channel i, one obtained:

$$C_{\pi e\nu} = \frac{B_{\pi e\nu}}{30} \cdot 580.142 \tag{7.11}$$

$$C_{\pi\mu\nu} = \frac{B_{\pi\mu\nu}}{30} \cdot 580.142 \tag{7.12}$$

$$C_{\pi^+\pi^-} = B_{2\pi} = A_{2\pi} \tag{7.13}$$

$$C_{\pi^+\pi^-\pi^0} = \frac{B_{3\pi}}{30} \cdot 579.142 \tag{7.14}$$

The numerical factor 30 corresponds to the lifetime range of the generated events $(0 - 30\,\tau_S)$, and the numbers 580.142 and 579.142 are the ratio τ_L/τ_S corrected for CP-violation effects.

Finally, in order to determine the total number of events N_i^0, one needed to correct C_i by a factor I_i^j for each specific weight j applied to the decay channel i. These factors I_i^j are the "$\lambda_+ = 0$" correction ($I^{\lambda}_{\pi e\nu}$) and the radiative corrections ($I^{\Delta RC}_{\pi e\nu}$) for $\pi e\nu$ events and the slope parameters correction ($I^{\text{slope}}_{3\pi}$) for $\pi^+\pi^-\pi^0$ events. The factors I_i^j are the ratios of the total number of weighted divided by unweighted generated events (G'_{mc}/G_{mc}, according to the notation of Section 5.4.1). It must be noted that the weight used to reproduce the exponential decay was already included in the calculation of C_i. The normalisation α at the primary vertex was applied to all events and is the same for each decay channel. Thus, it cancels in the determination of the ξ_i's, as well as the effect of the correction to the primary vertex Dalitz plot, and N_i^0 becomes:

$$N_i^0 = C_i \cdot \prod_j I_i^j \tag{7.15}$$

Using eq (7.8) and (7.15), the expression for ξ_i becomes

$$\boxed{\xi_i = \frac{C_{\pi e\nu}}{C_i} \cdot \frac{I^{\Delta RC}_{\pi e\nu}}{\prod_j I_i^j} \cdot \frac{BR_i^S + BR_i^L}{BR^S_{\pi e\nu} + BR^L_{\pi e\nu}},} \tag{7.16}$$

where all corrections for radius, z and lifetime cuts cancel. It should be noted that $I^{\lambda}_{\pi e\nu}$ does not enter in the numerator of eq. (7.16), because its purpose is to correct the number of generated $\pi e\nu$ events when the value of $\lambda_+ \neq 0.03$. Since in the numerator is the number of generated $\pi e\nu$ events with $\lambda_+ = 0.03$, then $I^{\lambda}_{\pi e\nu} = 1$.

7.2.3.3 Corrections for the $\pi e\nu$ Simulated Events

$\lambda = 0$ correction The semileptonic $\pi e\nu$ events were generated assuming a linear q^2-dependence of the form factor (cf. eq (2.47)), using the value $\lambda_+ = 0.03$. But the total number of events $N(\lambda_+)$ depends on λ_+. It is calculated as follows.

One defines $D_\lambda(q^2)$ as "a kind" of probability for one event to have a momentum transfer q^2. Then, one may write

$$N(\lambda_+) = N_0 \int_{-\infty}^{\infty} D_\lambda(q^2) dq^2 = N_\lambda. \tag{7.17}$$

In the particular case where $\lambda_+ = 0$,

$$N(0) = N_0 \int_{-\infty}^{\infty} D_0(q^2) dq^2 = N_0. \tag{7.18}$$

From these definitions one concludes that $D_0(q^2)$ is exactly a probability because it is normalised to 1, while $D_\lambda(q^2)$ is not but is related to $D_0(q^2)$ by

$$D_\lambda(q^2) = D_0(q^2) \cdot (1 + \lambda_+ \frac{q^2}{m_\pi^2})^2, \tag{7.19}$$

using eq. (2.47). Combining eqs (7.17) and (7.19) one finds:

$$N(\lambda_+) = N_0 \int_{-\infty}^{\infty} D_0(q^2) \cdot (1 + \lambda_+ \frac{q^2}{m_\pi^2})^2 \cdot dq^2. \tag{7.20}$$

After expanding the bracket, eq (7.20) becomes

$$N(\lambda_+) = N_0 \int_{-\infty}^{\infty} D_0(q^2) dq^2 + 2\frac{\lambda_+}{m_\pi^2} N_0 \int_{-\infty}^{\infty} D_0(q^2) q^2 dq^2 + \left(\frac{\lambda_+}{m_\pi^2}\right)^2 N_0 \int_{-\infty}^{\infty} D_0(q^2) q^4 dq^2, \tag{7.21}$$

which can be written as

$$N(\lambda_+) = N_0 \cdot \left(1 + 2\frac{\lambda_+}{m_\pi^2}\overline{q^2} + (\frac{\lambda_+}{m_\pi^2})^2 \overline{q^4}\right), \tag{7.22}$$

where $\overline{q^2}$ and $\overline{q^4}$ are the mean values of the q^2- and q^4- distributions. These distributions were produced using the event generator of semileptonic events, yielding the mean values:

$$\overline{q^2} = 0.033350 \text{ GeV}^2, \tag{7.23}$$

and

$$\overline{q^4} = 0.0017845 \text{ GeV}^4. \tag{7.24}$$

Hence, the multiplicative factor $I^\lambda_{\pi e\nu}(\lambda_+)$ is finally

$$I^\lambda_{\pi e\nu}(\lambda_+) = \frac{N^0(\lambda_+)}{N^0(0.03)} = \frac{1 + 2\frac{\lambda_+}{m_\pi^2}\overline{q^2} + (\frac{\lambda_+}{m_\pi^2})^2\overline{q^4}}{1 + 2\frac{0.03}{m_\pi^2}\overline{q^2} + (\frac{0.03}{m_\pi^2})^2\overline{q^4}} \tag{7.25}$$

Radiative Corrections to K^0_{e3} Decays The integration over the Dalitz plot of the radiative corrections (cf. Section 6.5) gives the value $I_{\triangle RC}$. The simulation of 10^6 generic $\pi e\nu$ events correspond to $1.0481 \cdot 10^6$ corrected events. Thus,

$$I_{\triangle RC} = 1.0481 \pm 0.0015 \tag{7.26}$$

7.2.3.4 Corrections for the $\pi^+\pi^-\pi^0$ Simulated Events

Slope Parameters The effect of the slope parameters in $\pi^+\pi^-\pi^0$ simulated events was integrated over the Dalitz plot (cf. Section 5.4.1), and gave the value of $I^{\text{slope}}_{3\pi}$:

$$I^{\text{slope}}_{3\pi} = 1.12 \pm 0.01 \tag{7.27}$$

7.2.3.5 Corrections for Real Data

The case of the real data is somehow different because the generated number of real events (G_{rd} according to the notation of Section 5.4.1) is unknown. Therefore, the effects of the corrections w_{reg} and α cannot be evaluated, and the normalisation factor $\xi_{real\ data}$ defined in Section 7.2.1 is left free in the fit of λ_+.

7.2.3.6 Values of the Correction Parameters ξ_i

The values of the parameters ξ_i were then obtained from eq. (7.16) (cf. table 7.1). The uncertainties on the parameters cannot be absolutely determined, mainly because of the indetermination introduced by the PID corrections on the total number of generated events (Section 5.4.2). Therefore, the uncertainties for each ξ_i is estimated to be within $\pm 10\%$.

Table 7.1: Parameters ξ_i for each decay channel i calculated from eq (7.16), taking the branching fractions from ref. [8]. A_i is the total number of generated events. N_i^0 is the corresponding number of events for all lifetimes, all decay distances and after corrections.

Channel	A_i	N_i^0	Branching Fraction	ξ_i
$\pi e\nu(\lambda_+ = 0.03)$	791'787'044	23'291'574'780	$0.000670(7)/K^0_S+0.3878(27)/K^0_L$	$1.0/I_{ff}$
$\pi\mu\nu$	122'560'000	3'438'313'746	$0.000469(6)/K^0_S+0.2717(25)/K^0_L$	4.746
$\pi^+\pi^-$	380'000'000	380'000'000	$0.6861(28)/K^0_S+0.002067(35)/K^0_L$	108.6
$\pi^+\pi^-\pi^0$	48'900'000	1'533'883'569	$0.1256(20)/K^0_L$	4.910

7.2.4 Determination of the K^0_{e3} Form Factor Linear Energy Dependence Parameter λ_+

In order to determine the form factor slope parameter λ_+, a χ^2 minimisation is performed on the expression given by eq (7.6):

$$\chi^2 = \sum_{q^2\ \text{bin}} \frac{1}{\sigma^2_{q^2\ \text{bin}}} \cdot \Bigg(\xi_{real\ data} \cdot N_D(q^2_{rec}) \\ - \Xi_{\pi e\nu} \cdot \left[\sqrt{N^{\lambda_+=0}_{S(1)}(q^2_{rec})} + \frac{\lambda_+}{m^2_\pi} \sqrt{N^{\lambda_+=0}_{S(q^4)}(q^2_{rec})} \right]^2 - \sum_{i=bkg} \Xi_i \cdot N_i(q^2_{rec}) \Bigg)^2, \tag{7.28}$$

where the Ξ_i are the values of the normalisation factors.

The form of $\sigma^2_{q^2\ \mathrm{bin}}$, for each individual q^2-bin, depends on the variance σ^2_D of the number N_D of real data events, on the variance σ^2_i of the number N_i of background events, on the variances $\sigma^2_{S(1)}$ and $\sigma^2_{S(q^4)}$ of $\pi e\nu$ simulated events $N_{S(1)}$ and $N_{S(q^4)}$, and finally on the covariance $\mathrm{Cov}_{(S(1),S(q^4))}$ between the last two variables[1]:

$$\begin{aligned}
\sigma^2_{q^2\ \mathrm{bin}} =& \xi^2_{real\ data} \cdot \sigma^2_D \\
&+ \xi^2_{\pi e\nu} \cdot \left(1 + \frac{\lambda_+}{m^2_\pi} \cdot \sqrt{\frac{N^{\lambda_+=0}_{S(q^4)}}{N^{\lambda_+=0}_{S(1)}}}\right)^2 \cdot \sigma^2_{S(1)} \\
&+ \xi^2_{\pi e\nu} \cdot \left(\sqrt{\frac{N^{\lambda_+=0}_{S(1)}}{N^{\lambda_+=0}_{S(q^4)}}} + \frac{\lambda_+}{m^2_\pi}\right)^2 \cdot \frac{\lambda_+}{m^2_\pi} \cdot \sigma^2_{S(q^4)} \\
&+ 2 \cdot \xi^2_{\pi e\nu} \cdot \frac{\lambda_+}{m^2_\pi} \cdot \sqrt{\frac{N^{\lambda_+=0}_{S(1)}}{N^{\lambda_+=0}_{S(q^4)}}} \cdot \left(1 + \frac{\lambda_+}{m^2_\pi}\sqrt{\frac{N^{\lambda_+=0}_{S(q^4)}}{N^{\lambda_+=0}_{S(1)}}}\right)^2 \cdot \mathrm{Cov}_{(S(1),S(q^4))} \\
&+ \sum_i \xi^2_i \cdot \sigma^2_i
\end{aligned} \qquad . \qquad (7.29)$$

The Ξ_i values may either be fixed at the values of ξ_i previously calculated, or they may be free parameters of the fit. If the term

$$\sum_{i=bkg} \frac{(\Xi_i - \xi_i)^2}{\sigma^2_{\xi i}} \qquad (7.30)$$

is added to the expression of the χ^2, the systematic errors on the value of λ_+, due to the uncertainties on the background levels, are directly included in the statistical error. In eq. (7.30), Ξ_i is the free parameter, ξ_i is the previously calculated normalisation value, and $\sigma_{\xi i}$ is the uncertainty on ξ_i.

The q^2-distributions were determined for the real data, for the simulated signal ($\pi e\nu$ and $e\pi\nu$ channels[2]) and for the simulated backgrounds ($\pi\mu\nu$, $\pi^+\pi^-$ and $\pi^+\pi^-\pi^0$ channels). These distributions were used to perform the fit.

In order to check the values of the normalisation factors ξ_i, the fit was firstly performed in the Dalitz plot defined by the two invariant masses $m^2_{e\nu}$ ($= q^2$) and $m^2_{e\pi}$. In this plot, the different channels are better separated than in the one-dimensional q^2-distribution. The values of the ξ_i's were left free, and

[1] The covariance $\mathrm{Cov}_{(S(1),S(q^4))}$ was computed as follows. The statistical weight of one event is $x = 1 \pm 1$. Then, $N_{S(1)} = \sum_i w_i \cdot x$ and $N_{S(q^4)} = \sum_i w_i \cdot q^4_i \cdot x$, from which one deduces the covariance between $f_1 = w_i \cdot x$ and $f_2 = w_i \cdot q^4_i \cdot x$:

$$\mathrm{Cov}_{(f_{1i},f_{2i})} = \frac{\partial f_{1i}}{\partial x}\frac{\partial f_{2i}}{\partial x} \cdot \mathrm{Cov}_{(x,x)} = w_i \cdot w_i q^4_i \cdot 1 = w^2_i \cdot q^4_i$$

Finally,

$$\mathrm{Cov}_{(S(1),S(q^4))} = \sum_i \frac{\partial N_{S(1)}}{\partial f_{1i}}\frac{\partial N_{S(q^4)}}{\partial f_{2i}} \cdot \mathrm{Cov}_{(f_{1i},f_{2i})} = \sum_i 1 \cdot 1 \cdot w^2_i \cdot q^4_i = \sum_i w^2_i \cdot q^4_i \,.$$

[2] The q^2-distribution measured from the $e\pi\nu$ channel depends on the K^0_{e3} form factor, although the corresponding events are badly reconstructed. Hence, the events from this channel have to be included in the signal (cf. Section 6.8).

no term was added to the χ^2 to constrain their values. Since the background was important at low and high q^2 (cf. Section 6.8), the fit of the background fractions was performed on the full range of q^2. The measured values of the ξ_i's are found to be compatible with the calculated values (cf. table 7.1) within $1.5\,\sigma$ (cf. table 7.2). The large uncertainties are due to the small statistical fractions of the background

Table 7.2: Measured background fraction from a χ^2-fit leaving these fractions free.

Parameter	Fitted value	Difference to the calculated value
$\xi_{\pi\mu\nu}$	7.40 ± 1.72	$1.54\,\sigma$
$\xi_{\pi^+\pi^-}$	146.8 ± 33.9	$1.13\,\sigma$
$\xi_{\pi^+\pi^-\pi^0}$	27.0 ± 33.1	$0.67\,\sigma$

channels. This result shows that the simulated data are sufficiently well described, and that the measured and the calculated values of ξ_i are compatible. The calculated values (table 7.1) can then be used with the 10% uncertainties quoted previously:

$$\begin{aligned} \xi_{\pi\mu\nu} &= 4.746 \pm 0.475 \\ \xi_{\pi^+\pi^-} &= 108.6 \pm 10.9 \\ \xi_{\pi^+\pi^-\pi^0} &= 4.910 \pm 0.491. \end{aligned}$$

For the final determination of λ_+, the fit was applied to the one-dimensional distribution of q^2, in the range:

$$0.02 < q^2 < 0.12\,\mathrm{GeV}^2. \tag{7.31}$$

These limits were chosen accordingly to the reasons seen previously, i.e.:

- The PID corrections showed that the q^2-distribution is sensitive to the quality of the simulation beyond the limits given by eq. (7.31) (cf. Section 5.4.2).
- The primary vertex kinematics corrections also showed a sensitivity for the values of q^2 below $0.01\,\mathrm{GeV}^2$ (cf. Section 5.4.3).
- In the selected range, the radiative corrections remain relatively constant, while outside this range, the corrections become large and uncertain (cf. Section 6.5).
- The acceptance is not flat for $q^2 < 0.02\,\mathrm{GeV}^2$ and $q^2 > 0.12\,\mathrm{GeV}^2$ (cf. Section 6.7).
- The $\pi^+\pi^-$ background is mainly situated at $q^2 < 0.02\,\mathrm{GeV}^2$, and the $\pi\mu\nu$ background has its maximum at high q^2-values (cf. Section 6.8).

For the final fit of λ_+, the normalisation factors were kept fixed in eq. 7.28. Two free parameters remained: λ_+ and $\xi_{real\,data}$. The result of the fit is:

$$\lambda_+ = 0.02446 \pm 0.00122,$$

with $\chi^2 = 33.0$ for 18 degrees of freedom, corresponding to a confidence level CL = 1.7%. The real data normalisation parameter is found to be $\xi_{real\,data} = 10.187 \pm 0.027$. The correlation ρ between $\xi_{real\,data}$ and λ_+ is $\rho = 0.645$. Figure 7.2 shows the dependence of the form factor $f_+(q^2)$ on q^2, where the form factor is normalised such that $f_+(q^2 = 0) = 1.0$ (Eqs (2.47) and (7.6) were used to calculate the ratio $f_+(q^2)/f_+(0)$, taking into account the backgrounds and the resolution).

Figure 7.2: The $f_+(q^2)$ form factor dependence on q^2, normalised such that $f_+(q^2=0)=1.0$. The result of the fit (line) is superimposed to the data points (crosses). The q^2-range of the figure corresponds to the range used in the fit.

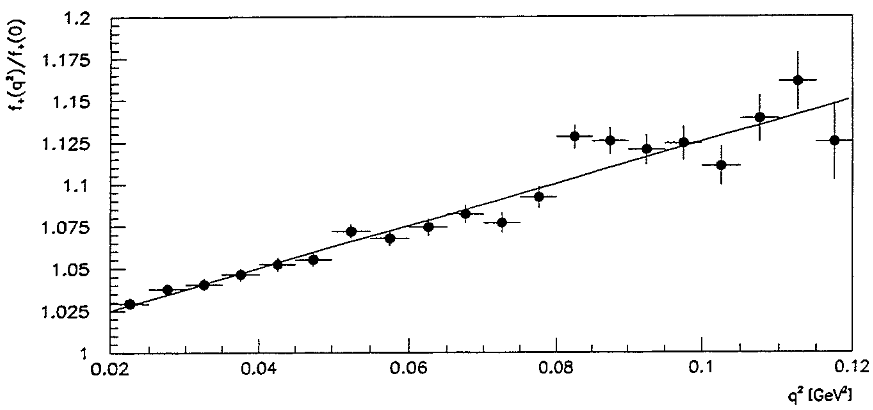

7.3 Systematics

The contribution of different effects to the systematic uncertainties are discussed now, and are summarised in table 7.4.

7.3.1 Background

The uncertainty on the background level was estimated to be about $\pm 10\%$. Two different methods were applied to measure the effect of these uncertainties:

1. The term given by eq. (7.30) was added to the χ^2, with the values calculated previously, and the Ξ_i of the backgrounds were left free. The result of the fit is then:

$$\lambda_+ = 0.02448 \pm 0.00134.$$

The quadratic difference between the new uncertainty (0.00134) and the uncertainty determined with fixed values of Ξ_i (0.00122) gives the systematic uncertainty due to the background:

$$\sigma_{\text{syst}}(bkg) = 0.00055.$$

2. The Ξ_i were fixed at $\xi \pm 10\%$. Half the difference of the λ_+ values determined for $+10\%$ and -10% corresponds to a $1\,\sigma$ effect on λ_+:

Background channel	$\lambda_+(\xi_i + 10\%)$	$\lambda_+(\xi_i - 10\%)$	σ_{syst}
$\pi\mu\nu$	0.02403	0.02489	0.00043
$\pi^+\pi^-$	0.02459	0.02433	0.00013
$\pi^+\pi^-\pi^0$	0.02447	0.02444	0.00003

The three uncertainties added quadratically give the total contribution of the background to the λ_+ uncertainty:

$$\sigma_{\text{syst}}(bkg) = 0.00045.$$

Both methods give similar results. However, the first method takes into account the correlations between the backgrounds, making its calculated $\sigma_{\text{syst}}(bkg)$ somewhat larger and more accurate. Hence,

$$\sigma_{\text{syst}}(bkg) = 0.00055.$$

7.3.2 Boundaries of the q^2-Range

The sensitivity of the measured λ_+ value on the fit boundaries was studied by changing these limits. The lower bound was varied by steps of 0.005 GeV^2 in the range $0.01 < q^2 < 0.05\,\text{GeV}^2$, with a constant upper bound at $q^2 = 0.12\,\text{GeV}^2$. Similarly, the upper bound was varied in the range $0.09 < q^2 < 0.013\,\text{GeV}^2$, with a constant lower bound at $q^2 = 0.02\,\text{GeV}^2$. The results are shown in figure 7.3. The

Figure 7.3: Dependence of λ_+ on the q^2-limits of the fit. The horizontal line represent the mean value. For the lower bound, the two first values are not taken into account for the systematics study.

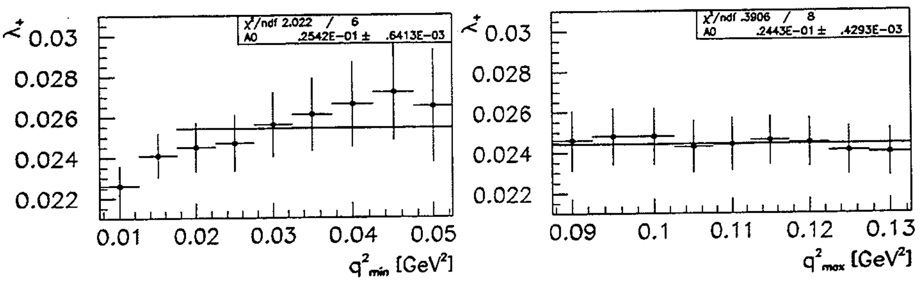

value of λ_+ is independent of the upper bound, and the dependence on the lower bound is not statistically significant. Hence, the possible systematic effect can be neglected. There is thus no systematic effect due to the boundaries of the q^2-range.

7.3.3 Variables Used in the Calculation of q^2

The momentum transfer q^2 was calculated from the neutral kaon momentum p_{K^0}, the pion momentum p_π and the cosine of the angle between these two particles $\cos\alpha_{K\pi}$. The value of λ_+ should be independent of these variables. However, any systematic effects due to the quality of the simulation data for the description of these variables can be studied by measuring λ_+ for different slices of p_{K^0}, p_π and $\cos\alpha_{K\pi}$. The data were separated into $N = 5$ different ranges for each of the variables, and $\lambda_+(i)$ was determined for each slice i. The χ^2-fit of a constant over the N independent measured values is expected to have a value equal to the number of degrees of freedom ($ndf = N - 1 = 4$), if no systematic effect is involved. For larger χ^2, a factor α is defined such that

$$\frac{\chi^2}{\alpha^2} = N - 1. \tag{7.32}$$

The uncertainty on each of the N measurements is then multiplied by α, such that the uncertainty on the mean value is also multiplied by α. Hence, the variance of the systematic effect under study is deduced to be the difference between the modified and the non-modified variances:

$$\sigma^2_{\text{syst}} = (\alpha^2 - 1)\sigma^2_{\text{stat}} \tag{7.33}$$

More details about this method can be found in ref. [8]. Figure 7.4 shows the result for the three variables used for the determination of q^2, i.e. p_{K^0}, p_π and $\cos\alpha_{K\pi}$.

Figure 7.4: Dependence of λ_+ on the neutral kaon momentum p_{K^0}, the pion momentum p_π and the cosine of the angle between these two particles $\cos\alpha_{K\pi}$. The first point of each plot corresponds to the fit on all the data. The five next points correspond two five independent slices in the physical range of each variable.

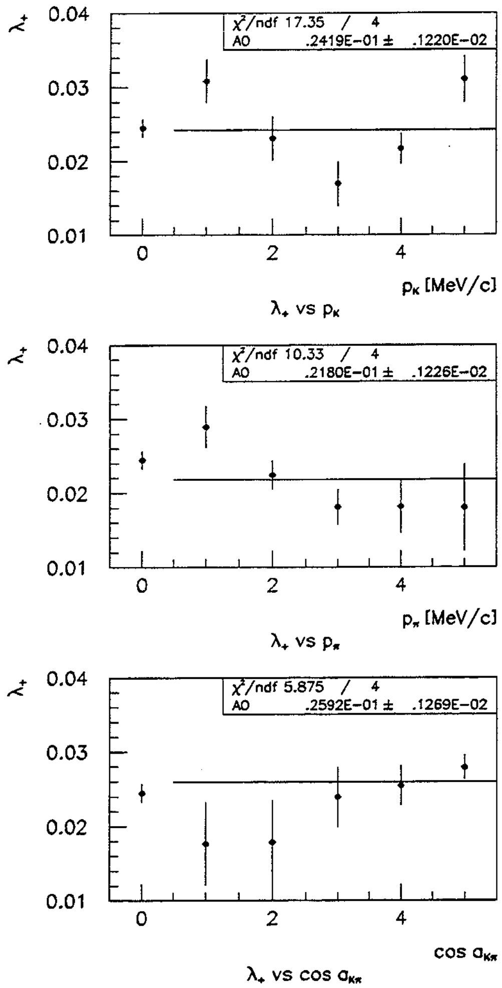

The values of the χ^2/ndf and the corresponding systematic uncertainties were calculated with $\sigma_{\text{stat}} = 0.00122$, and are summarised in table 7.3. The total uncertainty due to the three variables is obtained by adding the individual values quadratically:

$$\sigma_{\text{syst}}(\text{variables}) = 0.00284.$$

7.3.4 Other Effects

- The description of the other variables, like the kinematics of the charged primary particles, or of the electron might also induce systematic effects. However, these effects are all included in the

Table 7.3: Systematic uncertainties due to the neutral kaon momentum p_{K^0}, the pion momentum p_π and the cosine of the angle between these two particles $\cos\alpha_{K\pi}$.

Variable	χ^2/ndf	σ_{syst}
p_{K^0}	4.336	0.00223
p_π	2.583	0.00154
$\cos\alpha_{K\pi}$	1.469	0.00084

description of p_{K^0}, p_π and $\cos\alpha_{K\pi}$. Hence, all the contributions of these variables are included in the previously determined σ_{syst}(variables).

- It has also been checked that the value of λ_+ is independent of the neutral kaon strangeness. The results obtained for $\lambda_+(K^0)$ and $\lambda_+(\overline{K^0})$ were found to be compatible (cf. Section 7.4).
- The possible effect of the correction weights is also included in σ_{syst}(variables).
- It should be noted that the radiative corrections slightly modified the λ_+ value, namely:

$$\lambda_+(\Delta RC) - \lambda_+(No\Delta RC) \approx -0.001.$$

  Hence, the possible uncertainty introduced by the radiative corrections is certainly much smaller than 0.001, and thus negligible.
- The addition of a quadratic term to the energy dependence of the form factor does not improve the quality of the fit, and the quadratic term is compatible with zero. Hence, it can be neglected.

Finally, a summary of the relevant systematic effects is given in table 7.4.

Table 7.4: Summary of the systematic uncertainties.

Source	σ_{syst}
Background level	0.00055
q^2-range for the fit	$\ll 0.00001$
Description of the p_{K^0} spectrum	0.00223
Description of the p_π spectrum	0.00154
Description of the $\cos\alpha_{K\pi}$ spectrum	0.00084
Total	**0.00289**

7.4 Final Results

The final result for the linear energy dependence parameter λ_+, determined from the P28-P29 data (1995) with 366′000 reconstructed K^0 ($\overline{K}^0$) $\to \pi e \nu$ events, is

$$\boldsymbol{\lambda_+ = 0.0245 \pm 0.0012_{\text{stat}} \pm 0.0029_{\text{syst}}}.$$

This result shows that the uncertainty on λ_+ is dominated by systematic effects, because the large statistics of the simulated and of the real data emphasize the differences between the two data samples.

The total uncertainty can be calculated from the quadratic sum of the statistical and the systematic uncertainties:

$$\boldsymbol{\lambda_+ = 0.0245 \pm 0.0031}.$$

This result should be compared with the other measurements given in table 2.1. Note that only two measurements have smaller uncertainties. Combining all the measurements with our result, the new world average becomes:

$$\boldsymbol{\lambda_+ = 0.0291 \pm 0.0014},$$

where a scaling factor of 1.2 has been applied, according to the procedure of ref. [8]. This new world average may be compared with the corresponding parameter $\lambda_+(K^\pm)$ for the form factor of the charged kaon semileptonic decays ($K^\pm_{e3}$) [8]:

$$\lambda_+(K^\pm) = 0.0286 \pm 0.0022.$$

Both values of $\lambda_+(K^0)$ and $\lambda_+(K^\pm)$ should be equal if the $\Delta I = 1/2$ rule holds [13]. The mean values quoted above for $\lambda_+(K^0)$ and $\lambda_+(K^\pm)$ are very well compatible, showing thus no deviation from the $\Delta I = 1/2$ rule.

Finally, a test of CP-violation in the semileptonic decay amplitude was performed with the measured values of λ_+ for K^0 and $\overline{K}^0$ decays, with the results:

$$\lambda_+(K^0) = 0.0262 \pm 0.0017_{\text{stat}} \pm 0.0038_{\text{syst}},$$

and

$$\lambda_+(\overline{K^0}) = 0.0227 \pm 0.0017_{\text{stat}} \pm 0.0031_{\text{syst}}.$$

The systematic uncertainties were obtained with the same method as described previously. Using the fact that the weighted mean of $\lambda_+(K^0)$ and $\lambda_+(\overline{K^0})$ should have the same systematic uncertainty as the value of λ_+ determined from the full sample, the correlation ρ between the systematic uncertainties of $\lambda_+(K^0)$ and $\lambda_+(\overline{K^0})$ was found to be $\rho = 0.41$.

The asymmetry A_λ constructed with $\lambda_+(K^0)$ and $\lambda_+(\overline{K^0})$ is a measure of direct CP-violation in the decay. This asymmetry was deduced to be

$$A_\lambda = \frac{\lambda_+(K^0) - \lambda_+(\overline{K^0})}{\lambda_+(K^0) + \lambda_+(\overline{K^0})} = 0.072 \pm 0.092.$$

From this result, the following limit, at the 68% confidence level, can be set on $|A_\lambda|$:

$$\boldsymbol{|A_\lambda| < 0.13}.$$

Therefore, no CP-violation in the semileptonic decay amplitude is seen, as expected from the standard model.

Chapter 8

Conclusion

The linear energy dependence parameter λ_+ of the K^0_{e3} form factor has been measured in several experiments. The obtained results are not always compatible, and the latest publication dates back nearly twenty years.

The data sample from the CPLEAR experiment contained a large number of K^0_{e3} decays. In the present work, these data were used to evaluate the K^0_{e3} form factor. The method which was employed relied on an analysis of the Dalitz plot distribution. The measured density was compared with the simulated density for events generated with a constant matrix element. From a total of 366′000 reconstructed $K^0(\overline{K}^0) \to \pi e \nu$ events, one obtained the result:

$$\boldsymbol{\lambda_+ = 0.0245 \pm 0.0012_{\text{stat}} \pm 0.0029_{\text{syst}}}.$$

The uncertainty on λ_+ is dominated by systematic effects originating from the simulated data sample. This result was included in the list of all available measurements, and the new world average was determined to be

$$\boldsymbol{\lambda_+ = 0.0291 \pm 0.0014}.$$

This new world average was compared with the corresponding form factor's linear energy dependence of the charged kaon decays $K^{\pm}_{e3}$. No deviation from the $\Delta I = 1/2$ rule was found.

Finally, a limit was given on the value of the asymmetry

$$\boldsymbol{|A_\lambda| = \left| \frac{\lambda_+(K^0) - \lambda_+(\overline{K^0})}{\lambda_+(K^0) + \lambda_+(\overline{K^0})} \right| < 0.13},$$

at the 68% confidence level, thus showing no direct CP-violation in the semileptonic decay amplitude of the neutral kaons.

Bibliography

[1] J.H. Christenson et al., Phys. Rev. Lett. **13** (1964) 138

[2] M. Kobayashi and K. Maskawa, Prog. Theor. Phys. **49** (1973) 652

[3] G. Rochester and C. Butler, Nature **160** (1947) 855

[4] V. Weisskopf and E. Wigner, Z. Phys. **63** (1930) 54, **65** (1930) 18

[5] T. Nakada, CP Violation in K- and B-Meson Decays, PSI-PR-91-02 (1991)

[6] T. Nakada, Review on CP Violation, talk given at XVI Int. Symp. on Lepton-Photon Int., Cornell (1993)

[7] R. Adler et al., CPLEAR Collaboration, Phys. Lett. **B363** (1995) 237

[8] Particle Data Group, Review of Particle Physics, Phys. Rev. **D54** (1996) 1

[9] R. Adler et al., Results from $\pi^+\pi^-$ decays, to be published in Phys. Lett. B

[10] A. Angelopoulos et al., CPLEAR Collaboration, Results from $\pi^0\pi^0$decays, to be published in Phys. Lett. B, CERN-EP/97-148

[11] R. Adler et al., CPLEAR Collaboration, Phys. Lett. **B407** (1997) 193

[12] R. Adler et al., CPLEAR Collaboration, Results from $\pi^0\pi^0\pi^0$decays, to be published in Phys. Lett. B, CERN-EP/98-04

[13] L. Chounet et al., Phys. Reports **4** (1972) 199

[14] R. Blumenthal et al., Phys. Rev. Lett. **34** (1975) 164

[15] J. Gasser and H. Leutwyler, Nucl. Phys. **B250** (1985) 517

[16] E. Shabalin, Sov. J. Nucl. Phys. **51** (1990) 296

[17] A. Afanasev and W. Buck, Phys. Rev. **D55** (1997) 4380

[18] H. Ito et al., Phys. Lett. **B287** (1992) 23

[19] Y. Kalinovsky et al., Phys. Lett. **B399** (1997) 22

[20] V. Birulev et al., Nucl. Phys. **B182** (1981) 1

[21] Engler et al., Phys. Rev. **D18** (1978) 623

[22] Hill et al., Phys. Lett. **B73** (1978) 483

[23] G. Gjesdal et al., Nucl. Phys. **B109** (1976) 118

[24] Buchanan et al., Phys. Rev. **D11** (1975) 457

[25] Wang et al., Phys. Rev. **D9** (1974) 540

[26] Albrow et al., Nucl. Phys. **B58** (1973) 22

[27] Brandenburg et al., Phys. Rev. **D8** (1973) 1978

[28] Neuhofer et al., Phys. Lett. **B41** (1972) 642

[29] Bisi et al., Phys. Lett. **B36** (1971) 533

[30] Chien et al., Phys. Lett. **B35** (1971) 261

[31] Aronson et al., Phys. Rev. Lett. **20** (1968) 287

[32] Basile et al., Phys. Lett. **B26** (1968) 542

[33] Firestone et al., Phys. Rev. Lett. **18** (1967) 176

[34] Kadyk et al., Phys. Rev. Lett. **19** (1967) 597

[35] Lowys et al., Phys. Lett. **B24** (1967) 75

[36] Fisher et al., ANL **7130** (1965) 83

[37] Luers et al., Phys. Rev. **B133** (1967) 1276

[38] R. Adler et al., CPLEAR Collaboration, NIM **A379** (1996) 76

[39] R. Adler et al., NIM **A390** (1997) 293

[40] L. Faravel, PhD thesis, University of Fribourg (1993)

[41] Ch. Bula, PhD thesis, ETH Zürich (1992)

[42] F. Sauli, CERN report 77-09 (1977)

[43] W.R. Leo, Techniques for Nuclear and Particle Physics Experiments, Ed. Springler-Verlag, 2nd edition (1994)

[44] M. Rose and S. Korff, Phys. Rev. **59** (1941) 850

[45] CPLEAR Offline Group, CPGEANT User Manual, Geneva (1992)

[46] Application Software Group, GEANT User Guide, CERN Program Library Long Writeup W5013 (1994)

[47] CERN Program Library, GENBOD User Guide, CERN Writeup W5013 (1975)

[48] J.P. Berge et al., Rev. Sci. Inst., **32** (1961) 538

[49] M. Dejardin, CPLEAR note CP/SW/043 (1993)

[50] I. Mandic and M.Mikuz, CPLEAR note CP/SW/038 (1992)

[51] E. Ginsgerg, Phys. Rev. **171** (1968) 1675, Errata in Phys. Rev. **174** (1968) 2169

[52] R. Adler et al., CPLEAR Collaboration, Phys. Lett. **B374** (1996) 313

[53] A. Angelopoulos et al., CPLEAR Collaboration, Phys. Lett. **B413** (1997) 422

Publications and Proceedings

1 Publications

- R. Adler et al., CPLEAR Collaboration,
  Measurement of the K_L-K_S mass difference using semileptonic decays of tagged neutral kaons
  Phys. Lett. **B363** (1995) 237

- R. Adler et al., CPLEAR Collaboration,
  Measurement of the CP violation parameter η_{+-} using tagged K^0 *and* $\overline{\mathrm{K}}^0$
  Phys. Lett. **B363** (1995) 243

- R. Adler et al., CPLEAR Collaboration, and J. Ellis et al.,
  Tests of CPT symmetry and quantum mechanics with experimental data from CPLEAR
  Phys. Lett. **B364** (1995) 239

- R. Adler et al., CPLEAR Collaboration,
  First observation of a particle-antiparticle asymmetry in the decay of neutral kaons into $\pi^0\pi^0$
  Z. Phys. **C70** (1996) 211

- R. Adler et al., CPLEAR Collaboration,
  The CPLEAR detector at CERN
  Nucl. Instr. and Meth. in Phys. Res. **A379** (1996) 76

- R. Adler et al., CPLEAR Collaboration,
  Evaluation of the phase of the CP violation parameter η_{+-} and the K_L-K_S mass difference from a correlation analysis of different experiments
  Phys. Lett. **B369** (1996) 367

- R. Adler et al., CPLEAR Collaboration,
  Search for CP violation in the decay of neutral kaons to $\pi^+\pi^-\pi^0$
  Phys. Lett. **B370** (1996) 167

- R. Adler et al., CPLEAR Collaboration,
  Observation of the CP-conserving $K_S \to \pi^+\pi^-\pi^0$ decay amplitude
  Phys. Lett. **B374** (1996) 313

- R. Adler et al., CPLEAR Collaboration,
  Experimental measurement of the K_SK_S/K_SK_L ratio in antiproton annihilations at rest in gaseous hydrogen at 15 and 27 bar
  Phys. Lett. **B403** (1997) 383

- R. Adler et al., CPLEAR Collaboration,
  CPLEAR results on the CP parameters of neutral kaons decaying to $\pi^+\pi^-\pi^0$
  Phys. Lett. **B407** (1997) 193
- A. Angelopoulos et al., CPLEAR Collaboration,
  An upper limit for the branching ratio of the decay $K_S \to e^+e^-$
  Phys. Lett. **B413** (1997) 232
- A. Angelopoulos et al., CPLEAR Collaboration,
  Measurement of the neutral kaon regeneration amplitude in carbon at momenta below 1 GeV/c,
  Phys. Lett. **B413** (1997) 422
- A. Angelopoulos et al., CPLEAR Collaboration, and M.P. Locher, V.E. Markushin,
  Direct Determination of Two-Pion Correlations for $\overline{p}p \to 2\pi^+2\pi^-$ *Annihilation at Rest*
  Eur. Phys. J. **C1** (1998) 139
- A. Apostolakis et al., CPLEAR collaboration,
  An EPR experiment testing the non-separability of the $K^0\overline{K}^0$ *wave function*
  submitted to Phys. Lett. B, CERN-PPE/97-140
- A. Angelopoulos et al., CPLEAR Collaboration,
  Measurement of the CP-violation parameter η_{00} *using tagged* $\overline{K}^0$ *and* K^0
  submitted to Phys. Lett. B, CERN-PPE/97-148

Proceedings

Among $\approx$ 45 referenced proceedings of conferences between 1994 and 1998, the author gave a direct contribution to three of them:

- *CPLEAR Study of* K^0 *and* $\overline{K}^0$ *Semileptonic Decays: Experimental Topics*
  The CPLEAR Collaboration, poster presented by F. Blanc
  at the 2nd International Symposium on Symmetries in Subatomic Physics
  Seattle, USA, June 25-28, 1997
  No proceedings
- *Measurement of the* K^0_{e3} *Form Factor at CPLEAR*
  The CPLEAR Collaboration, talk presented by F. Blanc
  at the Swiss Physical Society
  La Chaux-de-Fonds, Switzerland, October 10, 1997
  Bulletin SPG/SSP, Vol. 14, No 1, 1997
- *Recent Results at CPLEAR*
  The CPLEAR Collaboration, talk presented by F. Blanc
  at the Swiss Physical Society
  Bern, Switzerland, February 26-27, 1998
  Bulletin SPG/SSP, Vol. 15, No 1, 1998

Other selected proceedings:

- *Direct Measurement of T-Violation in the Neutral Kaon System Using Tagged* K^0,$\overline{K}^0$ *at LEAR*
  The CPLEAR Collaboration, talk presented by P. Weber
  at the IV International Symposium on Weak and Electromagnetic Interactions in Nuclei (WEIN'95)
  Osaka, Japan, 1995
  Editors H. Ejiri, T. Kishimoto, T. Sato, World Scientific (1995), p. 52-57

- *Studies of CP, T and CPT Symmetries from the CPLEAR Experiment*
  The CPLEAR Collaboration, presented by R. Gamet
  at the XIVth International Conference on Particles and Nuclei (PANIC'96)
  Williamsburg, USA, May 22-28, 1996
  Editors C. Carlson, J. Domingo, World Scientific (1997), p. 460-463

- *Results on CP and CPT Violation*
  The CPLEAR Collaboration, presented by P. Bloch
  at Physics in Collision (PIC'97)
  Bristol, England, June 25-27, 1997

- *CPLEAR Experiment at CERN: CP, T and CPT Measurements in the Neutral Kaon System*
  The CPLEAR Collaboration, presented by D. Zavrtanik
  at the International Europhysics Conference on High Energy Physics (HEP'97)
  Jerusalem, Israel, August 19-26, 1997

- *Upper Limit for the Branching Ratio of $K_S \to e^+e^-$ Decay*
  The CPLEAR Collaboration, presented by I. Mandic
  at the 7th International Conference on Hadron Spectroscopy (Hadron'97)
  Brookhaven National Laboratory, USA, August 25-30, 1997

Acknowledgements

Many persons contributed directly or indirectly to the result of this thesis. May they all be thanked!

First of all, I would like to thank Professor Lukas Schaller and PD Dr. Tatsuya Nakada for having given me the opportunity of starting this thesis nearly five years ago. They always encouraged me and they proved their confidence in my work.

My special thanks go to Peter-Raymond Kettle, who spent so much time explaining to me the various aspects of experimental physics. I admire his patience and his love for a rigorous work. I would also like to thank him for the thorough reading of my thesis, and his helpful comments.

I am very thankful to Peter Weber for his precious help and advices on the data analysis, as well as for the constructive remarks about my thesis.

I would also like to express my thanks to all members of the CPLEAR collaboration. I want particularly to thank:
Panagiotis Pavlopoulos and Maria Fidecaro,
Philippe Bloch and Marc Dejardin, who introduced me to lots of details on the experiment and semileptonic data analysis,
Othmar Wigger, Robert Kreuger, Pedram Bargassa, Angela Benelli-Maley and Thomas Schietinger for all our interesting discussions about physics, computing, statistics, culture, politics, ... , and above all for their friendship.

Many thanks to the Fribourg ME group for their help and support during these $4\frac{1}{2}$ years.

I also thank the CPLEAR and Fribourg secretaries for their constant help in all kind of administrative problems.

Finally, my most grateful thanks go to my parents, who always encouraged me along my studies, and to Nat, who supported me with love every day for the five past years.

Curriculum Vitae

Name:	Blanc Frédéric
Date of birth:	31st of March 1969
Place of birth:	Montreux, Switzerland
Nationality:	Swiss
Address:	Av. de la Prairie 2b CH-1814 La Tour-de-Peilz

Studies:

1984: "Certificat d'Etudes Secondaires", at Corsier/Vevey, Switzerland.

1987: "Maturité Fédérale scientifique',
at the CESSEV, Burier, Switzerland.

1987-1992: Undergraduate studies at the Swiss Institute for Technology,
Lausanne, Switzerland

1993: "Diplôme d'Ingénieur Physicien EPF",
Diploma thesis:"Etude du Flux *UV* at du Flux *IR* d'étoiles λ Bootis."

1993-1998: Assistant at the University of Fribourg, with different teaching duties, and at the Paul Scherrer Institute (PSI).
PhD thesis within the CPLEAR Collaboration at CERN.
Title of the thesis: "Measurement of the K^0_{e3} Form Factor at the CPLEAR Experiment"

Languages:

French:	mother language
English:	spoken and written
German:	basic knowledge